A theoretical framework for waveguide quantum electrodynamics and its application in disordered systems

Dissertation
zur Erlangung des akademischen Grades

doctor rerum naturalium

(Dr. rer. nat.)

im Fach Physik

Spezialisierung: Theoretische Physik

eingereicht an der

Mathematisch-Naturwissenschaftlichen Fakultät

der Humboldt-Universität zu Berlin

von

Diplom-Physiker Michael Peter Schneider

Präsident der Humboldt-Universität zu Berlin

Prof. Dr. Jan-Hendrik Olbertz

Dekan der Mathematisch-Naturwissenschaftlichen Fakultät

Prof. Dr. Elmar Kulke

Gutachter/innen:

1. Prof. Dr. Kurt Busch
2. Prof. Dr. Alejandro Saenz
3. Prof. Dr. Alexander Shnirman

Tag der mündlichen Prüfung: 15.12.2015

Ich erkläre, dass ich die Dissertation selbständig und nur unter Verwendung der von mir gemäß § 7 Abs. 3 der Promotionsordnung der Mathematisch-Naturwissenschaftlichen Fakultät, veröffentlicht im Amtlichen Mitteilungsblatt der Humboldt-Universität zu Berlin Nr. 126/2014 am 18.11.2014 angegebenen Hilfsmittel angefertigt habe.

Berlin, den 1. Oktober 2015

To my parents

Introduction

The development of quantum mechanics began over 100 years ago with the seminal paper of Max Planck [1] and has proven extremely successful in describing the world at atomic scales but also led to huge controversies, especially in its the early times. One of its most intriguing properties is the phenomenon of entanglement, where two (or more) particles, described by the same wave-function, are instantaneously correlated even at very large distances [2]. The emergence of a non-local quantum theory was unexpected, since it could possibly induce superluminal information transfer. This led to a lot of confusion and even Einstein had the impression that entanglement provides a "spooky action at a distance" [3]. However, entanglement and non-locality have eventually been confirmed experimentally by measuring Bell's inequalities [4, 5].

In the last decades quantum mechanical effects, especially entanglement, have turned from fascinating phenomena to actual tools which can be used to improve existing technologies or even create new ones. The applications range from secure communication between two parties (*quantum key distribution* [6, 7]) over the large-distance transfer of a given quantum state (*quantum teleportation* [8, 9]) to ultra-high measurement sensitivity (*quantum metrology* [10]). Moreover, one can also imagine to construct a quantum network, which consists of quantum nodes that are connected via quantum channels [11] (see Fig. 1). The idea behind a quantum network is that entanglement is generated, processed and stored at the nodes and subsequently distributed over the whole network through the quantum channels. Compared to classical networks, quantum networks have an exponentially larger state space, they can be used to dis-

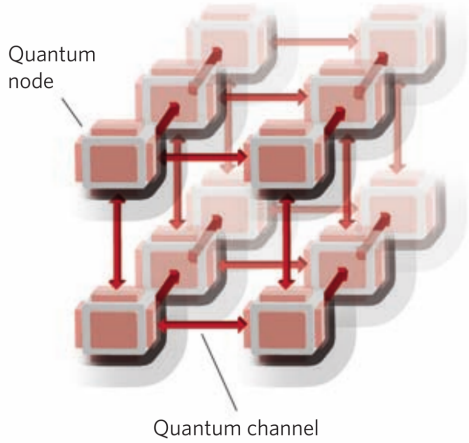

Figure 1: *Sketch of a quantum network consisting of quantum nodes which are connected via quantum channels (Figure adapted from Ref. [11]).*

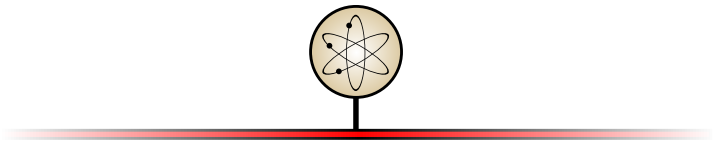

Figure 2: *Sketch of a prototypical waveguide QED setup, comprising a quantum emitter coupled to a one-dimensional waveguide.*

tribute quantum software [12] and quantum keys and are also essential for quantum computing, which plays a major role e.g. in cryptography [13].

A key ingredient of quantum networks are nodes with a long storage time and channels which distribute the entanglement with a high fidelity. Photons offer themselves for this task, since they provide a long coherence time and interact only weakly with the environment, whereas the quantum nodes can be realized for example by means of single quantum emitters (like cold atoms or quantum dots) or atomic ensembles [11]. In its simplest implementation, a single building block for a quantum network thus consists of a quantum emitter coupled to a one-dimensional waveguide as shown in Fig. 2. The physical description is summarized under the term *waveguide quantum electrodynamics* (waveguide QED).

Waveguide QED has experienced growing interest in the past decade from the experimental as well as the theoretical side and it will also be the topic of this thesis. For this purpose the quantum emitter is modeled as a two-level system (TLS) and the waveguide is characterized by its dispersion relation. Within this thesis a new theoretical formalism of waveguide QED is presented, that is based on quantum-field theory and is capable to provide Green's functions for different excitation numbers and arbitrary dispersion relations. In analogy to electrons in crystalline solids, these dispersion relations can also exhibit band edges, which leads to the formation of a bound atom-photon state. This framework is used to examine the effects of band edges on the scattering matrix, to study the dynamics of few-photon wavepackets and to analyze the influence of disorder in the waveguide on the decay properties of the TLS.

Outline

What follows is a detailed outline of the topics considered in this thesis.

In Chapter 1 we present the fundamental concepts of quantum-field theoretical Green's functions. We focus on the properties and techniques which are relevant throughout the thesis, i.e. the self-consistent treatment of interaction and the representation of Green's functions in terms of Feynman diagrams.

Chapter 2 deals with the derivation of the underlying physical model of waveguide QED. Starting with the quantization of the electromagnetic field we continue with the discussion of light-matter interaction on an atomic length scale. After presenting several experimental realizations of waveguide QED these results are used to construct the Hamiltonian which is used throughout this thesis.

Chapter 3 contains the main part of this thesis, the theoretical framework of waveguide QED

based on Green's functions. We derive the Green's function in the system in the one- and two-excitation sector. We find a self-consistent description in the latter case, and use them to calculate the corresponding scattering matrices and spectral densities. To benchmark our approach, in this Chapter the focus will be on the derivation of known results, i.e. the scattering matrix in the one-excitation sector for arbitrary dispersion relations and in the two-excitation sector for a linear one (i.e. no band edges). We find that in this case the two-photon Green's function has an especially easy form since the perturbation series breaks down after the second order.

The examination of the Green's function in the two-excitation sector with a nonlinear dispersion relation is deferred to Chapter 4. In the first part of this chapter we employ perturbative methods to calculate analytic corrections to the scattering matrix by a nonlinear dispersion relation and afterwards we discuss the effect of a band edge with the help of numerical methods. We find here that the first nonvanishing term in the perturbation series encapsulates the effect of interaction-induced radiation trapping (IIRT), i.e. the efficient excitation of a polaritonic eigenstate of the system which lies in the band gap and is thus not existent for a linear dispersion relation.

In Chapter 5 we employ the Green's functions to calculate the dynamics of one- and two-photon pulses in a waveguide with a linear dispersion relation. In this fully analytic calculation we find that the scattering behavior as well as the maximal excitation of the TLS are correlated and can be explained by the ratio of the different length scales involved. Moreover, we compare the results with numeric calculations on a tight-binding chain, which includes also effects of a nonlinear dispersion relation.

Chapter 6 is devoted to the influence of fabricational disorder in the waveguide on the decay properties of the TLS. Already in a rough approximation, which is again supported by numeric calculations, we find that the aforementioned polaritonic eigenstate is stable against sufficiently small disorder but breaks down at a critical disorder strength due to a smearing of the density of states. In addition, we identify a new class of diagrams which are dominant far away from the band edge and act as a memory kernel, thus rendering the system non-Markovian.

Finally, we conclude our results in Chapter 7 and give a short outlook on the possible extensions of the presented work.

Acknowledgments

This thesis in its current form would not have been possible without the help of a number of people.

First of all, I would like to thank Prof. Kurt Busch, who accepted me as a PhD student in his group. He gave me the opportunity to pursue my own ideas and I greatly profited from his expertise. Without him, this thesis would not have been possible.

Furthermore, I am very grateful to Prof. Alexander Shnirman and Prof. Alejandro Saenz, who agreed to review my thesis, and Prof. Oliver Benson and Prof. Mikhail Ivanov, who complete the doctoral degree committee.

I would like to express my gratitude to the members of the group Theoretical Optics & Photonics, with whom I experienced great companionship. I am especially thankful to my roommates and to my colleagues who agreed to proof-read my thesis.

Last but not least, many thanks to my friends, my family and Emeline for all the support, encouragement and understanding.

Contents

List of Figures

1 GREEN'S FUNCTIONS

In this chapter we introduce the concept of Green's functions, which are our main tools throughout the thesis. Green's functions are used in many areas of physics and nowadays a variety of textbooks are available covering the topic from different points of view [14–17]. We follow the line of reasoning presented by Mahan [16] in this chapter. The topics include a reminder about the interaction representation and the S-Matrix, an introduction to Green's functions and how they behave in the presence of interactions.

1.1 Time evolution in quantum mechanics

We start our journey to Green's functions with standard quantum mechanics and the different ways how to implement time. Note that throughout this thesis we set $\hbar = 1$, furthermore we assume all Hamiltonians and operators do not explicitly depend on time.

Quantum mechanics is usually taught in the *Schrödinger representation*, which is based on the Schrödinger equation

$$i\frac{\partial}{\partial t}|\Psi_S(t)\rangle = H|\Psi_S(t)\rangle. \tag{1.1}$$

In the Schrödinger representation the operators are taken to be independent of time but the states evolve in time according to the formula

$$|\Psi_S(t)\rangle = e^{-iHt}|\Psi_S(0)\rangle. \tag{1.2}$$

Quantum mechanics can be equivalently expressed in the *Heisenberg representation*. Here, the operators evolve in time according to the formula

$$i\frac{\partial}{\partial t}O_H(t) = [O_H(t), H] \tag{1.3}$$

and the states are independent of time. The connection between the two representations is given by

$$O_H(t) = e^{iHt}O_S e^{-iHt}, \tag{1.4}$$

where $O_S = O_H(0)$ corresponds to the operator in the Schrödinger representation. Note that both representations lead to the same expectation values $\langle \Psi_S^\dagger(t)|O_S|\Psi_S(t)\rangle = \langle \Psi_H^\dagger|O_H(t)|\Psi_H\rangle$.

In physics we often encounter Hamiltonians of the form

$$H = H_0 + V, \tag{1.5}$$

where H_0 is the Hamiltonian of the unperturbed system, which is assumed to be exactly solvable, and V describes the interaction. It is often the case that the interactions are difficult to handle and render the total Hamiltonian H impossible to diagonalize. If the Hamiltonian is of the form above it is useful to switch to the *interaction representation*, where the operators and states are transformed as

$$O_I(t) = e^{iH_0t} O_I(0) e^{-iH_0t} \tag{1.6}$$

$$|\Psi_I(t)\rangle = e^{iH_0t} e^{-iHt} |\Psi_I(0)\rangle. \tag{1.7}$$

In this case, the connection to the Schrödinger representation is given by $O_I(0) = O_S$ and $|\Psi_I(0)\rangle = |\Psi_S(0)\rangle$. The time dependence of the states can also be written in terms of the time evolution operator

$$|\Psi_I(t)\rangle = U_I(t)|\Psi_I(0)\rangle, \qquad \text{with} \quad U_I(t) = e^{iH_0t}e^{-iHt}. \tag{1.8}$$

We can obtain the equation of motion for the time evolution operator by taking the derivative with respect to t

$$\begin{aligned} \frac{\partial}{\partial t} U_I(t) &= i e^{iH_0t}(H_0 - H) e^{-iHt} \\ &= -i e^{iH_0t} V \left(e^{-iH_0t} e^{iH_0t} \right) e^{-iHt} \\ &= -i V_I(t) U_I(t), \end{aligned} \tag{1.9}$$

where we can see that the dynamics of $U_I(t)$ is governed by the interaction Hamiltonian. At this point we can clearly see the idea behind the interaction representation: the trivial part of the time-evolution (governed by H_0) is absorbed into the operators, which leaves only the nontrivial interaction as a determining factor of the time-evolution operator of the states. Integrating the above equation yields

$$U_I(t) = 1 - i \int_0^t \mathrm{d}t_1 V_I(t_1) U_I(t_1), \tag{1.10}$$

where we have used $U_I(0) = 1$. This equation can be formally solved by iterating it, i.e. by replacing $U_I(t_1)$ in the integral with its definition Eq. (1.10) over and over again. This procedure yields

$$\begin{aligned} U_I(t) &= 1 - i \int_0^t \mathrm{d}t_1 V_I(t_1) + (-i)^2 \int_0^t \mathrm{d}t_1 \int_0^{t_1} \mathrm{d}t_2 V_I(t_1) V_I(t_2) + \dots \\ &= \sum_{n=0}^{\infty} (-i)^n \int_0^t \mathrm{d}t_1 \int_0^{t_1} \mathrm{d}t_2 \dots \int_0^{t_{n-1}} \mathrm{d}t_n V_I(t_1) V_I(t_2) \dots V_I(t_n). \end{aligned} \tag{1.11}$$

Note that the integrals appearing in the sum are strongly coupled: the first integral is over the integration limits of the second integral, the second integral over the integration limits of the third integral and so on. This coupling can be greatly simplified by introducing the time ordering operator T. The time ordering operator acts on a group of time-dependent operators and orders them in such a way that the earliest times are to the right, i.e.

$$T[V_I(t_1)V_I(t_2)] = \Theta(t_1 - t_2)V_I(t_1)V_I(t_2) + \Theta(t_2 - t_1)V_I(t_2)V_I(t_1). \tag{1.12}$$

Here, $\Theta(x)$ is the Heaviside step function with $\Theta(0) = \frac{1}{2}$. With the help of the time ordering operator and a combinatorical prefactor we can write

$$\begin{aligned}\frac{1}{2!}\int_0^t \mathrm{d}t_1 \int_0^t \mathrm{d}t_2 T[V_I(t_1)V_I(t_2)] \\ &= \frac{1}{2!}\int_0^t \mathrm{d}t_1 \int_0^{t_1} \mathrm{d}t_2 V_I(t_1)V_I(t_2) + \frac{1}{2!}\int_0^t \mathrm{d}t_2 \int_0^{t_2} \mathrm{d}t_1 V_I(t_2)V_I(t_1) \\ &= \int_0^t \mathrm{d}t_1 \int_0^{t_1} \mathrm{d}t_2 V_I(t_1)V_I(t_2),\end{aligned} \tag{1.13}$$

which is exactly the term appearing in Eq. (1.11). This decomposition holds for any number n of time-dependent operators (with the corresponding combinatorical prefactor $1/n!$). Inserting the above equation in Eq. (1.11) we find

$$\begin{aligned}U_I(t) &= 1 + \sum_{n=1}^{\infty} \frac{(-i)^n}{n!} \int_0^t \mathrm{d}t_1 \int_0^t \mathrm{d}t_2 \ldots \int_0^t \mathrm{d}t_n T[V_I(t_1)V_I(t_2)\ldots V_I(t_n)] \\ &= T\exp\left[-i\int_0^t \mathrm{d}t_1 V_I(t_1)\right],\end{aligned} \tag{1.14}$$

which is our desired solution for the time evolution operator. Note that we have also found a nontrivial link between Eq. (1.8) and (1.14), i.e. that a product of two exponentiated operators can be written as the time-ordered exponential of a different operator.

The time evolution operator considered so far gives the connection between states at time 0 and t. We turn now to the general time evolution of states (i.e. from time t' to t), which is given by the S-Matrix $\mathcal{S}(t, t')$,

$$|\Psi_I(t)\rangle = \mathcal{S}(t, t')|\Psi_I(t')\rangle. \tag{1.15}$$

With our original definition of the time evolution operator we find

$$|\Psi_I(t)\rangle = U_I(t)|\Psi_I(0)\rangle = \mathcal{S}(t, t')U_I(t')|\Psi_I(0)\rangle \quad \Rightarrow \quad \mathcal{S}(t, t') = U_I(t)U_I^\dagger(t'). \tag{1.16}$$

From this definition, we can readily infer

$$\mathcal{S}(t, t) = 1, \quad \mathcal{S}^\dagger(t, t') = \mathcal{S}^{-1}(t, t') = \mathcal{S}(t', t), \quad \mathcal{S}(t, t')\mathcal{S}(t', t'') = \mathcal{S}(t, t'') \tag{1.17}$$

and the equation of motion is defined in analogy to $U_I(t)$,

$$\frac{\partial}{\partial t}\mathcal{S}(t, t') = -iV_I(t)\mathcal{S}(t, t') \quad \Rightarrow \quad \mathcal{S}(t, t') = T\exp\left[-i\int_{t'}^t \mathrm{d}t_1 V_I(t_1)\right]. \tag{1.18}$$

1.2 The Green's function

We turn now to the actual calculation of Green's functions. The time-ordered Green's function is defined as

$$G^T(\lambda, t-t') = -i\langle\Psi|TC_{\lambda,H}(t)C^\dagger_{\lambda,H}(t')|\Psi\rangle, \tag{1.19}$$

where λ encapsulates the quantum numbers of the system and $C^\dagger_{\lambda,H}(t)$ ($C_{\lambda,H}(t)$) is a second-quantized creation (annihilation) operator in the Heisenberg representation. In the limit of zero temperature, $|\Psi\rangle$ represents the ground state of the system. We use only this case here, the case for finite temperature can be found in the literature [14, 16, 17].

Before we begin with the calculation of the Green's function, we would like to get an idea with what kind of object we are dealing here. In the case of $t > t'$ the operators in the Green's function create a particle at time t and destroy it at t'. In other words, the Green's function propagates a particle from time t to t'. For this reason, Green's functions are sometimes also called *propagators*.

In order to calculate the Green's function we have to know the ground state $|\Psi\rangle$ of the interacting system. This is not a trivial task, in fact it is in most cases not possible to calculate the ground state exactly. However, if the Hamiltonian is of the form

$$H = H_0 + V \tag{1.20}$$

we can assume that the ground state $|\phi_0\rangle$ of H_0 is known. We furthermore assume that the interaction term V is switched off in the asymptotic limit $t \to -\infty$ and the system is thus in the ground state $|\phi_0\rangle$. According to the theorem of Gell-Mann and Low [18], the system stays in the ground state when the interaction is turned on adiabatically[1]. Hence, we find for the ground state of the full Hamiltonian in the interaction representation

$$|\Psi_I(t)\rangle = \mathcal{S}(t, -\infty)|\phi_0\rangle. \tag{1.21}$$

Assuming furthermore that the interaction is switched off adiabatically for $t \to \infty$ we expect that we find again the same state $|\phi_0\rangle$. The interactions could only lead to an additional phase, hence we find

$$\mathcal{S}(\infty, t)|\Psi_I(t)\rangle = |\phi_0\rangle e^{i\Theta}. \tag{1.22}$$

Thus, we can write

$$e^{i\Theta} = \langle\phi_0|\mathcal{S}(\infty, -\infty)|\phi_0\rangle \tag{1.23}$$

and

$$\langle\Psi_I(t)| = \langle\phi_0|\mathcal{S}(-\infty, t) = e^{-i\Theta}\langle\phi_0|\mathcal{S}(\infty, -\infty)\mathcal{S}(-\infty, t) = \frac{\langle\phi_0|\mathcal{S}(\infty, t)}{\langle\phi_0|\mathcal{S}(\infty, -\infty)|\phi_0\rangle}. \tag{1.24}$$

Since the ground state is given in the interaction representation, the operators have to be transformed correspondingly,

$$C_{\lambda,H}(t) = e^{iHt}e^{-iH_0t}C_{\lambda,I}(t)e^{iH_0t}e^{-iHt} = U^\dagger_I(t)C_{\lambda,I}(t)U_I(t) = \mathcal{S}(0, t)C_{\lambda,I}(t)\mathcal{S}(t, 0). \tag{1.25}$$

[1] This behavior can be understood as follows: The interaction is turned on so slowly that the energy change in the system is much smaller than the distance to the first excited level. Hence, the system stays in the ground state at all times.

Combining Eq. (1.25), (1.21) and (1.24) with (1.19) and shortening the notation with $\langle\phi_0|\ldots|\phi_0\rangle = \langle\ldots\rangle$ we find[2]

$$G^T(\lambda, t-t') = \frac{-i\langle T\mathcal{S}(\infty,t)C_\lambda(t)\mathcal{S}(t,t')C_\lambda^\dagger(t')\mathcal{S}(t',-\infty)\rangle}{\langle\mathcal{S}(\infty,-\infty)\rangle}. \tag{1.26}$$

Note that we have suppressed here the subscript for the interaction representation. In the remainder of this chapter we will always suppress this subscript and all time-dependent operators are in the interaction representation. Since the time-ordering operator in the numerator allows us to interchange the order of the operators we can write all S-Matrices to the right and find

$$G^T(\lambda, t-t') = \frac{-i\langle TC_\lambda(t)C_\lambda^\dagger(t')\mathcal{S}(\infty,-\infty)\rangle}{\langle\mathcal{S}(\infty,-\infty)\rangle}, \tag{1.27}$$

which is our desired result.

In the case of a clean system $V = 0$ the S-Matrix is unity (cf. Eq. (1.18)) and the free Green's function is given by

$$\begin{aligned} G_0^T(\lambda, t-t') &= -i\langle TC_\lambda(t)C_\lambda^\dagger(t')\rangle \\ &= -i\Theta(t-t')\langle C_\lambda(t)C_\lambda^\dagger(t')\rangle - i\Theta(t'-t)\langle C_\lambda^\dagger(t')C_\lambda(t)\rangle \\ &= G_0^R(\lambda, t-t') + G_0^A(\lambda, t-t'). \end{aligned} \tag{1.28}$$

In the last line we have defined the *retarded Green's function* $G_0^R(\lambda, t-t')$, which propagates the particle to a later time and the *advanced Green's function* $G_0^A(\lambda, t-t')$, which propagates to an earlier time. When we furthermore assume that the ground state is given by the particle vacuum $|\phi_0\rangle = |0\rangle$ we find

$$\begin{aligned} G_0^T(\lambda, t-t') &= -i\Theta(t-t')\langle C_\lambda(t)C_\lambda^\dagger(t')\rangle \\ &= -i\Theta(t-t')e^{-i\epsilon_\lambda(t-t')}\langle C_\lambda C_\lambda^\dagger\rangle \\ &= -i\Theta(t-t')e^{-i\epsilon_\lambda(t-t')} \\ &= G_0^R(\lambda, t-t'), \end{aligned} \tag{1.29}$$

where we have used the fact that $C_\lambda|0\rangle = 0$ and ϵ_λ is the energy Eigenvalue of the corresponding quantum number λ. Remarkably, the time-ordered Green's function collapses to the retarded one in this case and propagates the particles only to later times. Since we only consider vacuum ground states in this thesis we drop the superscript from now on and treat the Green's functions as time-ordered or retarded, whichever one is appropriate. In frequency domain, the Green's function is given by

$$G_0(\lambda, \omega) = \int_{-\infty}^{\infty} \mathrm{d}t G_0(\lambda, t) e^{i(\omega+i\delta)t} = \frac{1}{\omega - \epsilon_\lambda + i\delta} \tag{1.30}$$

We will encounter the Green's function in frequency domain often in the remainder of this thesis. Note that we have added an infinitesimal quantity $i\delta$ to the frequency in order to get a convergent integral and to ensure the correct propagation direction in time.

[2]Note that we have used here $|\Psi\rangle = |\Psi_I(t=0)\rangle$ to connect the states and the operators seamlessly.

1.3 Green's functions and interaction

In order to study the effects of interaction, we consider a toy model featuring two species of bosons which can be transformed into each other,

$$H_0 = \int \frac{\mathrm{d}k}{2\pi} \left(\omega_a(k) a_k^\dagger a_k + \omega_b(k) b_k^\dagger b_k \right), \qquad V = U \int \frac{\mathrm{d}k}{2\pi} \frac{\mathrm{d}k'}{2\pi} \left(a_k^\dagger b_{k'} + \text{h.c.} \right). \tag{1.31}$$

Here, $\omega_a(k)$ and $\omega_b(k)$ are the energies of the respective species, U is the interaction coupling constant and k can be interpreted as the momentum of the bosons which can be changed by the interaction. The free Green's functions are given by

$$G_{0,a}(k, t-t') = -i\langle T a_k(t) a_k^\dagger(t') \rangle, \qquad G_{0,b}(k, t-t') = -i\langle T b_k(t) b_k^\dagger(t') \rangle \tag{1.32}$$

and the full Green's function[3] can be constructed by expanding the S-Matrix in the numerator of Eq. (1.27) in a Taylor series,

$$G_a(k, t-t') = \sum_{n=0}^{\infty} \frac{(-i)^{n+1}}{n!} \int_{-\infty}^{\infty} \mathrm{d}t_1 \ldots \int_{-\infty}^{\infty} \mathrm{d}t_n \frac{\langle T a_k(t) V(t_1) \ldots V(t_n) a_k^\dagger(t') \rangle}{\langle \mathcal{S}(\infty, -\infty) \rangle} \tag{1.33}$$

In the numerator of this equation we encounter terms of the form

$$\langle T a_k(t) V(t_1) V(t_2) a_k^\dagger(t') \rangle. \tag{1.34}$$

Inserting the Hamiltonian from our toy model, we find that the main difficulty lies in the evaluation of time-ordered brackets like

$$\langle T a_k(t) a_p(t_1) b_{p'}^\dagger(t_1) a_q^\dagger(t_2) b_{q'}(t_2) a_k^\dagger(t') \rangle. \tag{1.35}$$

Expressions like this can be greatly simplified with the help of *Wick's Theorem* [19]. Wick's Theorem states that the time-ordered average (with respect to the ground state) of a product of non-interacting creation and annihilation operators can be written as the sum over all possible pairings of operators. A pairing is the product of two time-ordered operators whose product is nonvanishing (i.e. $\langle T a_k(t) a_k^\dagger(t') \rangle$). The pairing can be visualized by brackets connecting the two operators, in our case we find

$$\begin{aligned}
&\langle T \underbrace{a_k(t) a_p(t_1) \overbrace{b_{p'}^\dagger(t_1) a_q^\dagger(t_2)}^{} b_{q'}(t_2) a_k^\dagger(t')}_{} \rangle + \langle T \underbrace{a_k(t) \underbrace{a_p(t_1) \overbrace{b_{p'}^\dagger(t_1) a_q^\dagger(t_2)}^{} b_{q'}(t_2)}_{} a_k^\dagger(t')}_{} \rangle \\
&\quad = \langle T b_{q'}(t_2) b_{p'}^\dagger(t_1) \rangle \langle T a_p(t_1) a_k^\dagger(t') \rangle \langle T a_k(t) a_q^\dagger(t_2) \rangle \\
&\qquad + \langle T b_{q'}(t_2) b_{p'}^\dagger(t_1) \rangle \langle T a_p(t_1) a_q^\dagger(t_2) \rangle \langle T a_k(t) a_k^\dagger(t') \rangle \\
&\quad = -i G_{0,b}(p', t_2 - t_1) G_{0,a}(k, t_1 - t') G_{0,a}(k, t - t_2) \delta_{q'p'} \delta_{pk} \delta_{kq} (2\pi)^3 \\
&\qquad - i G_{0,b}(p', t_2 - t_1) G_{0,a}(p, t_1 - t_2) G_{0,a}(k, t - t') \delta_{q'p'} \delta_{pq} (2\pi)^2,
\end{aligned} \tag{1.36}$$

where we have identified the pairings as the free Green's functions $iG_{0,a/b}$ in the last equation. The free Green's functions are diagonal in momentum and thus generate momentum-conserving

[3] We are only considering $G_a(k, t-t')$ here, the calculation of $G_b(k, t-t')$ follows the same line of reasoning.

δ-functions. Note how this simplifies our calculation: The calculation of the average of a complicated time-ordered product of operators reduces to a sum over products of simple free Green's functions. The downside of this procedure is that it leaves us with a sum which becomes very complicated at higher orders[4]. The structure becomes even more complicated in the presence of fermions, which anticommute and thus lead to sign changes for specific combinations of operators.

With the help of Wick's theorem and Eq. (1.33) we are able to write down the full Green's function for our toy model,

$$\begin{aligned} G_a(k,t-t') = \Big\{ & G_{0,a}(k,t-t') \\ & + U^2 \int \mathrm{d}t_1 \mathrm{d}t_2 \Big[G_{0,a}(k,t-t_2) \int \frac{\mathrm{d}p}{2\pi} G_{0,b}(p,t_2-t_1) G_{0,a}(k,t_1-t') \\ & \qquad + G_{0,a}(k,t-t') \int \frac{\mathrm{d}p}{2\pi} G_{0,b}(p,t_2-t_1) \int \frac{\mathrm{d}p'}{2\pi} G_{0,a}(p',t_1-t_2) \Big] \\ & + \mathcal{O}(U^4) \Big\} / \langle \mathcal{S}(\infty,-\infty) \rangle . \end{aligned} \tag{1.37}$$

In order to get this formula, we have used the following properties: First of all we have noticed that the first order term in the perturbation series vanishes because there is no pairing which gives a finite result. Furthermore we have found that the four initial terms can be reduced to two terms by relabeling the integration variables. Additionally, we have performed the trivial momenta integrations over the δ-functions.

In the next step we depict the terms in the perturbation series graphically with the help of *Feynman diagrams* [15, 20]. In this representation, each free Green's function is depicted by a line (quantum numbers can either be indicated by an additional index or a different style). In our case, we have

$G_{0,a}(k,t-t') =$ 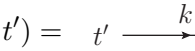 and $G_{0,b}(k,t-t') =$ 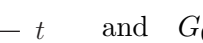 .

(1.38)

The arrows in the Green's function points from the earlier to the later time (above we have assumed $t > t'$). Additionally, we can also depict the interaction in terms of a vertex

$U =$ 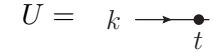 ,

(1.39)

where an a-boson with momentum k is transformed into a b-boson with momentum k'. Rewrit-

[4] In the example we have not shown all terms. Starting from Eq. (1.34) and inserting the full interaction Hamiltonian we are left with eight terms after the Wick contraction.

ing the second-order terms in the numerator of Eq. (1.37) in terms of Feynman diagrams yields

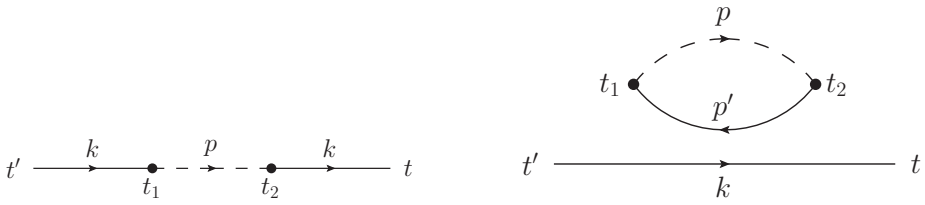

An intriguing property of the Feynman diagram representation is that we can interpret them as actual physical processes. The first term, for example, depicts an a-boson with momentum k which is transformed into a b-boson with momentum p and then again transformed back to an a-boson with momentum k. Note that we have to integrate over all internal degrees of freedom, which would correspond to the momentum p and the times t_1 and t_2 in this case. The diagram on the right represents a different process: Here, the interaction does not couple to the initial a-boson but forms a disconnected "bubble". This diagram together with all other disconnected diagrams form a special class of diagrams which are called vacuum polarization graphs.

At this point we can return to the denominator of Eq. (1.37). Expanding the S-Matrix and depicting the terms as Feynman diagrams yields

$$\begin{aligned}\langle \mathcal{S}(\infty,-\infty)\rangle &= \sum_0^\infty \frac{(-i)^n}{n!}\int \mathrm{d}t_1\ldots\mathrm{d}t_n\langle TV(t_1)\ldots V(t_n)\rangle \\ &= \quad + \ldots,\end{aligned} \tag{1.40}$$

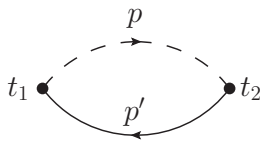

which are exactly the vacuum polarization graphs without the free Green's function. It can be rigorously proven that the terms in the denominator of Eq. (1.37) cancel exactly the disconnected diagrams in the numerator. This is called the *linked cluster theorem* [14, 16]. With the help of this theorem and the fact that every topologically different[5] diagram appears $n!$ times we find that the general full Green's function is a sum over all topologically different, connected diagrams,

$$G_a(k,t-t') = \sum_{n=0}^\infty \underbrace{(-i)^{n+1}\int \mathrm{d}t_1\ldots\mathrm{d}t_n\langle Ta_k(t)V(t_1)\ldots V(t_n)a_k^\dagger(t')\rangle}_{\text{topologically different, connected diagrams}} \tag{1.41}$$

At this point we have reduced the actual perturbation series for the full Green's function to the most fundamental form. Nevertheless the result is not satisfactory because we still have to deal with an infinite sum. Luckily, it is possible in most cases to sum the perturbation series

[5] In this context two diagrams are topologically equivalent if they can be transformed into each other by rearranging the vertices and stretching the Green's functions, but without cutting them. If this is not possible, the two diagrams are topologically different.

in a self-consistent way and to generate a very nice form of the full Green's function (the other case is discussed in the end of this section). To demonstrate this we return to our interacting toy model and transform the perturbation series to the frequency domain

$$G_a(k,\omega) = G_{0,a}(k,\omega) + G_{0,a}(k,\omega)\Sigma_b(\omega)G_{0,a}(k,\omega) + \dots \tag{1.42}$$

Here we have introduced the function

$$\Sigma_b(\omega) = U^2 \int \frac{\mathrm{d}p}{2\pi} G_{0,b}(p,\omega) \tag{1.43}$$

which will become important shortly. When we calculate the higher order terms in the perturbation series we find that we only encounter higher powers of our first order result. Hence we can cast the perturbation series in the form of a Dyson series,

$$\begin{aligned} G_a(k,\omega) &= G_{0,a}(k,\omega) + G_{0,a}(k,\omega)\Sigma_b(\omega)G_{0,a}(k,\omega) + G_{0,a}(k,\omega)[\Sigma_b(\omega)G_{0,a}(k,\omega)]^2 + \dots \\ &= G_{0,a}(k,\omega) + G_{0,a}(k,\omega)\Sigma_b(\omega)\left[G_{0,a}(k,\omega) + G_{0,a}(k,\omega)\Sigma_b(\omega)G_{0,a}(k,\omega) + \dots\right] \\ &= G_{0,a}(k,\omega) + G_{0,a}(k,\omega)\Sigma_b(\omega)G_a(k,\omega). \end{aligned} \tag{1.44}$$

This equation can be solved exactly and we find

$$\begin{aligned} G_a(k,\omega) &= \frac{G_{0,a}(k,\omega)}{1 - G_{0,a}(k,\omega)\Sigma_b(\omega)} = \frac{1}{G_{0,a}^{-1}(k,\omega) - \Sigma_b(\omega)} \\ &= \frac{1}{\omega - \omega_a(k) - \Sigma_b(\omega)} \\ &= \frac{1}{\omega - \Big(\omega_a(k) + \mathrm{Re}\left[\Sigma_b(\omega)\right]\Big) - i\mathrm{Im}\left[\Sigma_b(\omega)\right]}. \end{aligned} \tag{1.45}$$

This is a major result: The full Green's function can be achieved by the formal substitution $\omega \to \omega - \Sigma_b(\omega)$ from the free Green's function. $\Sigma_b(\omega)$ is called *self-energy* in this context and has two effects. The real part can be absorbed in the definition of the unperturbed energy spectrum and is equivalent to an interaction-induced energy shift (e.g. Lamb shift). The imaginary part replaces the infinitesimal $i\delta$ which we introduced into the free Green's function to obtain a convergent integral and the correct propagation direction in time and can be furthermore interpreted as a decay-time $\tau = -\mathrm{Im}[\Sigma_b(\omega)]^{-1}$.

We would like to point out at this point that we have chosen a very simple toy model, where the self-energy can be easily obtained (actually, this model can also be diagonalized exactly). For more complicated systems (e.g. electrons in a metal with electron-electron interaction) the perturbation series can often not be summed exactly. In those cases one usually sums the perturbation series only partially[6], but to an infinite order. This procedure generates a self-energy which may not be exact, but nonetheless leads to an approximate energy shift and decay time. However, the partial summation is only valid for sufficiently small coupling constants and breaks down for strong coupling.

[6] With partially we mean that only few diagrams (which give the dominant contributions) are taken into account for the self-energy. Prominent examples of this procedure are, e.g., the random phase approximation (RPA) in the electron-electron interaction [16] and the self-consistent Born approximation in disordered systems. The latter is presented in Sec. 6.2.

2 LIGHT-MATTER INTERACTION ON THE QUANTUM LEVEL

In this chapter we consider the fundamental physics of light-matter interaction on the quantum level and construct the theoretical model used throughout this thesis. After a short summary about the quantization of the electromagnetic field, we discuss the interaction of the quantized field with a single atom. Eventually, we introduce the concept of waveguide QED together with experimental realizations and construct the corresponding theoretical model.

2.1 Field quantization

In this section we derive the quantization of the electromagnetic field in vacuum, following the book of W.P. Schleich [21]. We begin with the calculation of the (classical) **E**- and **B**-field in vacuum and the Coulomb gauge[1] and use these fields later on to quantize the energy of the electromagnetic field.

2.1.1 The E- and B-field

We start with the microscopic Maxwell's equations,

$$\nabla \cdot \mathbf{B} = 0 \qquad \nabla \times \mathbf{E} = -\frac{\partial \mathbf{B}}{\partial t} \tag{2.1a}$$

$$\nabla \cdot \mathbf{E} = \frac{\rho}{\epsilon_0} \qquad \nabla \times \mathbf{B} = \frac{1}{c^2}\frac{\partial \mathbf{E}}{\partial t} + \mu_0 \mathbf{j}, \tag{2.1b}$$

where ρ and $\mathbf{j}$ denote charge and current density, ϵ_0 is the electric permittivity, μ_0 the magnetic permeability and $c = (\epsilon_0 \mu_0)^{-\frac{1}{2}}$ is the speed of light. The electric and magnetic field can also

[1] For the field quantization in media we refer to the comprehensive derivation by R. Glauber [22] and to the book *Field Quantization* [23] by W. Greiner and J. Reinhardt for quantization procedures in other gauges.

be expressed in terms of a vector potential $\mathbf{A}$ and a scalar potential Φ,

$$\mathbf{E} = -\nabla\Phi - \frac{\partial \mathbf{A}}{\partial t} \qquad \mathbf{B} = \nabla \times \mathbf{A}. \tag{2.2}$$

These potentials are not unique. Potentials of the form

$$\mathbf{A}' = \mathbf{A} + \nabla\Lambda \qquad \Phi' = \Phi - \frac{\partial \Lambda}{\partial t} \tag{2.3}$$

generate the same electric and magnetic fields. This property is called *gauge invariance* and enables us to choose the function Λ such that it simplifies our calculation. Here we choose to work in the Coulomb gauge, which is defined by

$$\nabla \cdot \mathbf{A} = 0. \tag{2.4}$$

Expressing the inhomogeneous Maxwell's equations Eq. (2.1b) in terms of the potentials yields

$$\nabla^2 \mathbf{A} - \frac{1}{c^2}\frac{\partial^2 \mathbf{A}}{\partial t^2} = \nabla\left[\frac{1}{c^2}\frac{\partial \Phi}{\partial t} + \nabla \cdot \mathbf{A}\right] - \mu_0 \mathbf{j} \tag{2.5a}$$

$$-\nabla \cdot \big(\nabla\Phi\big) - \frac{\partial}{\partial t}\big(\nabla \cdot \mathbf{A}\big) = \frac{\rho}{\epsilon_0}. \tag{2.5b}$$

We want to quantize the electromagnetic field in the absence of charges and currents, i.e. $\rho = 0$ and $\mathbf{j} = 0$. In this case and with the help of the Coulomb gauge the second equation reduces to

$$-\nabla \cdot \big(\nabla\Phi\big) = 0, \tag{2.6}$$

which has the solution $\Phi = 0$. Hence, the wave equation for the vector potential is given by

$$\nabla^2 \mathbf{A} - \frac{1}{c^2}\frac{\partial^2 \mathbf{A}}{\partial t^2} = 0. \tag{2.7}$$

The next step is to find a solution to this wave equation. We notice that space and time coordinates decouple and choose an ansatz

$$\mathbf{A}(\mathbf{r}, t) = \Upsilon q(t)\mathbf{v}(\mathbf{r}), \tag{2.8}$$

where Υ is a constant. Inserting this ansatz into the wave equation gives

$$q(t)\nabla^2 \mathbf{v}(\mathbf{r}) - \frac{1}{c^2}\ddot{q}(t)\mathbf{v}(\mathbf{r}) = 0 \tag{2.9}$$

and can be rewritten componentwise as

$$\frac{\nabla^2 v_j(\mathbf{r})}{v_j(\mathbf{r})} = \frac{1}{c^2}\frac{\ddot{q}(t)}{q(t)} \tag{2.10}$$

for each component $j = x, y, z$. Note that all space variables are appearing on the left hand side of this equation and all time variables on the right hand side. This implies that both sides are

independent of $\mathbf{r}$ and t and hence equal to a constant. We choose this constant as $-k^2 = -\mathbf{k}^2$ and find

$$\nabla^2\mathbf{v}(\mathbf{r}) + k^2\mathbf{v}(\mathbf{r}) = 0 \qquad\qquad \ddot{q}(t) + \Omega^2 q(t) = 0, \tag{2.11}$$

where $\Omega = ck$. The value of k^2 depends on the actual problem, i.e. on the boundary conditions of the differential equations above. A common choice for this boundary is a perfect conductor, where the tangential component of $\mathbf{E}$ and the normal component of $\mathbf{B}$ vanish. With the help of Eqs. (2.2) and (2.8), the relations on the boundary ∂V read

$$\mathbf{e}_\parallel(\mathbf{r}) \cdot \mathbf{E}(\mathbf{r},t)\Big|_{\partial V} = -\mathbf{e}_\parallel(\mathbf{r})\frac{\partial \mathbf{A}}{\partial t}\Big|_{\partial V} = -\Upsilon\dot{q}(t)\mathbf{e}_\parallel(\mathbf{r}) \cdot \mathbf{v}(\mathbf{r})\Big|_{\partial V} \stackrel{!}{=} 0 \tag{2.12}$$

which implies

$$\mathbf{e}_\parallel(\mathbf{r}) \cdot \mathbf{v}(\mathbf{r})\Big|_{\partial V} = 0. \tag{2.13}$$

Here, $\mathbf{e}_\parallel(\mathbf{r})$ is a unit vector tangential to the boundary. Introducing a unit vector $\mathbf{e}_\perp(\mathbf{r})$ which is normal to the boundary gives

$$\mathbf{e}_\perp(\mathbf{r}) \cdot \mathbf{B}(\mathbf{r},t)\Big|_{\partial V} = \mathbf{e}_\perp(\mathbf{r}) \cdot \big[\nabla \times \mathbf{A}\big]\Big|_{\partial V} = \Upsilon q(t)\mathbf{e}_\perp(\mathbf{r}) \cdot \big[\nabla \times \mathbf{v}(\mathbf{r})\big]\Big|_{\partial V} \stackrel{!}{=} 0, \tag{2.14}$$

that is

$$\mathbf{e}_\perp(\mathbf{r}) \cdot \big[\nabla \times \mathbf{v}(\mathbf{r})\big]\Big|_{\partial V} = 0. \tag{2.15}$$

Additionally, the Coulomb gauge itself introduces another constraint

$$\nabla \cdot \mathbf{v}(\mathbf{r}) = 0. \tag{2.16}$$

Note that this equation is valid at every point in space, whereas Eqs. (2.13) and (2.15) hold only at the boundary. We are not going to solve the wave equation for a specific setup here, but we note that the boundary conditions lead to a discrete set of solutions of the differential equations Eq. (2.11) which are labeled by an index l. For many setups (especially with a high symmetry) the $l = 0$ solution can be understood as the fundamental resonance of an electromagnetic field in a cavity and the $l > 0$ solutions as higher harmonics. After an appropriate scaling with the so-called mode volume[2] V_l

$$\mathbf{v}_l(\mathbf{r}) = \frac{1}{\sqrt{V_l}}\mathbf{u}_l(\mathbf{r}) \tag{2.17}$$

we find that the solutions form an orthonormal set

$$\frac{1}{\sqrt{V_l V_{l'}}}\int \mathrm{d}^3 r \mathbf{u}_l(\mathbf{r}) \cdot \mathbf{u}_{l'}(\mathbf{r}) = \delta_{l,l'}. \tag{2.18}$$

Hence, we can expand the vector potential in a sum over all modes,

$$\mathbf{A}(\mathbf{r},t) = \sum_l \frac{1}{\sqrt{\epsilon_0 V_l}} q_l(t)\mathbf{u}_l(\mathbf{r}). \tag{2.19}$$

[2] In the present case V_l serves solely as a normalization factor for the solutions of the electromagnetic field $v_l(\mathbf{r})$. However, rewriting Eq. (2.18) as $\int \mathrm{d}^3 r \mathbf{u}_l^2(\mathbf{r}) = V_l$ indicates that the mode volume is also a measure for the field distribution within the boundaries.

This is our desired solution for the vector potential in Coulomb gauge for a given set of boundary conditions. With the help of Eq. (2.2) we can also find the solutions for the electric and magnetic field,

$$\mathbf{E}(\mathbf{r},t) = -\frac{\partial \mathbf{A}}{\partial t} = -\sum_l \frac{1}{\sqrt{\epsilon_0 V_l}} \dot{q}_l(t)\mathbf{u}_l(\mathbf{r}) \tag{2.20a}$$

$$\mathbf{B}(\mathbf{r},t) = \nabla \times \mathbf{A} = \sum_l \frac{1}{\sqrt{\epsilon_0 V_l}} q_l(t) \left[\nabla \times \mathbf{u}_l(\mathbf{r})\right]. \tag{2.20b}$$

It is worth keeping in mind that the lth mode of the $\mathbf{E}$-field $\mathbf{E}_l$ is determined by $\dot{q}_l(t)$ and points in $\mathbf{u}_l(\mathbf{r})$-direction, whereas the lth component of the $\mathbf{B}$-field $\mathbf{B}_l$ is connected with $q_l(t)$ and points in the direction of $\nabla \times \mathbf{u}_l(\mathbf{r})$.

2.1.2 Quantizing the energy of the electromagnetic field

After calculating the electric and magnetic field in the previous section we now turn to the energy of the electromagnetic field, which is given by

$$\mathcal{H} = \int_V \mathrm{d}^3 r \left[\frac{1}{2}\epsilon_0 \mathbf{E}^2(\mathbf{r},t) + \frac{1}{2\mu_0}\mathbf{B}^2(\mathbf{r},t)\right]. \tag{2.21}$$

Inserting the solutions for the $\mathbf{E}$- and $\mathbf{B}$-field (Eq. (2.20a) and (2.20b)) we find

$$\mathcal{H} = \frac{1}{2}\sum_{l,l'} \dot{q}_l \dot{q}_{l'} \frac{1}{\sqrt{V_l V_{l'}}} \int_V \mathrm{d}^3 r \mathbf{u}_l \mathbf{u}_{l'} + \frac{c^2}{2}\sum_{l,l'} q_l q_{l'} \frac{1}{\sqrt{V_l V_{l'}}} \int_V \mathrm{d}^3 r \left(\nabla \times \mathbf{u}_l\right) \cdot \left(\nabla \times \mathbf{u}_{l'}\right). \tag{2.22}$$

The integral in the first term can be evaluated immediately and yields a $\delta_{l,l'}$-function (cf. Eq. (2.18)). The integral in the second term is more complicated and is evaluated separately. The two cross-products can be rewritten as

$$\int_V \mathrm{d}^3 r \left(\nabla \times \mathbf{u}_l\right) \cdot \left(\nabla \times \mathbf{u}_{l'}\right) = \int_V \mathrm{d}^3 r \nabla \cdot \left[\mathbf{u}_{l'} \times \left(\nabla \times \mathbf{u}_l\right)\right] + \int_V \mathrm{d}^3 r \mathbf{u}_{l'} \cdot \left[\nabla \times \left(\nabla \times \mathbf{u}_l\right)\right]. \tag{2.23}$$

By using the theorem of Gauss, the first term can be reformulated as a surface integral

$$\int_V \mathrm{d}^3 r \nabla \cdot \left[\mathbf{u}_{l'} \times \left(\nabla \times \mathbf{u}_l\right)\right] = \int_{\partial V} \mathrm{d}\mathbf{S} \cdot \left[\mathbf{u}_{l'} \times \left(\nabla \times \mathbf{u}_l\right)\right], \tag{2.24}$$

where the surface element $\mathrm{d}\mathbf{S}$ is orthogonal to the surface. In the previous section we have noted that $\mathbf{E}_l \propto \mathbf{u}_l(\mathbf{r})$ and $\mathbf{B}_l \propto \nabla \times \mathbf{u}_l(\mathbf{r})$, which means that the integral is proportional to

$$\int_{\partial V} \mathrm{d}\mathbf{S} \cdot \left[\mathbf{u}_{l'} \times \left(\nabla \times \mathbf{u}_l\right)\right] \propto \int_{\partial V} \mathrm{d}\mathbf{S} \cdot \left[\mathbf{E}_{l'} \times \mathbf{B}_l\right]. \tag{2.25}$$

According to the boundary conditions the $\mathbf{E}$-field is orthogonal to the surface whereas the $\mathbf{B}$-field is tangential. Thus, $\mathbf{E}_{l'} \times \mathbf{B}_l$ is tangential to the surface and the product $\mathrm{d}\mathbf{S} \cdot \left[\mathbf{E}_{l'} \times \mathbf{B}_l\right]$

is zero everywhere on the surface. Hence, the integral vanishes. The double curl in the second term of Eq. (2.23) can be written as

$$\nabla \times \left(\nabla \times \mathbf{u}_l\right) = \nabla \left(\nabla \cdot \mathbf{u}_l\right) - \nabla^2 \mathbf{u}_l = -\nabla^2 \mathbf{u}_l = k_l^2 \mathbf{u}_l = \left(\frac{\Omega_l}{c}\right)^2 \mathbf{u}_l, \tag{2.26}$$

where we have used the Coulomb gauge $\nabla \cdot \mathbf{u}_l = 0$. The integral collapses then to a simple $\delta_{l,l'}$-function and we find for the Hamiltonian of the electromagnetic field

$$\mathcal{H} = \sum_l \mathcal{H}_l = \sum_l \left[\frac{1}{2}\dot{q}_l^2 + \frac{1}{2}\Omega_l^2 q_l^2\right]. \tag{2.27}$$

Each mode of the electromagnetic field behaves as a harmonic oscillator with according frequency Ω_l. Indeed, we find that q_l and $p_l \equiv \dot{q}_l$ are conjugated variables, since they obey Hamilton's equations

$$\dot{q}_l = \frac{\partial \mathcal{H}_l}{\partial p_l} = p_l \qquad\qquad \dot{p}_l = -\frac{\mathcal{H}_l}{q_l} = -\Omega_l^2 q_l, \tag{2.28}$$

which lead to the same equation of motion as before,

$$\ddot{q}_l + \Omega_l^2 q_l = 0. \tag{2.29}$$

Note that the electric field is proportional to p_l and the magnetic field to q_l, which makes it tempting to say that the fields are conjugated variables. This statement does not hold because the electric and magnetic field do not fulfill Hamilton's equations, only q_l and p_l are conjugated variables. Additionally, we point out that the whole calculation was fully classical up to now. We have calculated the energy of the classical electromagnetic field and we have found that each mode is equal to a classical harmonic oscillator.

We now turn to the actual quantization of Eq. (2.27). In order to maintain a better connection to well-known results from quantum mechanics we reintroduce $\hbar$ here and in the next section. Furthermore, we will denote operators by a hat in this section to clarify the difference between classical and quantum quantities.

Since the (classical) coordinates q_l and p_l are canonically conjugated, their Poisson bracket evaluates to

$$\{q_l, p_{l'}\} = \delta_{l,l'}. \tag{2.30}$$

In canonical quantization we replace the coordinates with operators and the Poisson bracket with the commutator,

$$\hat{\mathcal{H}} = \sum_l \left[\frac{1}{2}\hat{p}_l^2 + \frac{1}{2}\Omega_l^2 \hat{q}_l^2\right], \qquad\qquad [\hat{q}_l, \hat{p}_{l'}] = i\hbar\delta_{l,l'}. \tag{2.31}$$

Furthermore, we define new operators

$$\hat{a}_l = \frac{1}{\sqrt{2\hbar\Omega_l}}\left(\Omega_l \hat{q}_l + i\hat{p}_l\right) \qquad \text{and} \qquad \hat{a}_l^\dagger = \frac{1}{\sqrt{2\hbar\Omega_l}}\left(\Omega_l \hat{q}_l - i\hat{p}_l\right), \tag{2.32}$$

which obey the commutation relation

$$[\hat{a}_l\,, \hat{a}_{l'}^\dagger] = \delta_{l,l'}. \tag{2.33}$$

Hence, we find for the Hamilton operator of the electromagnetic field

$$\hat{\mathcal{H}} = \sum_l \hbar\Omega_l \left(\hat{a}_l^\dagger \hat{a}_l + \frac{1}{2}\right). \tag{2.34}$$

In analogy to the quantum harmonic oscillator we can identify the operators in the Hamiltonian with the number operator for each mode $\hat{a}_l^\dagger \hat{a}_l = \hat{n}_l$. The Eigenstates of this operator determine the quanta of the electromagnetic field, which are called *photons*. As an example, $\hat{n}_l|N_l\rangle = N_l|N_l\rangle$ corresponds to N_l photons in the lth mode. Furthermore, the operator $\hat{a}_l^\dagger$ ($\hat{a}_l$) is the creation (annihilation) operator of a photon in the lth mode.

When we now come back to Eq. (2.34) we find that the number of photons determines the total energy: Each mode l can be occupied multiple times and the sum of these modes makes up the energy of the electromagnetic field. On top of that we find a constant term $\sum_l \frac{\hbar\Omega_l}{2}$. Formally this term is divergent, but since it does not contain any operators (and therefore is a constant energy shift) we neglect it from here on. Physically, this term stems from vacuum fluctuations which give rise to the Casimir effect [24], for example.

As a last step we derive the quantized electric and magnetic field. Solving Eq. (2.32) for $\hat{q}_l$ and $\hat{p}_l$ gives

$$\hat{q}_l = \sqrt{\frac{\hbar}{2\Omega_l}}\left(\hat{a}_l + \hat{a}_l^\dagger\right) \qquad \text{and} \qquad \hat{p}_l = \frac{1}{i}\sqrt{\frac{\hbar\Omega_l}{2}}\left(\hat{a}_l - \hat{a}_l^\dagger\right). \tag{2.35}$$

Replacing $\dot{q}_l = p_l$ and q_l in Eq. (2.20a) and (2.20b) by its according operators yields

$$\begin{aligned}\hat{\mathbf{E}}(\mathbf{r},t) &= i\sum_l \mathcal{E}_l \mathbf{u}_l(\mathbf{r})\left(\hat{a}_l(t) - \hat{a}_l^\dagger(t)\right)\\ &= i\sum_l \mathcal{E}_l \mathbf{u}_l(\mathbf{r})\left(\hat{a}_l(0)e^{-i\Omega_l t} - \hat{a}_l^\dagger(0)e^{i\Omega_l t}\right)\end{aligned} \tag{2.36}$$

and

$$\begin{aligned}\hat{\mathbf{B}}(\mathbf{r},t) &= \sum_l \mathcal{B}_l\left(\nabla\times\mathbf{u}_l(\mathbf{r})\right)\left(\hat{a}_l(t) + \hat{a}_l^\dagger(t)\right)\\ &= \sum_l \mathcal{B}_l\left(\nabla\times\mathbf{u}_l(\mathbf{r})\right)\left(\hat{a}_l(0)e^{-i\Omega_l t} + \hat{a}_l^\dagger(0)e^{i\Omega_l t}\right).\end{aligned} \tag{2.37}$$

Here, we have used

$$\mathcal{E}_l = \sqrt{\frac{\hbar\Omega_l}{2\epsilon_0 V_l}}, \qquad\qquad \mathcal{B}_l = \sqrt{\frac{\hbar}{2\epsilon_0 V_l \Omega_l}} \tag{2.38}$$

and the operators $\hat{a}_l(t)$ and $\hat{a}_l^\dagger(t)$ are in the Heisenberg representation. The fields are often divided in two parts $\hat{\mathbf{E}} = \hat{\mathbf{E}}^{(+)} + \hat{\mathbf{E}}^{(-)}$ in literature (a similar equation holds for the $\hat{\mathbf{B}}$-field), where the two terms correspond to the different frequency dependence $\hat{\mathbf{E}}_l^{(\pm)} \propto e^{\mp i\Omega_l t}$.

2.2 Light-Matter interaction

After we have quantized the electromagnetic field in the last section, we analyze now how a single atom interacts with the quantized electromagnetic field. Note that we omit the hat over operators from now on. It should be clear from the context if we are dealing with an operator or a number.

The total Hamiltonian is given by

$$H = H_{\text{at}} + H_{\text{em}} + H_{\text{int}}, \tag{2.39}$$

where H_{at} incorporates the atomic degrees of freedom, H_{em} is the Hamiltonian of the electromagnetic field and

$$H_{\text{int}} = -\mathbf{d} \cdot \mathbf{E}(\mathbf{R}) \tag{2.40}$$

describes the interaction between the atom and the field, where $\mathbf{d}$ is the dipole operator of the atom. We have assumed here that the wavelength of the electromagnetic field is much larger than the size of the atom[3]. This means that the field does not change considerably over the atomic length scale and we can evaluate the field at the coordinates $\mathbf{R}$ of the atom.

To keep the calculation simple we consider an atom where one transition is resonant and the electromagnetic field consists of one mode. This model is also known as the Jaynes-Cummings model [25]. Since only one atomic transition is relevant, the Hamiltonian of the atom can be described in terms of a two-level system (TLS)

$$H_{\text{at}} = E_e|e\rangle\langle e| + E_g|g\rangle\langle g| = \begin{pmatrix} E_e & 0 \\ 0 & E_g \end{pmatrix} = \frac{\hbar\Omega}{2}\sigma_z + E_0\mathbb{1}. \tag{2.41}$$

Here, we have cast the Hamiltonian in a matrix form, where

$$\sigma_z = \begin{pmatrix} 1 & 0 \\ 0 & -1 \end{pmatrix} \tag{2.42}$$

is the third Pauli matrix, $|e\rangle = (1,0)^T$ ($|g\rangle = (0,1)^T$) is the excited (ground) state, $\Omega = (E_e - E_g)/\hbar$ is the transition frequency and $E_0 = (E_e + E_g)/2$ is a constant energy offset. The Hamiltonian of the single-mode electromagnetic field is defined in analogy to the previous section as

$$H_{\text{em}} = \hbar\omega\left(a^\dagger a + \frac{1}{2}\right). \tag{2.43}$$

The next step is to evaluate the matrix elements of the dipole operator $\mathbf{d} = e\mathbf{r}$, which are given by

$$\langle j|\mathbf{d}|k\rangle = e\int \mathrm{d}^3r\, \phi_j^*(\mathbf{r})\,\mathbf{r}\,\phi_k(\mathbf{r}), \tag{2.44}$$

with the atomic wavefunction $\phi_j(\mathbf{r})$ of the jth Eigenvalue. Assuming that every wavefunction has a well-defined parity we can immediately see that all diagonal matrix elements are zero

[3] To give some numbers, the wavelength of light at optical frequencies is of the order $10^{-7}m$ whereas typical atomic radii are of the order $10^{-10}m$. The wavelength of light is thus four orders of magnitude larger than the spatial extent of an atom.

because the integrand is odd. Hence, the matrix element is only nonzero for $j \neq k$ and we find in our case

$$\langle e|\mathbf{d}|g\rangle := \mathbf{t} \qquad \langle g|\mathbf{d}|e\rangle := \mathbf{t}^*, \tag{2.45}$$

or alternatively

$$\mathbf{d} = \begin{pmatrix} 0 & \mathbf{t} \\ \mathbf{t}^* & 0 \end{pmatrix} = \mathbf{t}\sigma_+ + \mathbf{t}^*\sigma_-. \tag{2.46}$$

Here, σ_+ and σ_- are the respective atomic raising and lowering operators. The single-mode electric field is given by

$$\mathbf{E}(\mathbf{r}) = i\mathcal{E}_0\mathbf{u}(\mathbf{r})\left(a - a^\dagger\right), \tag{2.47}$$

where

$$\mathcal{E}_0 = \sqrt{\frac{\hbar\omega}{2\epsilon_0 V}}. \tag{2.48}$$

Combining everything, we find for the coupling Hamiltonian

$$H_{\text{int}} = -i\mathcal{E}_0\left[\mathbf{t}\cdot\mathbf{u}(\mathbf{R})\sigma_+ + \mathbf{t}^*\cdot\mathbf{u}(\mathbf{R})\sigma_-\right]\left(a - a^\dagger\right). \tag{2.49}$$

Rewriting $\mathbf{t}\cdot\mathbf{u}(\mathbf{R}) = |\mathbf{t}\cdot\mathbf{u}(\mathbf{R})|e^{i\varphi}$, defining

$$\mathcal{E}_0|\mathbf{t}\cdot\mathbf{u}(\mathbf{R})| := g(\mathbf{R}) \tag{2.50}$$

and furthermore setting[4] $\varphi = \pi/2$ finally yields

$$H_{\text{int}} = g(\mathbf{R})\left(\sigma_+ - \sigma_-\right)\left(a - a^\dagger\right). \tag{2.51}$$

This is the general light-matter coupling Hamiltonian in the dipole approximation, where all physical constants have been absorbed into the coupling constant $g(\mathbf{R})$.

2.2.1 Rotating-Wave-Approximation

We now examine the interaction Hamiltonian in detail. Expanding the interaction Hamiltonian as

$$H_{\text{int}} = g(\mathbf{R})\left(\sigma_+ a - \sigma_+ a^\dagger - \sigma_- a + \sigma_- a^\dagger\right) \tag{2.52}$$

generates four terms which comprise different physical processes. The term $\sigma_+ a$ ($\sigma_- a^\dagger$) describes the absorption (emission) of a photon, which sets the TLS to the excited (ground) state. The term $\sigma_+ a^\dagger$ ($\sigma_- a$), however, describes the simultaneous excitation (decay) of the TLS together with the emission (absorption) of a photon. These processes seem to violate energy conservation and are therefore very unprobable. With this heuristic statement it would be more convenient to use an interaction Hamiltonian of the form

$$H'_{\text{int}} = g(\mathbf{R})\left(\sigma_+ a + \sigma_- a^\dagger\right). \tag{2.53}$$

[4] This phase can be absorbed into the definition of the electric field, for example, since the electric field multiplied by a constant is still a solution of the wave equation Eq. (2.7).

To quantify this statement we transform H_{int} to the interaction representation, where the free Hamiltonian is given by

$$H_0 = H_{\text{at}} + H_{\text{em}} = \frac{\hbar\Omega}{2}\sigma_z + \hbar\omega a^\dagger a. \tag{2.54}$$

We have neglected here the constant energy offset for a cleaner notation. With the help of [21]

$$e^{\frac{i}{2}\Omega t\sigma_z}\sigma_- e^{-\frac{i}{2}\Omega t\sigma_z} = \sigma_- e^{-i\Omega t} \qquad \text{and} \qquad e^{ia^\dagger a\omega t} a e^{-ia^\dagger a\omega t} = a e^{-i\omega t} \tag{2.55}$$

we find for the coupling Hamiltonian in interaction representation

$$\begin{aligned} H_{\text{int}}(t) &= e^{\frac{i}{\hbar}H_0 t} H_{\text{int}} e^{-\frac{i}{\hbar}H_0 t} \\ &= g(\mathbf{R})\left(\sigma_+ a e^{-i(\omega-\Omega)t} - \sigma_+ a^\dagger e^{i(\omega+\Omega)t} - \sigma_- a e^{-i(\omega+\Omega)t} + \sigma_- a^\dagger e^{i(\omega-\Omega)t}\right). \end{aligned} \tag{2.56}$$

We can already see here that the energy-conserving terms acquire a time dependence of the form $e^{i(\Omega-\omega)t}$ and the energy-violating terms behave as $e^{i(\omega+\Omega)t}$. In the case when the TLS and the electromagnetic field are tuned on resonance $\Omega \sim \omega$ the energy-conserving terms oscillate slowly, whereas the energy-violating terms oscillate very fast. The fast oscillating terms often average out, hence the physical terms are dominant in the interaction Hamiltonian.

To support this statement even more, we recall the time evolution of a state from the last chapter Eq. (1.18),

$$|\Psi(0)\rangle = \mathcal{S}(0,-\infty)|\phi_0\rangle, \tag{2.57}$$

where the S-matrix $\mathcal{S}(0,-\infty)$ propagates an Eigenstate $|\phi_0\rangle$ of the unperturbed system at time $t \to -\infty$ to an Eigenstate of the full system $|\Psi(t)\rangle$ at time $t = 0$. Hence, the S-matrix encapsulates the effects of the interaction. Indeed, we find

$$\begin{aligned} \mathcal{S}(0,-\infty) &= T\exp\left[-\frac{i}{\hbar}\int_{-\infty}^{0} dt' H_{\text{int}}(t')\right] \\ &= T\exp\left[\frac{g(\mathbf{R})}{\hbar(\omega-\Omega)}\left(\sigma_+ a - \sigma_- a^\dagger\right) + \frac{g(\mathbf{R})}{\hbar(\omega+\Omega)}\left(\sigma_+ a^\dagger - \sigma_- a\right)\right]. \end{aligned} \tag{2.58}$$

We can see here again that the slowly oscillating terms generate the dominant contribution for $\Omega \sim \omega$, which supports the choice of

$$H'_{\text{int}} = g(\mathbf{R})\left(\sigma_+ a + \sigma_- a^\dagger\right) \tag{2.59}$$

as effective coupling Hamiltonian. Since the fast oscillating terms are neglected here, this procedure is called *Rotating Wave Approximation (RWA)*. Note that this approximation is only valid when $|g(\mathbf{R})| < |\hbar(\Omega+\omega)|$, i.e. for sufficiently small coupling constants. In the regime of ultra-strong coupling the fast-rotating terms cannot be neglected anymore and the RWA breaks down.

2.3 Waveguide Quantum Electrodynamics

As discussed in the introduction, light-matter interaction on the quantum level are a key element of prospective technologies like quantum information processing [7, 9], quantum metrology [10] or quantum networks [11]. These technologies rely on entanglement over large distances, distributed by single photons. The building block of most of these systems can be described in the context of *waveguide quantum electrodynamics* (waveguide QED), i.e. a high-fidelity one-dimensional (1D) waveguide with an embedded quantum emitter (e.g. a quantum dot, qubit, cold atom...). In this section we present the experimental realizations of waveguide QED together with a simplified model which is used in this thesis.

2.3.1 Experimental realizations

There exists a variety of different experimental realizations of the waveguide QED setup nowadays, which work in different regimes and employ various waveguiding techniques and quantum emitters. One of the first successful realizations was achieved in the microwave regime, where a superconducting qubit acting as quantum emitter is coupled to a 1D transmission line [28–32]. At optical wavelengths, semiconductor quantum dots are widely used as quantum emitters [33–35]. They have been successfully coupled to photonic nanowires [36] and line defect waveguides in photonic crystal slabs [34], where recently unity coupling efficiency has been reported [37].

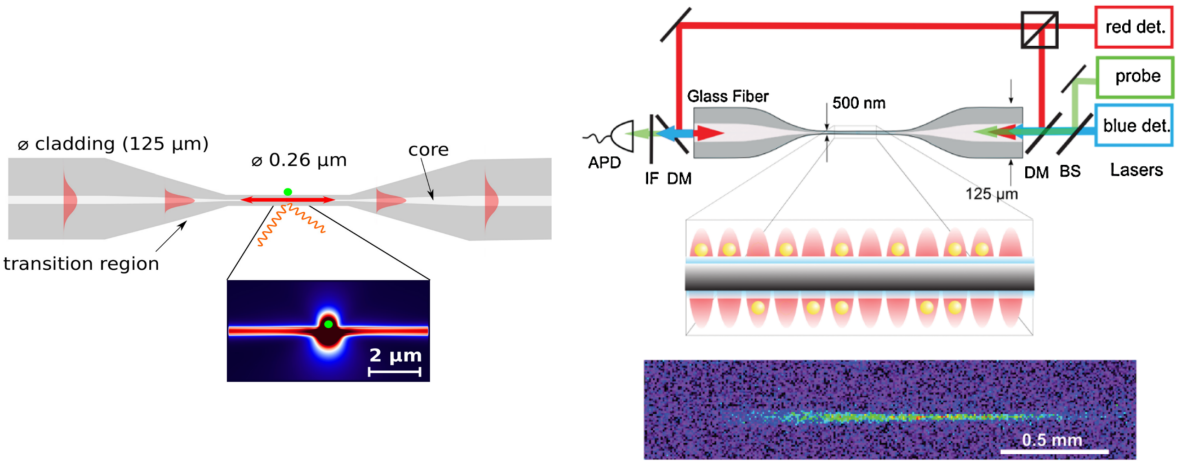

(a) NV center in a nanodiamond placed next to fiber

(b) Caesium atoms trapped next to fiber

Figure 2.1: *(a) Schematic setup of a NV center in a nanodiamond placed next to a tapered fiber by using the tip of an atomic force microscope. The inset shows a finite difference time-domain simulation of the intensity distribution of the NV center coupled to the fiber (adapted from Ref. [26])*
(b) Caesium atoms trapped next to a tapered fiber by two detuned laser beams (top), together with a fluorescence image of the trapped atomic ensemble (bottom) (adapted from Ref. [27]).

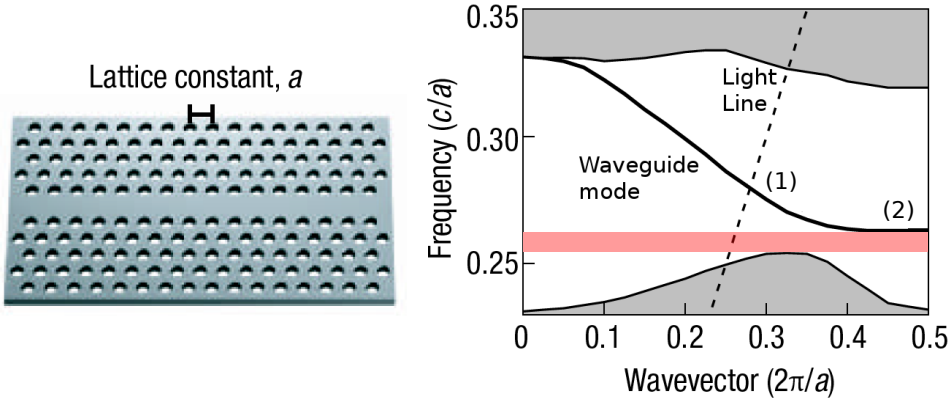

Figure 2.2: *Left: Line defect waveguide in a photonic crystal slab. Right: Dispersion relation of the waveguiding mode, which exhibits a linear regime (1), a slow-light regime (2) and a photonic band gap (red shaded region) (adapted from Ref. [47]).*

Quantum dots can also be coupled to metallic nanowires to generate plasmons [38], which can then be transformed to photons in hybrid systems [39]. Nitrogen-vacancy (NV) centers in diamond are another popular choice for quantum emitters [40] and have been successfully coupled e.g. to a tapered fiber [26] (see Fig. 2.1 (a)). Growing interest has been received in the last couple of years by ultracold atoms, where efficient coupling to a fiber [27] and to a line defect waveguide in a photonic crystal [41] has been demonstrated (see Fig. 2.1 (b)). Recent experiments with a thin glass capillary filled with a dye solution [42] promise yet another way to reach strong atom-photon interaction in the waveguide QED setup.

At this point we would also like to present a special class of waveguides, which are based on a periodic arrangement of the environment (e.g. line defect waveguides in photonic crystal slabs [43, 44]) or resonators (e.g. coupled-resonator optical waveguides (CROW) [45] or side-coupled integrated spaced sequence of resonators (SCISSOR) [46]. These waveguides exhibit properties which are similar to solids with a crystalline structure, i.e. a band structure which could feature a band edge. As an example, we have shown the dispersion relation of a line defect waveguide in a photonic crystal slab in Fig. 2.2. We can see here that the dispersion relation can be approximated by a linear dispersion relation in region (1), but becomes very flat in region (2). This indicates a slow-light regime, where the photons travel with a velocity $v \ll c$. On top of that, the waveguide exhibits a photonic band gap (red shaded region), where photonic excitations are forbidden.

2.3.2 Theoretical model

We have already discussed that the model of waveguide QED features a 1D waveguide with an embedded quantum emitter, as sketched in Fig. 2.3. In this section we lay down the theoretical description of the model and derive the corresponding Hamiltonian

$$H = H_{\mathrm{ph}} + H_{\mathrm{qe}} + H_{\mathrm{int}}, \tag{2.60}$$

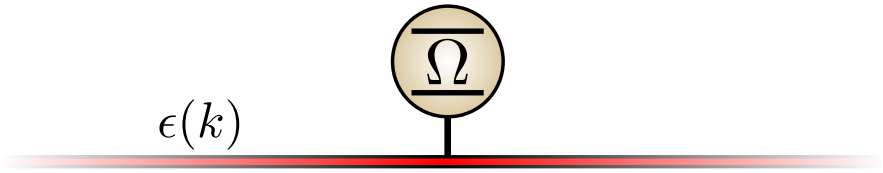

Figure 2.3: *Sketch of the theoretical model: A two-level system with resonance energy Ω coupled to a 1D waveguide with dispersion relation $\epsilon(k)$.*

where the individual terms describe the photons in the waveguide, the state of the quantum emitter and the interaction between the two, respectively.

The Hamiltonian of the photons is given by

$$H_{\mathrm{ph}} = \int \frac{\mathrm{d}k}{2\pi} \epsilon(k) a_k^\dagger a_k, \tag{2.61}$$

where $a_k^\dagger$ (a_k) is a photonic (bosonic) creation (annihilation) operator and $\epsilon(k)$ is the mode spectrum. Since there exists a variety of waveguides which employ lattice effects to generate a photonic band structure, we call $\epsilon(k)$ *dispersion relation*. In this context, the quantum number k is equivalent to the (crystal) momentum of the photon. The quantum emitter is modeled here as a two-level system (TLS), to keep the calculations simple. The corresponding Hamiltonian is given by

$$H_{\mathrm{qe}} = \frac{\Omega}{2} \sigma_z, \tag{2.62}$$

where Ω is the level splitting. Assuming that the rotating wave approximation is valid, we find for the interaction Hamiltonian

$$H_{\mathrm{int}} = \int \frac{\mathrm{d}k}{2\pi} \left(U(k) a_k^\dagger \sigma_- + U^*(k) a_k \sigma_+ \right), \tag{2.63}$$

with the waveguide-TLS coupling constant $U(k)$. The Fourier-transformed coupling constant $\tilde{U}(x)$ describes the spatial profile of the coupling. We assume here that the spatial coupling can be described by a δ-function, $\tilde{U}(x) = U\delta(x)$, which gives $U(k) = U = \mathrm{const}$. To simplify the Hamiltonian even more we set U real, which leaves us with the total Hamiltonian

$$H = \int \frac{\mathrm{d}k}{2\pi} \epsilon(k) a_k^\dagger a_k + \frac{\Omega}{2} \sigma_z + U \int \frac{\mathrm{d}k}{2\pi} \left(a_k \sigma_+ + \mathrm{h.c.} \right). \tag{2.64}$$

We employ two dispersion relations in this thesis, a cosine dispersion relation and a linear dispersion relation,

$$\epsilon_{\cos}(k) = -2J \cos(k) \qquad \epsilon_{\mathrm{lin},\mu}(k) = \mu v k. \tag{2.65}$$

The cosine-shaped dispersion relation, where J defines the bandwidth $\Lambda = 4J$, exhibits band edges and a slow-light regime and is therefore suited to describe lattice-based waveguides like CROWs or line defect waveguides in photonic crystals. For energies far away from the band

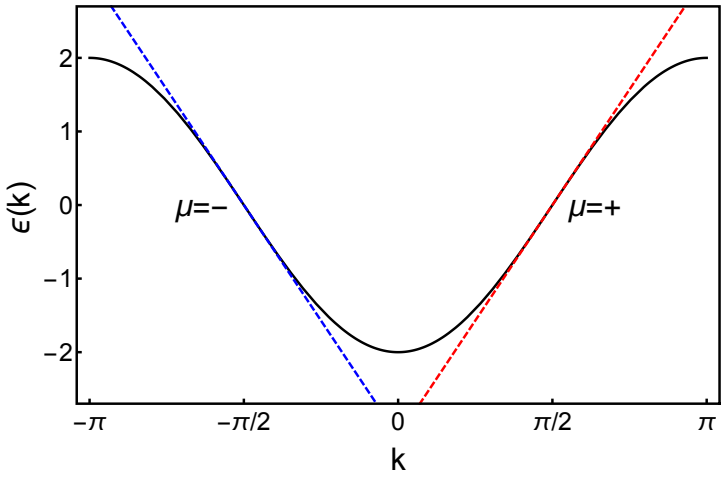

Figure 2.4: *Plot of $\epsilon_{cos}(k)$ for $J = 1$, together with the linear approximation around $\epsilon_{cos}(k) = 0$. We have also indicated the according chirality μ of the linearized dispersion relation.*

edge, the dispersion relation can often be linearized, which leads to the dispersion relation on the right (where we have neglected the energy offset). Here, v is the group velocity of the photons in the waveguide and $\mu = \pm$ is the new quantum number *chirality*, which discriminates between right- and leftmoving photons. We would like to point out that both dispersion relations are defined here in the field limit, i.e. there is no intrinsic length scale like lattice spacing, for example[5]. We have plotted both dispersion relations in Fig. 2.4, where the linear dispersion relation appears as an approximation of the cosine dispersion relation around $\epsilon_{\cos}(k) = 0$.

Moreover, the Hamiltonian conserves the excitation number

$$N = \int \frac{\mathrm{d}k}{2\pi} a_k^\dagger a_k + \frac{1}{2}\left(\sigma_z + 1\right). \tag{2.66}$$

Here, the first term counts the number of photons in the waveguide, n, and the second term gives zero or one for a TLS in the ground or excited state, respectively. This means that a state with n photons in the waveguide and a TLS in the ground state has the same excitation number as a state with $n-1$ photons and a TLS in the excited state. Furthermore, since $[H, N] = 0$ the Hilbert space of the Hamiltonian factorizes into subspaces of constant N, which allows us to treat these subspaces separately. Indeed, we only consider the cases $N = 1$ (which corresponds to states with one photon plus a TLS in the ground state or no photon plus an excited TLS) and $N = 2$ (the same states as before, but with one additional photon) throughout this thesis. At this point we would like to point out a crucial difference between the two cases (for simplicity, we start with a TLS in the ground state): For $N = 1$ a photon in the waveguide can be absorbed and reemitted at a later time by the TLS. For $N = 2$ (i.e. two photons in the

[5] In fact, the linear dispersion relation can only be defined in the field limit whereas the cosine dispersion relation stems originally from a tight-binding chain with nearest neighbor hopping. In this case, the momentum is usually measured in terms of the inverse lattice spacing $[k] = a^{-1}$.

waveguide), however, the TLS can absorb one photon, but not the other one. The interaction of the second photon with the TLS is therefore modified, which renders the system nonlinear in the presence of two and more photons. This nonlinearity induces an effective photon-photon interaction and is one of the effects which we will study in this thesis.

At some points throughout this thesis it is useful to back up the calculations with numerics. In these cases, we use a Hamiltonian in real space, where the waveguide is realized by a tight-binding chain with nearest neighbor hopping and unit lattice spacing,

$$H_{\mathrm{tb}} = -J \sum_i \left(a_i^\dagger a_{i+1} + \mathrm{h.c.} \right) + \frac{\Omega}{2} \sigma_z + U \left(a_0 \sigma_+ + \mathrm{h.c.} \right). \tag{2.67}$$

Here, the index i indicates the location of the photon in the waveguide and $a_i^\dagger$ is the corresponding creation operator. Note that this model corresponds to the cosine-shaped dispersion relation shown above, which enables us to compare both approaches. Finally, we would like to point out that Eq. (2.64) is the main Hamiltonian in this thesis and we will make it clear in the text when Eq. (2.67) is used.

3 FEYNMAN DIAGRAMS IN WAVEGUIDE QUANTUM ELECTRODYNAMICS

We present here the theoretical framework which is used throughout this thesis. This framework employs quantum-field theoretical Green's functions in the single- and two-excitation sector, where a Feynman diagram representation enables us to gain insight into the physical processes. We calculate in both sectors the full Green's function for an arbitrary dispersion relation and find a self-consistent T-Matrix equation for the Green's function in the two-excitation sector. With the help of these Green's functions we calculate the scattering matrix and the spectral density and find a Fano resonance between the excited TLS and the additional photon in the two-excitation sector.

3.1 Introduction

The theoretical foundation of waveguide QED was derived after the first successful experimental realizations with superconducting circuits [48] and led to the Hamiltonian Eq. (2.64). In the beginning, the focus was on the scattering behavior of single photons with the TLS [49, 50]. Here, it was found that a careful tuning of the photonic and atomic energies can lead to a vanishing transmission, i.e. the TLS acts as an energy-dependent mirror. The scattering matrix for two photons was derived two years later by employing a sophisticated Bethe Ansatz [51, 52]. In this case, it was found that the TLS induces a correlation between the photons (i.e. photon bunching). The reason behind this effect is the nonlinear behavior of the system in the presence of two or more photons (this was discussed in Sec. 2.3.2).

The drawback of this approach was the use of Bethe Ansatz, which leads to lengthy and complicated calculations. This paved the way to the development of other frameworks that rely on the input-output formalism [53], master equations [54], quantum field theory [55, 56] and full-counting statistics [57]. With the help of these new tools, it was possible to expand the model and calculate the scattering matrix for N photons [58], multi-level systems [59, 60] and for TLS which are placed in a cavity [61] or a whispering gallery resonator [62]. Furthermore, there exist studies for two spatially separated TLS [63], for a TLS that is coupled to an external

bath [64, 65] and even general statements on the form of the scattering matrix [66]. Other works focused on the simpler system of a waveguide coupled to a single TLS and investigated the time-domain behavior of the photons. Here, interesting effects like the stimulated emission from the TLS [67] or the full inversion by a single photon [68] have been found. On top of that, there exist frameworks to determine the time-evolution of Gaussian one- and two-photon wavepackets [69–71], which support the behavior predicted by the scattering solutions.

All of the works presented so far have in common that they employ a linear dispersion relation. We have seen in Sec. 2.3.1 that there exist waveguides without a linear dispersion relation and moreover exhibiting a slow-light regime and a photonic band gap. It has been shown that the appearance of a photonic band gap leads to the formation of a polaritonic Eigenstate in the coupled atom-waveguide system [72, 73]. This Eigenstate is called atom-photon bound state and has the intriguing property that it lies in the photonic band gap and hence does not decay. Since the atom-photon bound state is not captured within theories with a linear dispersion relation (which has no band edge), we expect that the physics in the vicinity of the band edge differs from that described by a linear dispersion relation.

This can be seen in the case of a quadratic dispersion relation in the scattering matrix: Here, the dip in the transmission spectrum indicating the energy dependent mirror acquires a different form when the energy is close to the band edge [74]. Another way to get a nonlinear dispersion relation is by modeling the waveguide as a tight-binding chain with nearest neighbor hopping, which is equivalent to a cosine-shaped dispersion relation. In this case, numerical time-domain simulations in the one- and two-photon sector have been performed [75–80], which have also been extended to more complicated quantum emitters [81]. These simulations have shown the effect of interaction-induced radiation trapping, i.e. that the atom-photon bound state can be excited by a carefully tuned two-photon pulse. Furthermore, the effect of ultrastrong coupling has been examined [82], together with the effects of the rotating wave approximation.

We present here a Green's function approach to waveguide QED which employs Feynman diagrams to display the physical processes in the perturbation theory. We calculate the exact Green's function for an arbitrary dispersion relation in the single- and two-excitation sector. In the two-excitation sector the Green's function is defined in terms of a self-consistent T-Matrix equation. In general, this equation has to be solved numerically, but we find that it can be solved exactly in special cases. From a physical point of view we focus on the calculation of the scattering matrix and the spectral density of the TLS in both sectors, where a Fano resonance appears in the two-excitation spectral density.

3.2 Green's functions

We start by presenting the Green's functions for the Hamiltonian given by Eq. (2.64) in the single- and two-excitation sector. The Green's functions have been initially derived by C. Stawiarski in her diploma thesis [83] by means of the coherent-state path integral. Based on these Green's functions, we present an alternative derivation by means of Feynman diagrams[1] [84]. In order to connect both approaches, we begin the derivation with the starting point of the path integral approach.

[1]The work presented in this chapter was done in collaboration with T. Sproll.

The first step is to replace the spin operators in Eq. (2.64) with the corresponding auxiliary-fermion representation, i.e.

$$\sigma_z = f^\dagger f - g^\dagger g, \qquad \sigma_+ = f^\dagger g, \qquad \sigma_- = g^\dagger f, \tag{3.1}$$

where the operators fulfill the completeness relation $f^\dagger f + g^\dagger g = 1$. Here, $f^\dagger$ and $g^\dagger$ are the creation operators of the excited and ground state of the TLS, respectively. The deeper reason behind the auxiliary-fermion representation is that it enables us to employ fermionic coherent states in the path integral instead of spin coherent states. In this representation, the Hamiltonian is given by

$$H = \int \frac{\mathrm{d}k}{2\pi} \epsilon(k) a_k^\dagger a_k + \frac{\Omega}{2}\left(f^\dagger f - g^\dagger g\right) + U \int \frac{\mathrm{d}k}{2\pi}\left(a_k^\dagger g^\dagger f + h.c.\right). \tag{3.2}$$

The Green's function is then defined as

$$G(t_f - t_i) = -i\langle f | e^{-\int_{t_i}^{t_f} H(t)dt} | i\rangle, \tag{3.3}$$

where $|i\rangle$ and $|f\rangle$ are the initial and final states. Although this equation is different from the definition given in Eq. (1.19), they both describe the same quantity. In a heuristic way, this can be seen from the fact that both quantities describe the propagation of states from an initial to a final time: In Chapter 1 this was achieved by means of creation and annihilation operators in the Heisenberg representation, whereas here the propagation is cast in the form of a time-evolution operator. Furthermore, decomposing the initial and final states into a product state of photonic and atomic excitation, $|i/f\rangle = |\mathrm{ph}_{i,f}\rangle \otimes |\mathrm{TLS}_{i/f}\rangle$ enables us to cast the Green's function in a matrix form in the subspace of the TLS states. Indeed, setting

$$|\mathrm{TLS}\rangle = \begin{pmatrix} |e\rangle \\ |g\rangle \end{pmatrix}, \tag{3.4}$$

where $|e\rangle = f^\dagger|0\rangle$ ($|g\rangle = g^\dagger|0\rangle$) is the excited (ground) state of the TLS leads to the matrix Green's function

$$G = \begin{pmatrix} G_\mathrm{e} & G_\mathrm{ab} \\ G_\mathrm{em} & G_\mathrm{w} \end{pmatrix}. \tag{3.5}$$

Here, G_e describes the propagation of an excited TLS from an initial to a final time. Thus it is called the *TLS-Green's function*. The other diagonal Green's function, G_w, describes the propagation of a TLS in the ground state. Thus, this Green's function describes the dynamics of the photons in the waveguide and is called the *waveguide Green's function*. The last two Green's functions describe the transition from the ground state to the excited state and vice versa. Since these processes are accompanied by the absorption or emission of a photon we call these Green's functions the *absorption Green's function* (G_ab) and the *emission Green's function* (G_em), respectively. We would like to point out that this matrix representation describes only the state of the TLS and makes no statements about the additional photons in the waveguide.

A key feature of this chapter is the Feynman diagram representation of the Green's functions. From Eq. (3.2) we can see that three diagonal contributions exist: photons in the waveguide

Photons	$\|e\rangle$	$\|g\rangle$	Vertex
			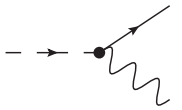

Table 3.1: *Table of the representations for the individual species and the interaction vertex in terms of Feynman diagrams.*

and a TLS in the excited state or the ground state. We depict these excitations by a wavy line, a dashed line and a solid line, respectively. Additionally, the interaction can be cast in the form of a vertex, which transforms a dashed line into a wavy and a solid one and vice versa. As an overview, we have summarized these representations in Tab. 3.1. At this point, this diagrammatic representation is merely heuristic and not connected to formulas. The connection will be made in the next sections, when we present the Green's functions in the single- and two-excitation sector.

3.2.1 Single-excitation sector

We start with calculations in the single excitation sector, where we have either an excited TLS or a photon in the waveguide. We focus here on the calculation of the TLS-Green's function G_e, since it turns out that this Green's function serves as a building block for all other Green's functions.

From the path integral approach we find for the TLS-Green's function in time-domain [83, 84]

$$\begin{aligned} {}_1G_\mathrm{e}(t_f - t_i) = &- i \sum_{r=0}^{\infty} \left(iU\right)^{2r} \int_0^{t_i - t_f} \mathrm{d}t_{2r} \int_0^{t_{2r}} \mathrm{d}t_{2r-1} .... \int_0^{t_2} \mathrm{d}t_1 \\ &\times {}_1G_\mathrm{e}^0(t_f - t_i - t_{2r}) \left[\int \frac{\mathrm{d}k}{2\pi} {}_1G_\mathrm{w}^0(k, t_{2r} - t_{2r-1}) \right] \\ &\times {}_1G_\mathrm{e}^0(t_{2r-1} - t_{2r-2}) \dots {}_1G_\mathrm{e}^0(t_1 - t_0) \end{aligned} \tag{3.6}$$

where

$${}_1G_\mathrm{e}^0(t' - t) = e^{-i\frac{\Omega}{2}(t'-t)}, \qquad {}_1G_\mathrm{w}^0(k, t' - t) = e^{i\frac{\Omega}{2}(t'-t)} e^{-i\epsilon(k)(t'-t)}. \tag{3.7}$$

Here, the subscript on the left indicates that the Green's functions are defined in the single-excitation sector. From a physical point of view, these free Green's functions describe the propagation of an excited TLS,

$${}_1G_\mathrm{e}^0(t' - t) = e^{-i\frac{\Omega}{2}(t'-t)} = \quad \text{ 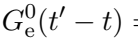 }, \tag{3.8}$$

and the simultaneous propagation of a TLS in the ground state together with a photon in the waveguide,

$${}_1G_\mathrm{w}^0(k, t' - t) = e^{i\frac{\Omega}{2}(t'-t)} e^{-i\epsilon(k)(t'-t)} = \quad \text{ 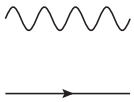 }, \tag{3.9}$$

from time t to t'. With the help of these diagrammatic representations, we can rewrite the perturbation series as

$${}_1G_\mathrm{e}(t_f - t_i) = -i\Big\{$$

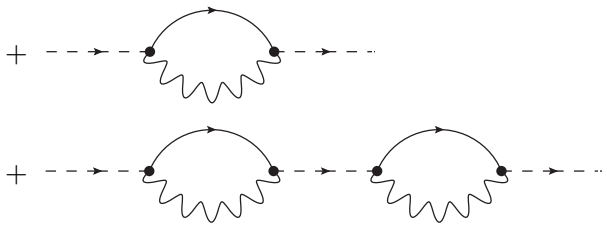

$$+\ldots\Big\}. \tag{3.10}$$

Here, each interaction vertex comes with a factor iU and induces an integration over the intermediate times. Furthermore, each photonic line which is sandwiched between interaction vertices implies an integration over the corresponding momentum. From this diagrammatic representation, the physics behind the perturbation series given by Eq. (3.6) becomes immediately clear: The initially excited TLS emits a photon and with this decays to the ground state. This photon is then reabsorbed at a later time, exciting the TLS again. This process is repeated n times in nth order perturbation theory.

The perturbation series can be greatly simplified by Fourier transforming the expression to frequency domain. Due to the convolution theorem the internal time integrations transform to a simple product, which gives

$${}_1G_\mathrm{e}(\omega) = {}_1G_\mathrm{e}^0(\omega) \sum_{r=0}^{\infty} \left(U^2 \int \frac{\mathrm{d}k}{2\pi} {}_1G_\mathrm{w}^0(k,\omega) {}_1G_\mathrm{e}^0(\omega) \right)^r . \tag{3.11}$$

The free Green's functions are given in frequency domain by

$${}_1G_\mathrm{e}^0(\omega) = \frac{1}{\omega - \Omega/2 + i\delta} =$$

 (3.12)

and

$${}_1G_\mathrm{w}^0(k,\omega) = \frac{1}{\omega + \Omega/2 - \epsilon(k) + i\delta} =$$

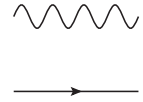 . (3.13)

Here, the additional factor $+i\delta$ is understood in the limit $\delta \to 0^+$ and indicates that we are working with retarded Green's functions. The single ω dependency of ${}_1G_\mathrm{w}^0(k,\omega)$ stems from the fact that ${}_1G_\mathrm{w}^0(k, t'-t)$ propagates a TLS in the ground state and a photon in the waveguide from the same initial time t to the same final time t'. Hence, it depends only on one time difference $\tau = t' - t$. The perturbation series in frequency domain can be derived from Eq. (3.10) in a similar way as in the time domain, but here the interaction vertices contribute a factor U, the energy ω is conserved in all terms and the prefactor $-i$ has to be omitted.

The perturbation series in Eq. (3.11) can be recast in the form of a self-consistent Dyson series[2],

$$ {}_1G_\mathrm{e}(\omega) = {}_1G_\mathrm{e}^0(\omega) + U^2 {}_1G_\mathrm{e}^0(\omega) \left[\int \frac{\mathrm{d}k}{2\pi} {}_1G_\mathrm{w}^0(k;\omega) \right] {}_1G_\mathrm{e}(\omega), \tag{3.14} $$

or alternatively in a diagrammatic form

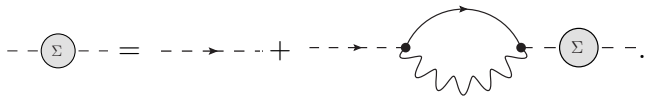

(3.15)

The Dyson equation can be readily solved as

$$ {}_1G_\mathrm{e}(\omega) = \frac{1}{\omega - \Omega/2 - {}_1\Sigma(\omega)}, \tag{3.16} $$

where the self-energy is given by

$$ {}_1\Sigma(\omega) = U^2 \int \frac{\mathrm{d}k}{2\pi} {}_1G_\mathrm{w}^0(k;\omega) = $$

. (3.17)

This is the first major result in this chapter: We have found a self-consistent solution for the TLS-Green's function in the single excitation sector, where the self-energy is defined by a bubble-diagram consisting of a photon in the waveguide together with a TLS in the ground state.

Based on the above discussion, we find for the full waveguide Green's function (i.e. a photon in the waveguide and a TLS in the ground state as initial and final state)

$$ {}_1G_\mathrm{w}(k_f, k_i;\omega) = {}_1G_\mathrm{w}^0(k_i;\omega) 2\pi\delta_{k_i,k_f} + U^2 {}_1G_\mathrm{w}^0(k_i;\omega)\, {}_1G_\mathrm{e}(\omega)\, {}_1G_\mathrm{w}^0(k_f;\omega), \tag{3.18} $$

which can be cast in a diagrammatic form as

$$ {}_1G_\mathrm{w}(k_f, k_i;\omega) = $$

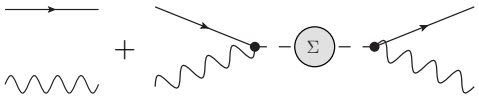

. (3.19)

Again, the diagrammatic form clarifies the physical processes behind Eq. (3.18): The full waveguide Green's function consists of a term describing the free propagation of the photon in the waveguide and one term which takes the scattering of the photons on the renormalized TLS into account.

To complete the discussion of the single-excitation sector, the absorption and emission Green's function are given by

$$ {}_1G_\mathrm{ab}(k_i;\omega) = U {}_1G_\mathrm{w}^0(k_i;\omega)\, {}_1G_\mathrm{e}(\omega) = $$

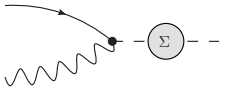

(3.20)

and

$$ {}_1G_\mathrm{em}(k_f;\omega) = U {}_1G_\mathrm{e}(\omega) {}_1G_\mathrm{w}^0(k_f;\omega) = $$

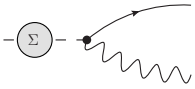

, (3.21)

where the physics behind the diagrams should be clear from the discussion before.

[2] See also Sec. 1.3.

3.2.2 Two-excitation sector

We turn now to the calculation of the Green's function in the two-excitation sector. Again, we focus mostly on the calculation of the TLS-Green's function as it is once more the building block of the other Green's functions. Furthermore, we recall that the TLS can only carry one excitation, which renders the system nonlinear in the presence of two or more photons (cf. Sec. 2.3.2). Due to the nonlinear behavior, the Green's function in the two-excitation sector cannot be obtained by merely taking the square of the single-excitation Green's functions. We will later see in the diagrammatic representation of the perturbation series how the nonlinearity emerges.

To shorten the presentation, we skip the Green's function in time domain and immediately advance to the frequency domain. Here, the perturbation series for the TLS-Green's function is given by

$$\begin{aligned} {}_2G_{\mathrm{e}}(k_f,k_i;\omega) =& {}_2G_{\mathrm{e,r}}(k_i;\omega)2\pi\delta_{k_i,k_f} \\ &+ U^2\, {}_2G_{\mathrm{e,r}}(k_i;\omega)\, {}_2G^0_{\mathrm{w}}(k_f,k_i;\omega)\, {}_2G_{\mathrm{e,r}}(k_f;\omega) \\ &+ U^4 \int \frac{\mathrm{d}k}{2\pi}\, {}_2G_{\mathrm{e,r}}(k_i;\omega)\, {}_2G^0_{\mathrm{w}}(k_i,k;\omega)\, {}_2G_{\mathrm{e,r}}(k;\omega)\, {}_2G^0_{\mathrm{w}}(k,k_f;\omega)\, {}_2G_{\mathrm{e,r}}(k_f;\omega) \\ &+ \dots, \end{aligned} \tag{3.22}$$

where

$${}_2G^0_{\mathrm{w}}(k,k';\omega) = \frac{1}{\omega + \Omega/2 - \epsilon(k) - \epsilon(k') + i\delta} \tag{3.23}$$

is the free waveguide Green's function and

$${}_2G_{\mathrm{e,r}}(k;\omega) = \frac{1}{\omega - \Omega/2 - \epsilon(k) + i\delta - {}_2\Sigma(k;\omega)} \tag{3.24}$$

is a partly[3] renormalized TLS-Green's function. Here, the self-energy ${}_2\Sigma(k;\omega)$ is given by

$${}_2\Sigma(k;\omega) = U^2 \int \frac{\mathrm{d}k'}{2\pi}\, {}_2G^0_{\mathrm{w}}(k,k';\omega). \tag{3.25}$$

Although we cannot represent Eq. (3.22) in a closed form, we can cast it in the form of a self-consistent T-Matrix equation. Explicitly, we find

$${}_2G_{\mathrm{e}}(k_f,k_i;\omega) = {}_2G_{\mathrm{e,r}}(k_i;\omega)2\pi\delta_{k_i,k_f} + {}_2G_{\mathrm{e,r}}(k_i;\omega)\, T(k_f,k_i;\omega)\, {}_2G_{\mathrm{e,r}}(k_f;\omega) \tag{3.26}$$

with the T-matrix

$$T(k_f,k_i;\omega) = U^2\, {}_2G^0_{\mathrm{w}}(k_f,k_i;\omega) + U^2 \int \frac{\mathrm{d}k}{2\pi}\, {}_2G^0_{\mathrm{w}}(k,k_i;\omega)\, {}_2G_{\mathrm{e,r}}(k;\omega)\, T(k_f,k;\omega). \tag{3.27}$$

The two equations above are the second major result in this chapter: They describe self-consistently the TLS-Green's function in the two-excitation sector for an arbitrary dispersion

[3] The exact form of this renormalization is shown by means of the Feynman diagram representation in the next section.

relation. Although we have not found an analytical solution to Eq. (3.27), a numerical solution can be readily obtained by way of discretizing the convolution integral. Later on we will see that the TLS-Green's function can be calculated exactly for certain special cases.

Before we continue to the diagrammatic representation of the TLS-Green's function, we briefly present the remaining Green's functions. In analogy to the single-excitation sector, the full waveguide Green's function can be obtained by attaching free waveguide Green's functions to the full TLS-Green's function and adding the free propagation,

$$\begin{aligned} {}_2G_{\mathrm{w}}(\omega, k_f, p_f, k_i, p_i) =& {}_2G^0_{\mathrm{w}}(k_i, p_i; \omega) \left[(2\pi)^2 \delta_{k_i,k_f}\delta_{p_i,p_f} + (2\pi)^2 \delta_{k_i,p_f}\delta_{p_i,k_f}\right] \\ &+ U^2\, {}_2G^0_{\mathrm{w}}(\omega, k_i, p_i)\, {}_2G^{\mathrm{sym}}_{\mathrm{e}}(k_i, p_i, k_f, p_f; \omega)\, {}_2G^0_{\mathrm{w}}(\omega, k_f, p_f), \end{aligned} \tag{3.28}$$

where the TLS-Green's function has been symmetrized as

$${}_2G^{\mathrm{sym}}_{\mathrm{e}}(k_i, p_i, k_f, p_f; \omega) = {}_2G_{\mathrm{e}}(k_f, k_i; \omega) + {}_2G_{\mathrm{e}}(k_f, p_i; \omega) + {}_2G_{\mathrm{e}}(p_f, k_i; \omega) + {}_2G_{\mathrm{e}}(p_f, p_i; \omega). \tag{3.29}$$

Furthermore, the emission and absorption Green's functions are given by

$${}_2G_{\mathrm{em}}(k_i, k_f, p_f; \omega) = U \left[{}_2G_{\mathrm{e}}(p_f, k_i; \omega) + {}_2G_{\mathrm{e}}(k_f, k_i; \omega)\right] {}_2G^0_{\mathrm{w}}(k_f, p_f; \omega) \tag{3.30}$$

and

$${}_2G_{\mathrm{ab}}(k_i, p_i, k_f; \omega) = U\, {}_2G^0_{\mathrm{w}}(k_i, p_i; \omega) \left[{}_2G_{\mathrm{e}}(k_f, k_i; \omega) + {}_2G_{\mathrm{e}}(k_f, p_i; \omega)\right] \tag{3.31}$$

and have the same interpretation as in the single excitation sector.

Feynman diagram representation

We proceed now to the representation of the TLS-Green's function in terms of Feynman diagrams, focusing on the individual terms in the perturbation series and their physical interpretation. The building blocks of the perturbation series are the free waveguide Green's function ${}_2G^0_{\mathrm{w}}(k, k'; \omega)$ and the partly renormalized TLS Green's function ${}_2G_{\mathrm{e,r}}(k; \omega)$. Both Green's functions depend only on one frequency, hence they propagate the particles simultaneously from one starting time t to one end time t' (in the same fashion as ${}_1G^0_{\mathrm{w}}(k, \omega)$ in the single particle sector). Explicitly, the free waveguide Green's function

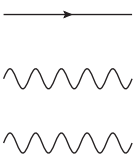

$${}_2G^0_{\mathrm{w}}(k, k'; \omega) = \tag{3.32}$$

describes the propagation of two photons with momenta k and k' together with a TLS in the ground state, and the partly renormalized TLS Green's function

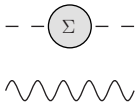

$${}_2G_{\mathrm{e,r}}(k; \omega) = \tag{3.33}$$

describes the propagation of an excited and renormalized TLS together with an additional photon in the waveguide. The self-energy appearing in ${}_2G_{\mathrm{e,r}}$ can be expressed diagrammatically as

$${}_2\Sigma(k;\omega) = U^2 \int \frac{\mathrm{d}k'}{2\pi}\, {}_2G^0_{\mathrm{w}}(k,k';\omega) =$$

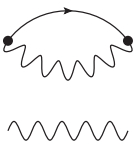

(3.34)

and includes the bubble-like renormalization which appears also in the single-excitation sector.

With the help of these basic Green's functions, we can represent the perturbation series for the full TLS-Green's function as

$${}_2G_{\mathrm{e}}(k,k';\omega) =$$

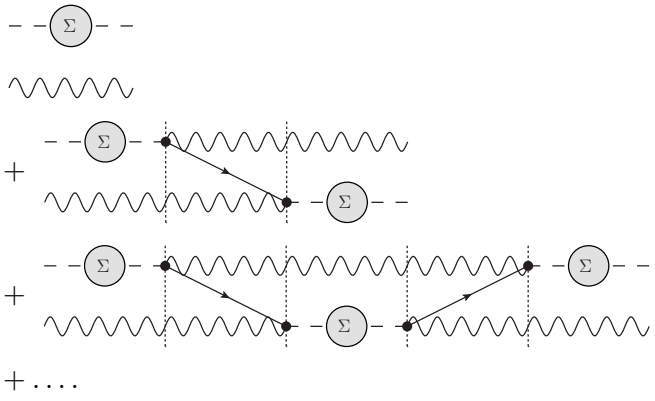

(3.35)

Here, the dotted vertical lines serve as a separator for the basic equal-time Green's functions. Each vertex provides a factor of U and photonic lines sandwiched between two interaction vertices imply an integration over the corresponding momentum. Furthermore, photonic lines which are cut by a vertical dotted line (but not by an interaction vertex) conserve momentum. At this point some readers might be confused by the appearance of equal-time Green's functions in the perturbation series. We have laid down the way to the equal-time Green's functions in Appendix A to clarify the appearance.

The diagrammatic representation of ${}_2G_{\mathrm{e}}(k,k';\omega)$ provides a clear physical interpretation of every term in the perturbation series. The first term is trivial and describes the propagation of an excited TLS (renormalized by the bubble-diagrams) together with an additional photon in the waveguide. In the second term, an excited TLS and an additional photon are created, and after a certain time the TLS emits a photon and is reset to the ground state. This enables the TLS to absorb the other, initially free photon, thus setting the TLS to the excited state whereas the other (emitted) photon propagates freely. In the third term the TLS emits a photon which is reabsorbed at a later time (upper line). During the propagation of this intermediate photon, however, the TLS is temporarily excited by the initial photon (lower line). This process of generating intermediate photons is repeated over and over again in higher order terms.

Furthermore, we are able to identify the origin of the nonlinear behavior of the system at this point. For a linear system the two-excitation Green's function would factorize into two single-excitation Green's function. This would lead to a double excited quantum emitter, which is not

possible in the case of a TLS[4]. Thus, the two-excitation Green's function must guarantee that the TLS cannot be excited by more than one photon at a time. In fact, since the perturbation series consists of the retarded, equal-time Green's functions ${}_2G^0_{\mathrm{w}}(k,k';\omega)$ and ${}_2G_{\mathrm{e,r}}(k;\omega)$, the TLS is at all times either in the ground state or in the excited state, but never excited twice at the same time. Hence, the nonlinearity emerges.

3.3 Properties of the Green's function in the single-excitation sector

After having presented the Green's functions in the previous section, we turn now to the analysis of their properties. This section is devoted to the analysis of the Green's functions in the single-excitation sector, where we focus on the spectral density of the TLS-Green's function and the calculation of the scattering matrix.

3.3.1 Spectral density

We begin with the calculation of the spectral density of the TLS, which is defined as

$$ {}_1A(\omega) = -\frac{1}{\pi}\mathrm{Im}\left[{}_1G_{\mathrm{e}}(\omega)\right]. \tag{3.36}$$

The spectral density can be interpreted as a measure for the distribution of the states. For a single particle without interaction, the spectral density assumes the form of a δ-function at the particle's energy. When the particle is subjected to interaction the spectral density is broadened due to the self-energy. The width can then be interpreted as the lifetime of the particle. In the present case, the spectral density of the TLS can be interpreted as a measure of the strength of the decay into the individual modes of the waveguide.

Since the broadening of the spectral density is introduced by the self-energy, we start by examining the according one given by Eq. (3.17),

$$\begin{aligned} {}_1\Sigma(\omega) =& U^2 \int \frac{\mathrm{d}k}{2\pi} \frac{1}{\omega + \Omega/2 - \epsilon(k) + i0} \\ =& U^2 \mathcal{P} \int \frac{\mathrm{d}k}{2\pi} \frac{1}{\omega + \Omega/2 - \epsilon(k)} - i\pi U^2 \int \frac{\mathrm{d}k}{2\pi} \sum_n \delta(k-k_n) \frac{1}{\partial\epsilon/\partial k}\bigg|_{k=k_n}. \end{aligned} \tag{3.37}$$

Here, $\mathcal{P}$ denotes the Cauchy principal value and the k_n are given by the roots of $\omega + \Omega/2 = \epsilon(k)$. If all these roots are real (this is the case when the energy lies in the band), the principal value vanishes. Furthermore, the second term can be identified with the density of states (DOS). Hence, we can write

$$ {}_1\Sigma(\omega) = -i\pi U^2 \nu(\omega) \tag{3.38}$$

with the DOS $\nu(\omega)$. As discussed in Sec. 2.3.2, we are mainly interested in two dispersion relations, a cosine one and a linear one

$$ \epsilon_{\cos}(k) = -2J\cos(k) \qquad\qquad \epsilon_{\mathrm{lin},\mu}(k) = \mu v k. \tag{3.39}$$

[4]Double excitation would be possible if the waveguide is coupled to a bosonic emitter. In this case the system is linear and the Green's function in the two-excitation sector would factorize.

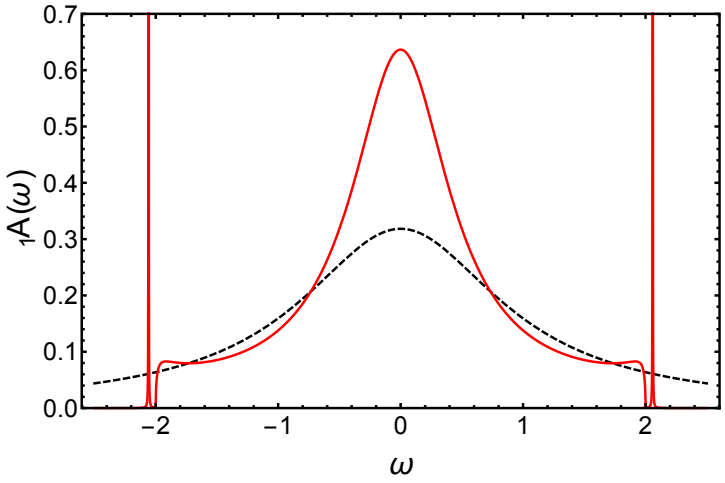

Figure 3.1: *Spectral density of the TLS with*[5] $\Omega = 0$, $U = 1$, $v = 1$ *and* $J = 1$ *for the linear (black, dashed) and cosine (red) dispersion relation. The spectral density of the cosine band clearly displays the band edges and features spectrally ultra-sharp bound states in the band gaps on either side of the band (when plotting the spectral density for the cosine band, we have introduced an artificial broadening* $\delta = 10^{-4}$ *in order to enhance the visibility of the bound states). By contrast, the spectral density for the linear dispersion relation corresponds to a simple Lorentzian.*

For these dispersion relations we find the self-energies

$$ {}_1\Sigma_{\cos}(\omega, \Omega) = \frac{U^2}{\omega + \Omega/2 + i\delta - 2J} \sqrt{\frac{\omega + \Omega/2 + i\delta - 2J}{\omega + \Omega/2 + i\delta + 2J}} \tag{3.40} $$

and

$$ {}_1\Sigma_{\text{lin}}(\omega) = -i\frac{U^2}{v}. \tag{3.41} $$

The absence of any band curvature in the case of a linear dispersion relation leads to a frequency-independent DOS and thus to a frequency-independent self-energy. Furthermore, the self-energy for the cosine dispersion is written in a slightly complicated way such that the square-root is evaluated at the correct side of the branch-cut.

We have plotted the spectral density for both cases in Fig. 3.1. In the case of a linear dispersion relation, we observe a Lorentzian centered around $\Omega/2$ with a width U^2/v. The spectral density assumes a more complicated form in the case of a cosine dispersion relation. In this case, we can see the bandwidth of the dispersion relation ($\omega \in [-2J, 2J]$) together with

[5] Note that since we have set $\hbar = 1$ basically all parameters apart from the momentum have the unit energy, e.g. $[\Omega]$ = Energy. We can thus set an arbitrary scale for the energy and present no units. Furthermore, the momentum has no unit because the calculations are carried out in the field limit, i.e. there is no scale which defines a length.

two ultra-sharp peaks in the band gap, which correspond to the atom-photon bound states [55, 72, 76, 77] introduced in Sec. 3.1.

3.3.2 Scattering matrix

In addition to the spectral density, the knowledge of the Green's functions enables us to calculate the scattering matrix via the Lehmann-Symanzik-Zimmermann (LSZ) reduction formula [85–87]. According to this formula, the scattering matrix (S-Matrix) is defined as

$$S_{k,p} = \delta_{k,p} + i2\pi\delta\left(\epsilon(k) - \epsilon(p)\right)\mathcal{T}_{k,p}, \tag{3.42}$$

where the T-Matrix $\mathcal{T}$ (not to be confused with the self-consistent T-matrix Eq. (3.27)) is given by

$$i\mathcal{T}_{k,p} = -i\Delta_N G_0^{-1}(k)G(k,p)G_0^{-1}(p)\Big|_{\text{os}}. \tag{3.43}$$

Here, $G(k,p)$ and $G_0(k)$ denote, respectively, the full and free (waveguide) Green's function and the subscript "os" indicates that the expression is taken on-shell, i.e.

$$\omega = \sum_i \epsilon(k_i) + \Omega/2 = \sum_f \epsilon(k_f) + \Omega/2, \tag{3.44}$$

where the sums are over the initial and final momenta, respectively. Furthermore, we have added the factor $\Delta_N = (2\pi)^{-N}$ (where N is the excitation number), which accounts for the fact that we use equal-time Green's functions and stems from missing Fourier transformations in the derivation of the LSZ formula[6].

With the help of Eq. (3.13) and (3.18), and dropping the free propagating part in the full Green's function, we find

$$iT_{k,p} = -i\frac{U^2}{2\pi}{}_1G_{\text{e}}(\omega)\Big|_{\text{os}}. \tag{3.45}$$

Additionally, rewriting the energy conserving δ-function in terms of momenta and the DOS

$$\delta\left(\epsilon(k) - \epsilon(p)\right) = \pi\nu\left(\delta_{k,p} + \delta_{k,-p}\right), \tag{3.46}$$

yields the S-Matrix

$$S_{k,p} = (1 + r_k)\delta_{k,p} + r_k\delta_{k,-p}, \tag{3.47}$$

[6] The original derivation of the LSZ formula is performed in time domain whereas we use it in frequency domain. Note how the Green's function in time-domain can be obtained in two different ways from the ones in frequency domain,

$$\int \frac{\mathrm{d}\omega}{2\pi}\frac{1}{\omega - \epsilon_1 - \epsilon_2 + i0}e^{-i\omega t} = i\int \mathrm{d}\tau \int \frac{\mathrm{d}\omega}{2\pi}\frac{1}{\omega - \epsilon_1 + i0}e^{-i\omega t}\int \frac{\mathrm{d}\tilde{\omega}}{2\pi}\frac{1}{\omega - \epsilon_2 + i0}e^{-i\tilde{\omega}\tau}\delta\left(t - \tau\right).$$

On the left we have a generic equal-time Green's function and on the right two independent ones together with a δ-function which matches the two times. The derivation of the LSZ formula involves independent Green's functions, which indicates the origin of the factors $(2\pi)^{-N}$ appearing in the LSZ formula for equal-time Green's functions.

where the reflection coefficient is given by

$$r_k = \frac{-i\pi\nu U^2}{\epsilon(k) - \Omega/2 + i\pi\nu U^2}. \tag{3.48}$$

With the help of Eq. (3.40) and (3.41) we find the reflection coefficients for the cosine and linear dispersion relations as

$$r_k^{\cos} = \frac{-iU^2}{2J|\sin(k)|} \frac{1}{-2J\cos(k) - \Omega + iU^2/2J|\sin(k)|} \tag{3.49}$$

and

$$r_k^{\mathrm{lin}} = \frac{-iU^2/v}{vk - \Omega + iU^2/v}. \tag{3.50}$$

In these formulas we have performed a shift $\omega \to \omega - \Omega/2$, such that our results agree with earlier calculations [50, 55, 74].

3.4 Properties of the Green's function in the two-excitation sector

After the discussion of the single-excitation sector, we now turn to the case of two excitations. The examination of the Green's functions in the two-excitation sector is not as straightforward as in the case of a single excitation due to the more complicated analytical structure (including a self-consistent T-Matrix equation), which originates from the nonlinear behavior of the system. We thus split the analysis of the Green's functions in two parts: The first part includes a numerical treatment of the self-consistent T-Matrix equation for a cosine dispersion relation, which allows us to compute the spectral density. In the second part we show that the Green's function can be calculated exactly for a linear dispersion relation and we derive again the spectral density and the scattering matrix in this case.

3.4.1 Cosine dispersion relation

In order to calculate the full TLS-Green's function, we have to determine the T-Matrix, which is defined by the self-consistent Eq. (3.27). We solve this equation by treating the waveguide as a discrete system, i.e. consisting of L sites with unit lattice spacing. In this case Eq. (3.27) transforms to

$$T(k_f, k_i; \omega) = U^2\, {}_2G_{\mathrm{w}}^0(k_f, k_i; \omega) + \frac{U^2}{L} \sum_k {}_2G_{\mathrm{w}}^0(k, k_i; \omega)\, {}_2G_{\mathrm{e,r}}(k; \omega)\, T(k_f, k; \omega). \tag{3.51}$$

The second term on the right hand side has the form of a matrix product (where k_i and k_f make up the rows and columns of the matrix). Therefore the above equation can be readily solved numerically by employing linear algebra and we are able to compute the full TLS-Green's function numerically for arbitrary dispersion relations.

We define the spectral density of the TLS in the two-excitation sector as

$${}_2A(k, \omega) = -\frac{1}{\pi} \mathrm{Im}\left[{}_2G_{\mathrm{e}}(k, k; \omega)\right]. \tag{3.52}$$

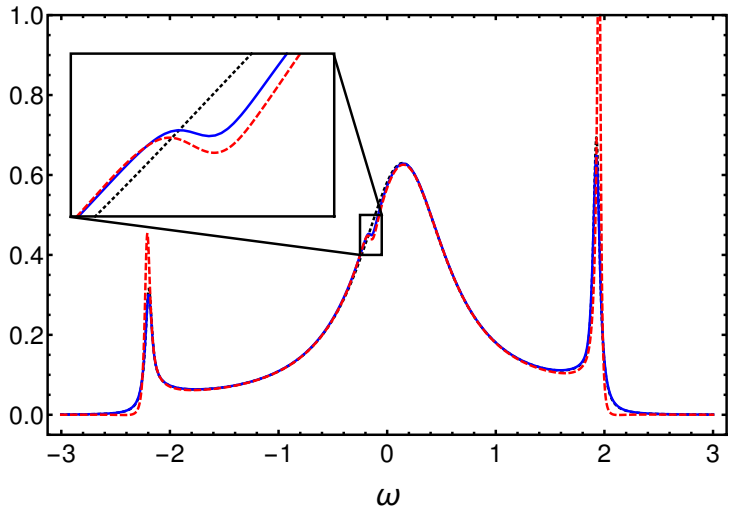

Figure 3.2: *Single and two-excitation spectral density* ${}_1A(\omega)$ *(black dotted) and* ${}_2A(\pi/2,\omega)$ *(obtained via the Green's function approach (solid blue) and DMRG (dashed red)) of the TLS with* $\Omega = 0.3$ *and* $U = 1$ *for a tight-binding waveguide with* $L = 600$ *discrete sites and cosine dispersion relation* $\epsilon(k) = -2t\cos(k)$ $(t = 1)$*. In* ${}_2A(\pi/2,\omega)$*, we clearly observe a Fano-resonance just below* $\omega = 0$ *(see text for details). This Fano-resonance is absent in the single-excitation spectral density of the TLS. When plotting the spectral densities, we have introduced an artificial broadening* $\delta = 0.04$ *in order to enhance the visibility of the Fano-resonance and to improve numerical convergence.*

We have plotted both ${}_1A(\omega)$ and ${}_2A(\pi/2,\omega)$ in Fig. 3.2 for the cosine dispersion relation. First of all, we notice that both functions show an overall similar behavior. The most notable difference between the two plots is a wiggle in the plot of ${}_2A(\pi/2,\omega)$ just below $\omega = 0$, which we attribute to a Fano resonance between the excited (renormalized) TLS and the additional photon in the waveguide. A Fano resonance appears when a broad continuum of states interacts with a single sharp mode. In our case the (smeared out) TLS plays the role of the continuum and the additional photon acts as a sharp resonance. Furthermore, we have introduced an artificial broadening $\delta = 0.04$ to enhance numerical convergence. Due to this relatively large broadening, the bound states are not as sharp as in Fig. 3.1 and the Fano resonance is smeared out. To support our calculations, we have also plotted the spectral density as obtained by using an expansion in Chebyshev polynomials within the framework of the Density-Matrix-Renormalization-Group (DMRG) technique as described in [88] (this calculation has been performed by P. Schmitteckert).

Finally, we would like to note that this Fano resonance appears also in the case of a linear dispersion relation (see next section). Thus we conjecture that the Fano resonance is a typical feature for an excited (renormalized) TLS interacting with individual photons in the waveguide and is visible in every sector with excitation number $N > 1$. In addition, we would like to stress

that although we have analyzed the case of a cosine dispersion relation here, the framework is able to compute the two-excitation Green's functions for arbitrary dispersion relations.

3.4.2 Linear dispersion relation

After having solved the self-consistent T-Matrix equation numerically, we try to calculate the full Green's function analytically in this section. A linear dispersion relation offers itself for this purpose since it is infinitely extended over the whole energy and momentum range and does not exhibit potentially problematic features like band edges. Indeed, the two-excitation self-energy is given by

$$ {}_2\Sigma_{\mathrm{lin}}(k;\omega) = -i\frac{U^2}{v}, \tag{3.53} $$

which is identical to the single-excitation self-energy ${}_1\Sigma_{\mathrm{lin}}(\omega)$. Moreover, ${}_2\Sigma_{\mathrm{lin}}(k;\omega)$ is not depending on the momentum of the additional photon in the waveguide, which indicates that the TLS-Green's function can indeed be calculated exactly in this case.

In contrast to the numerical treatment above, we do not aim at solving the self-consistent T-Matrix equation but rather calculate the perturbation series given by Eq. (3.22). This perturbation series can be cast in the form

$$ {}_2G_{\mathrm{e}}(k_f,k_i;\omega) = \sum_i {}_2G_{\mathrm{e}}^{(i)}(k_f,k_i;\omega), \tag{3.54} $$

where the first two terms are trivial, as no integration over internal momenta is required. The third term, however, is given by

$$ {}_2G_{\mathrm{e}}^{(3)}(k_f,k_i;\omega) = U^4 \sum_\mu \int \frac{\mathrm{d}k}{2\pi}\, {}_2G_{\mathrm{e,r}}(k_i;\omega)\, {}_2G_{\mathrm{w}}^{0}(k_i,k;\omega)\, {}_2G_{\mathrm{e,r}}(k;\omega)\, {}_2G_{\mathrm{w}}^{0}(k,k_f;\omega)\, {}_2G_{\mathrm{e,r}}(k_f;\omega), \tag{3.55} $$

where the integral extends only over the three internal Green's functions and we sum over the chirality of the internal photon[7]. Since the self-energy ${}_2\Sigma_{\mathrm{lin}}(k;\omega)$ is independent of the integration variable k, all Green's functions in the integrand have simple poles which are shifted into the same half-plane[8]. Hence, the integral vanishes. This statement holds true for all diagrams of order higher or equal to three, which means that the full TLS-Green's function for a linear dispersion relation is given by

$$ {}_2G_{\mathrm{e}}(k_f,k_i;\omega) = {}_2G_{\mathrm{e,r}}(k_i;\omega)\, 2\pi\delta_{k_i,k_f} + U^2\, {}_2G_{\mathrm{e,r}}(k_i;\omega)\, {}_2G_{\mathrm{w}}^{0}(k_f,k_i;\omega)\, {}_2G_{\mathrm{e,r}}(k_f;\omega). \tag{3.56} $$

Besides from the mathematical argument presented above, we can also understand the breakdown of the perturbation series from a physical point of view. In the Feynman diagram representation, the first vanishing diagram is given by

$$ {}_2G_{\mathrm{e}}^{(3)}(k_f,k_i;\omega) = $$

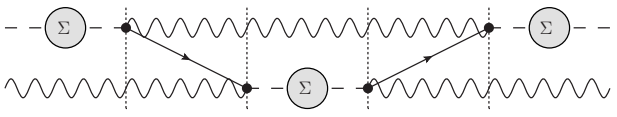

, (3.57)

[7] The chirality index is suppressed at the Green's functions.
[8] The actual half-plane depends on the chirality of the photon.

where in Eq. (3.55) we integrate over the momentum of the upper, intermediate photon. It is useful in this case to consider the physics behind the diagram in space-time domain. During the time when the intermediate photon exists the other, initial photon is absorbed by the TLS, which emits another photon at a later time. This entire process occupies a certain time $\tau > 0$ during which the intermediate photon travels away from the TLS (due to the nonvanishing group velocity v). Hence, the intermediate photon cannot be reabsorbed by the TLS which renders the diagram to zero. We note that this behavior could be overcome by the appearance of a slow-light regime in the dispersion relation, such that the photon stays in the vicinity of the TLS and can be reabsorbed.

Spectral density

We have calculated the two-excitation spectral density according to Eq. (3.52) and plotted it together with the single-excitation spectral density in Fig. 3.3. In analogy to the numerical calculations for the cosine dispersion relation, we find again a Fano resonance located at

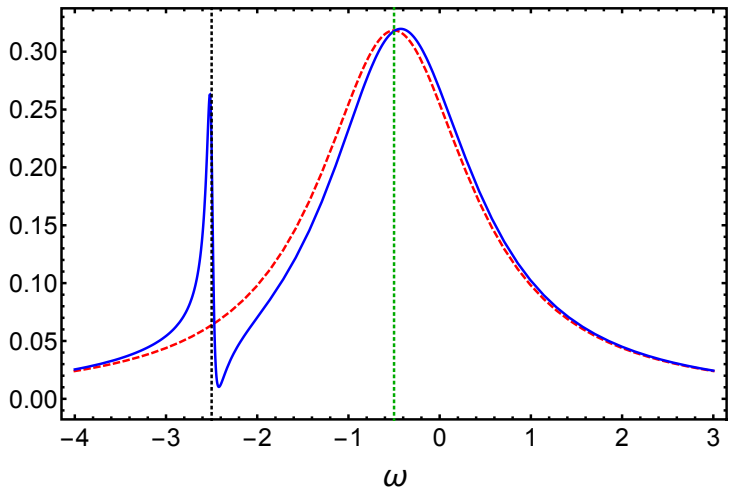

Figure 3.3: *Single- and two-excitation spectral densities* ${}_2A(-1,\omega)$ *(solid blue) and* ${}_1A(\omega)$ *(dashed red) of the TLS with* $\Omega = 1$ *and* $U = 1$ *for a waveguide with linear dispersion relation* $\epsilon(k) = \mu v k$ *and* $v = 1$*. We have shifted the single-excitation spectral density* ${}_1A(\omega)$ *by* $\omega \to \omega - vk$*, so that the maxima of both plots overlap. The green dotted line is at* $vk + \Omega/2$ *and indicates the maximum of* ${}_1A(\omega)$*. In* ${}_2A(-1,\omega)$*, we clearly observe a Fano-resonance at* $\omega_F = 2vk - \Omega/2$ *(black-dotted line) which is more pronounced than for the case of the cosine dispersion relation in Fig. 3.2. As in the case of the cosine dispersion relation, this Fano-resonance is absent in the single-excitation spectral density of the TLS. When plotting the spectral densities, we have introduced the same artificial broadening* $\delta = 0.04$ *as in the case of the cosine dispersion relation in order to enhance the visibility of the Fano-resonance and make the graph comparable to that in Fig. 3.2.*

$\omega_F = 2vk - \Omega/2$, which, however, is much more pronounced than in the latter case. Comparing both dispersion relations, the Fano resonance appears in two different ways: In the case of the cosine dispersion relation the Fano resonance emerges as a result of the self-consistent treatment of the T-Matrix, whereas for the linear dispersion relation it can be traced back to the second term in the perturbation series ${}_2G_\mathrm{e}^{(2)}(k_f, k_i; \omega)$. To be more exact, the Fano resonance stems from the internal free waveguide Green's function ${}_2G_\mathrm{w}^0(k_i, k_f; \omega)$, which is of the form $(\omega - \omega_F + i\delta)^{-1}$. Hence, the Fano resonance is the result of a first order pole, regularized by a finite imaginary factor $i\delta$. For sufficiently small δ, the spectral density can thus assume negative values. However, one has to take into account that we are not considering the spectral density of the full system, but only of a part of it (namely that of the TLS). Hence, a negative spectral density is acceptable and can be considered as some sort of gain (where the energy is taken from the waveguide), indicating effects like photon bunching [51, 52, 79]. Moreover, we would like to point out that the Fano resonance is less pronounced in Fig. 3.2, although all energies are in the linear regime of the cosine band. Therefore the Green's functions for the cosine and linear dispersion relation should be comparable. We attribute this regularization to the self-consistent treatment of the Green's function for a cosine dispersion relation, which is not possible for the linear dispersion relation.

The deeper reason behind the breakdown of the perturbation series is the separation of the photons on the Hamiltonian level in two kinds of photons (left- and rightmoving ones). This changed the symmetry of the Hamiltonian and eventually led to the special analytic structure of the Green's functions and thus to the breakdown of the perturbation series.

Scattering matrix

Due to the knowledge of the exact Green's function, we are also able to construct the scattering matrix in the two excitation sector for a linear dispersion relation. Generalizing Eq. (3.42) to two excitations yields

$$S_{k_i p_i, k_f p_f} = \left(\delta_{k_i,k_f}\delta_{p_i,p_f} + \delta_{p_i,k_f}\delta_{k_i,p_f}\right) + i2\pi\delta(E)\,\mathcal{T}_{k_i p_i, k_f p_f}, \tag{3.58}$$

where $\delta(E) = \delta(\epsilon(k_i) + \epsilon(p_i) - \epsilon(k_f) - \epsilon(p_f))$ guarantees energy conservation. The T-Matrix is furthermore defined as

$$i\mathcal{T}_{k_i p_i, k_f p_f} = -i\Delta_N G_0^{-1}(k_i, p_i)\, G(k_i, p_i; k_f, p_f)\, G_0^{-1}(k_f, p_f)\Big|_\mathrm{os}. \tag{3.59}$$

As in the single-excitation sector, $G_0(k_i, p_i)$ and $G(k_i, p_i; k_f, p_f)$ are the free and full waveguide Green's functions, respectively, and $\Delta_N = (2\pi)^{-N}$ (N is the excitation number). With the help of Eq. (3.28) we find

$$i\mathcal{T}_{k_i p_i, k_f p_f} = -i\frac{U^2}{(2\pi)^2}\,{}_2G_\mathrm{e}^\mathrm{sym}(k_i, p_i, k_f, p_f; \omega)\Big|_\mathrm{os}, \tag{3.60}$$

where ${}_2G_\mathrm{e}^\mathrm{sym}(k_i, p_i, k_f, p_f; \omega)$ is defined in Eq. (3.29).

In order to keep this section compact, we have relegated the calculation of the two-excitation S-Matrix to Appendix B and only show the results here. Shifting the energy as $\omega \to \omega - \Omega/2$, we find for the different chirality configurations

- $k_i^R p_i^R \to k_f^R p_f^R$

$$S^{RR,RR}_{k_i p_i, k_f p_f} = t_{k_i} t_{p_i} \left(\delta_{k_i,k_f} \delta_{p_i,p_f} + \delta_{k_i,p_f} \delta_{p_i,k_f} \right) + S^{2,\mathrm{P.V.}}_{k_i p_i, k_f p_f}, \tag{3.61}$$

- $k_i^R p_i^R \to k_f^R p_f^L$

$$S^{RR,RL}_{k_i p_i, k_f p_f} = t_{k_i} r_{p_i} \delta_{k_i,k_f} \delta_{p_i,-p_f} + r_{k_i} t_{p_i} \delta_{k_i,-p_f} \delta_{p_i,k_f} + S^{2,\mathrm{P.V.}}_{k_i p_i, k_f p_f}, \tag{3.62}$$

- $k_i^R p_i^R \to k_f^L p_f^L$

$$S^{RR,LL}_{k_i p_i, k_f p_f} = r_{k_i} r_{p_i} \left(\delta_{k_i,-k_f} \delta_{p_i,-p_f} + \delta_{k_i,-p_f} \delta_{p_i,-k_f} \right) + S^{2,\mathrm{P.V.}}_{k_i p_i, k_f p_f}. \tag{3.63}$$

Here, the superscript of the momenta indicates the corresponding chiralities, r_k is the single-excitation reflection amplitude given by Eq. (3.50), $t_k = 1 + r_k$ is the single-excitation transmission amplitude. $S^{2,\mathrm{P.V.}}_{k_i p_i, k_f p_f}$ is given by

$$\begin{aligned} S^{2,\mathrm{P.V.}}_{k_i p_i, k_f p_f} = \frac{iU^4}{\pi v} \delta_{k_i + p_i, k_f + p_f} & \frac{\left(k_i + p_i - 2\Omega + iU^2/v \right)}{(vp_i - \Omega + iU^2/v)(vk_i - \Omega + iU^2/v)} \\ & \times \frac{1}{(vp_f - \Omega + iU^2/v)(vk_f - \Omega + iU^2/v)}. \end{aligned} \tag{3.64}$$

This result is in agreement with earlier works, where the scattering matrix has been obtained by means of Bethe Ansatz [52], Input-Output formalism [53] and LSZ-techniques [55].

The most interesting part of the S-Matrix is the term $S^{2,\mathrm{P.V.}}_{k_i p_i, k_f p_f}$, which encapsulates the nonlinear behavior of the system[9] and comprises the effect of photon bunching [52, 79, 89]. In the first place, this term emerges by decomposing ${}_2G^0_{\mathrm{w}}(k, p; \omega)$ in ${}_2G^{(2)}_{\mathrm{e}}(k, p; \omega)$ as

$${}_2G^0_{\mathrm{w}}(k, p; \omega) = \frac{1}{\omega - vk - vp + i0} = \mathcal{P} \frac{1}{\omega - vk - vp} - i\pi\delta\left(\omega - vk - vp\right). \tag{3.65}$$

The two terms can be interpreted as follows: The δ-function sets the particles on-shell and can thus be associated with long-time, real processes. In fact, this term contributes to the single-excitation transmission and reflection amplitudes. The term containing the Cauchy principal value, however, can redistribute the momenta and eventually leads to the term $S^{2,\mathrm{P.V.}}_{k_i p_i, k_f p_f}$ in the S-Matrix. Since we have split off the long-time behavior we conclude that this term stems from short-time processes on the timescale of the Heisenberg uncertainty principle, i.e. it encapsulates *virtual processes*.

[9] the rest are just single-excitation effects

3.5 Conclusion

In this chapter, we have shown one of the main results of this thesis: We have developed a new formalism for waveguide QED, where we have adopted Green's functions in the single- and two-excitation sector that have been calculated with the help of the coherent-state path integral. These calculations provide us with closed-form solutions in both sectors for arbitrary dispersion relations, including a self-consistent T-Matrix equation in the two-excitation sector. Furthermore, representing the individual terms in the perturbation series as Feynman diagrams provides us with insight into the underlying physical processes.

We have used the Green's functions to extract the spectral density and the scattering matrix. In the single-excitation sector, these quantities serve a) as a confirmation of our framework by comparing the results with earlier works and b) as reference solutions to compare the two-excitation sector to. In the two-excitation sector we have split up the examination in two parts. In the first part we have solved the self-consistent T-Matrix equation numerically for a cosine dispersion relation (and backed it up with DMRG-techniques) and found a Fano resonance in the spectral density between the excited (renormalized) TLS and the additional photon in the waveguide. In the second part we have investigated a linear dispersion relation. In this case the perturbation series breaks down after two terms, thus we find an analytical expression for the exact Green's function. The spectral density exhibits again a Fano resonance. Furthermore, we were able to calculate the scattering matrix, which is accordance with earlier works.

As we will see throughout this thesis, Green's functions are a versatile tool and can be used to calculate the dynamics of photonic pulses in Chap. 5 or the influence of (fabricational) disorder in the waveguide on the TLS decay dynamics in Chap. 6. Other interesting applications would be, e.g., to include the effect of dissipation or adding a second TLS to study excitation transfer [90].

4 EFFECTS OF A NONLINEAR DISPERSION RELATION IN THE TWO-EXCITATION WAVEGUIDE QED

Here, we discuss the effects of a nonlinear dispersion relation in waveguide QED in the two-excitation sector, where we focus on the terms in the perturbation series of the Green's function which vanish for a linear dispersion relation. Motivated by a numerical study with a cosine dispersion relation we investigate two different regimes. Far away from band edges we define a quasi-linear regime and examine the effects of a small band curvature with perturbative methods. Here we find that additional physical processes are strongly suppressed and the dominant effects are renormalizations. In the vicinity of the band edge, however, the formerly vanishing terms become dominant and we find that they are responsible for the effect of interaction-induced radiation trapping.

4.1 Introduction

In the previous chapter we have calculated the Green's function in waveguide QED in the two-excitation sector for an arbitrary dispersion relation. The Green's function is defined in terms of a self-consistent T-Matrix equation, which we were not able to solve in the general case. However, we found that that the Green's function can be determined exactly in the case of a linear dispersion relation because in the perturbation series all terms higher than second order vanish. We thus investigate here the effect of a nonlinear dispersion relation by specifically looking at the nonvanishing terms in the perturbation series. Motivated by a numerical calculation of the full Green's function we consider two different regimes: For energies far away from a band edge and a small band curvature we define a quasi-linear regime, where we calculate perturbative corrections to the scattering matrix of the linear dispersion relation. On the other hand, for energies close to the band edge we analyze the first nonvanishing term on a phenomenological level and determine the dominant physical effect induced by this term.

4.2 The Green's function

We start by investigating the TLS-Green's function in the two-excitation sector again. From Eq. (3.22) we know that the Green's function can be written in terms of a perturbation series

$$\begin{aligned} {}_2G_{\mathrm{e}}(k_f,k_i;\omega) &= \sum_{i=1}^{\infty} {}_2G_{\mathrm{e}}^{(i)}(k_f,k_i;\omega) \\ &= \left[\sum_{i=1}^{2} {}_2G_{\mathrm{e}}^{(i)}(k_f,k_i;\omega)\right] + \left[\sum_{i=3}^{\infty} {}_2G_{\mathrm{e}}^{(i)}(k_f,k_i;\omega)\right] \\ &= {}_2G_{\mathrm{e}}^{\mathrm{lin}}(k_f,k_i;\omega) + {}_2G_{\mathrm{e}}^{\mathrm{T}}(k_f,k_i;\omega). \end{aligned} \tag{4.1}$$

This separation can also be made in the Feynman diagram representation,

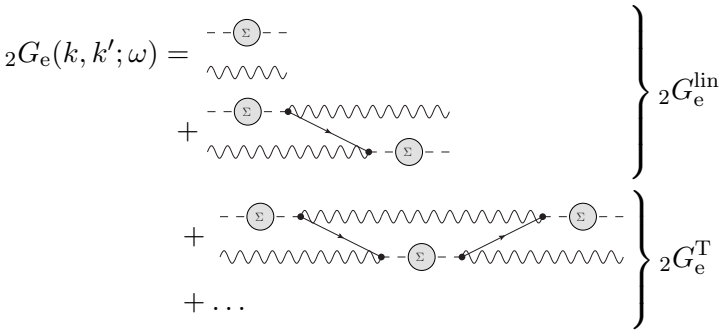

Here, ${}_2G_{\mathrm{e}}^{\mathrm{lin}}(k_f,k_i;\omega)$ encapsulates all the trivial terms (not containing internal integrations) which make up the Green's function in the case of a linear dispersion relation and ${}_2G_{\mathrm{e}}^{\mathrm{T}}(k_f,k_i;\omega)$ contains all the other terms.

We recall that the special property of the diagrams summed in ${}_2G_{\mathrm{e}}^{\mathrm{T}}(k_f,k_i;\omega)$ is the appearance of internal integrations. These integrations correspond to the upper photon in the third diagram, which is emitted and reabsorbed by the TLS. For a linear dispersion relation these diagrams vanish since the photon moves away from the TLS and cannot be reabsorbed. This could possibly be overcome by the appearance of a slow-light regime, such that the photon stays in the vicinity of the TLS. Alternatively, one could argue that the photons are massless in the case of a linear dispersion relation. Following this argument, a finite mass (induced by band curvature) would lead to inertia and the photon has a higher probability to be reabsorbed.

4.2.1 Qualitative Analysis of ${}_2G_{\mathrm{e}}^{\mathrm{T}}(k_f,k_i;\omega)$

We start our analysis by examining the qualitative behavior of the nontrivial terms. Note that throughout this chapter we have shifted the energy $\omega \to \omega - \Omega/2$. ${}_2G_{\mathrm{e}}^{\mathrm{T}}(k_f,k_i;\omega)$ can also be defined in terms of the self-consistent T-Matrix as

$${}_2G_{\mathrm{e}}^{\mathrm{T}}(k_f,k_i;\omega) = U^2\, {}_2G_{\mathrm{e,r}}(k_i;\omega)\, I_{\mathrm{T}}(k_i,k_f;\omega)\, {}_2G_{\mathrm{e,r}}(k_f;\omega), \tag{4.2}$$

where the internal integrations are included in

$$I_{\mathrm{T}}(k_i,k_f;\omega) = \int \frac{dk}{2\pi}\, {}_2G_{\mathrm{w}}^{0}(k_i,k;\omega)\, {}_2G_{\mathrm{e,r}}(k;\omega)\, T(k,k_f;\omega) \tag{4.3}$$

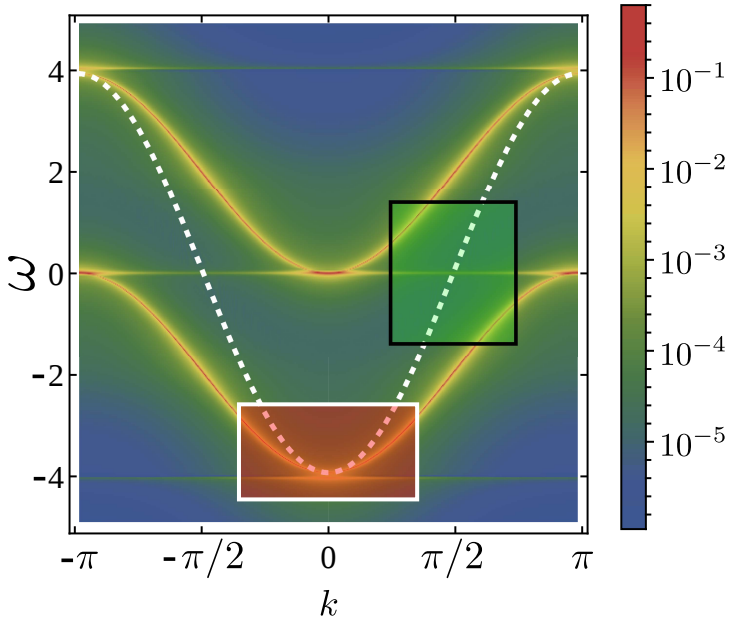

Figure 4.1: *Plot of* $|I_{\mathrm{T}}(k,k;\omega)|$*, calculated numerically on a waveguide with* $L = 4999$ *sites, where the intersite hopping constant* $J = 1$*,* $U = 1$*,* $\Omega = 0$*, and artificial broadening* $\delta = 0.005$*. The white dashed line indicates the free waveguide solution,* ${}_2G^0_w(k,k)^{-1} = 0$*, the green box with black borders shows the quasi-linear regime of the cosine band and the red box with white borders the regime of the band-edge.*

and $T(k_i,k_f;\omega)$ is defined in Eq. (3.27).

As discussed in the previous chapter ${}_2G^{\mathrm{T}}_{\mathrm{e}}(k_f,k_i;\omega) = 0$ for a linear dispersion relation since $I_{\mathrm{T}}(k_i,k_f;\omega)$ vanishes. For a general dispersion relation which could exhibit band curvature, slow-light regimes and a photonic band edge, however, this is not the case. We have plotted $I_{\mathrm{T}}(k,k;\omega)$ for a cosine dispersion relation in Fig. 4.1, where the T-Matrix was evaluated numerically by discretizing the waveguide into $L = 4999$ sites. Indeed, we find that $I_{\mathrm{T}}(k,k;\omega)$ can exhibit values up to order unity for special combinations of k and ω. The most prominent features in the plot are the two cosine-shaped curves, which are roughly separated by the bandwidth $4J$. These features are also visible, e.g., in the spectral density of the TLS[1] and can be attributed to the atom-photon bound states just outside of the band [55, 72, 73, 76]. In addition to the cosine-shaped curves, there are sharp lines at $\omega \simeq \{-4, 0, 4\}$ (the exact position depends on Ω). These lines are strongest near the atom-photon bound states, which suggests that there is some connection between the two features. Note that all these contributions stem from the band edge and that $I_{\mathrm{T}}(k_i,k_f;\omega)$ gives very small contributions apart from the above-mentioned features. This is in accordance with the result for the linear dispersion relation and

[1] See Fig. 3.1 and 3.2. These plots have a fixed momentum and the connection can be made by setting e.g. $k = \pi/2$ in Fig. 4.1.

furthermore indicates that the major contribution from ${}_2G_{\mathrm{e}}^{\mathrm{T}}(k_f, k_i; \omega)$ stems from band edge effects.

On a more qualitative level, $I_{\mathrm{T}}(k_i, k_f; \omega)$ can be also interpreted as a transition amplitude from photon momentum k_i to k_f in ${}_2G_{\mathrm{e}}^{\mathrm{T}}(k_f, k_i; \omega)$ (cf. Eq. (4.2)). In

$$\begin{aligned} {}_2G_{\mathrm{e}}^{\mathrm{lin}}(k_f, k_i; \omega) &= {}_2G_{\mathrm{e}}^{(1)}(k_f, k_i; \omega) + {}_2G_{\mathrm{e}}^{(2)}(k_f, k_i; \omega) \\ &= {}_2G_{\mathrm{e,r}}(k_i; \omega)\, 2\pi\delta_{k_i,k_f} + U^2\, {}_2G_{\mathrm{e,r}}(k_i; \omega)\, {}_2G_{\mathrm{w}}^{0}(k_f, k_i; \omega)\, {}_2G_{\mathrm{e,r}}(k_f; \omega), \end{aligned} \tag{4.4}$$

this task is taken over by the free waveguide Green's function ${}_2G_{w}^{0}(k_f, k_i; \omega)$ in the term ${}_2G_{\mathrm{e}}^{(2)}(k_f, k_i; \omega)$. We have plotted the solution of ${}_2G_{w}^{0}(k, k)^{-1} = 0$ in Fig. 4.1 as white, dashed curve. Comparing this solution with the features of $I_{\mathrm{T}}(k_i, k_f; \omega)$ we see that both solutions behave qualitatively different. From this we can infer that $I_{\mathrm{T}}(k_i, k_f; \omega)$ couples the momenta in a different way than ${}_2G_{w}^{0}(k_f, k_i; \omega)$ and hence ${}_2G_{\mathrm{e}}^{\mathrm{T}}(k_f, k_i; \omega)$ describes different physics than ${}_2G_{\mathrm{e}}^{\mathrm{lin}}(k_f, k_i; \omega)$.

4.2.2 Obstacles for an analytic solution

Since the dominant contributions in ${}_2G_{\mathrm{e}}^{\mathrm{T}}(k_f, k_i; \omega)$ stem from the band edge, we try to calculate the first nontrivial term in the perturbation series for a quadratic dispersion relation, $\epsilon(k) = tk^2$ ($t > 0$). In this case, the two-excitation self-energy is given by

$${}_2\Sigma_{\mathrm{qu}}(k; \omega) = -i\frac{\pi U^2}{\sqrt{t(\omega - tk^2 + i\delta)}}. \tag{4.5}$$

This self-energy renders the internal momentum integration in ${}_2G_{\mathrm{e}}^{(3)}(k_f, k_i; \omega)$ very difficult. First of all, we notice that the the quadratic dispersion relation induces poles on either half-plane, hence the integral cannot vanish immediately. Moreover, the self-energy induces two branch-cuts, one on either side of the real axis. These branch-cuts are major obstacles in the computation of the internal integral and we have not succeeded in finding a general solution for the integral.

We thus focus on two different regimes in this chapter: The first part considers in a quasi-linear regime where we perform a perturbative calculation. In this regime, the energies are far away from the band edge, but the dispersion relation still features a nonvanishing band curvature. In the second part we analyze the phenomenological behavior of ${}_2G_{\mathrm{e}}^{\mathrm{T}}(k_f, k_i; \omega)$ in the vicinity of the band edge, where the dispersion relation is again quadratic. The energy and momentum range considered in these limits are shown by the green box with black borders and the red box with white borders in Fig. 4.1, respectively.

4.3 Quasi-Linear Regime

We start by investigating the effect of a small band curvature on ${}_2G_{\mathrm{e}}^{\mathrm{T}}(k_f, k_i; \omega)$. The idea behind this calculation is that a finite band curvature induces a mass to the photons. As already noted, the mass leads to inertia and therefore the photons should have a higher probability to return to the TLS. We therefore define a quasi-linear regime and calculate perturbatively the corrections to the scattering matrix induced by the small nonlinearity in the dispersion relation.

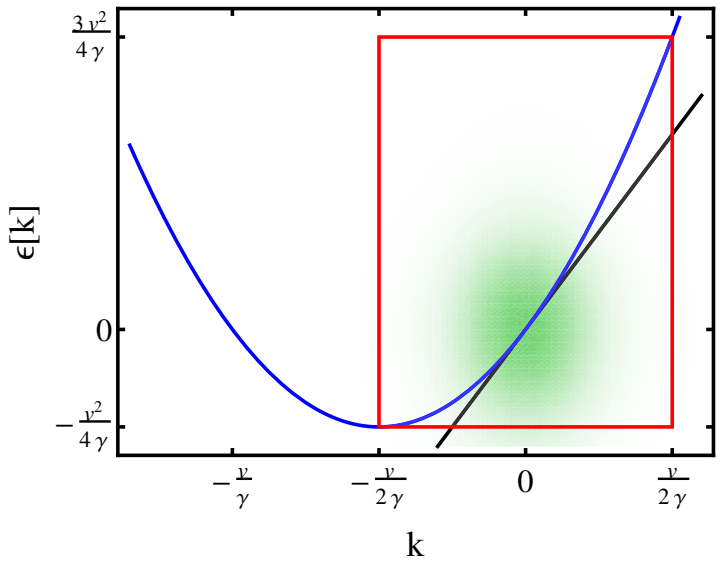

Figure 4.2: *Dispersion relation with $\gamma/v = 0$ (black) and $\gamma/v = 0.05$(blue). The dispersion relation with curvature exhibits a band edge and a second solution with $\epsilon(k) = 0$, which are both not physical. The red rectangle indicates the limits given by Eqs.* (4.9) *and* (4.10) *and the green shaded region shows roughly the actual quasi-linear region.*

4.3.1 Definition of the quasi-linear regime

Assuming that the photons are injected into the waveguide with a given momentum k_0, we can expand the dispersion relation around this momentum as

$$\epsilon(k) = \epsilon(k_0) + v(k - k_0) + \gamma(k - k_0)^2 + \ldots, \tag{4.6}$$

where $v = \epsilon'(k_0)$ and $\gamma = \epsilon''(k_0)/2$. We take the nonlinearity in Eq. (4.6) in the limit $|\gamma/v| \ll 1$ into account and set $v > 0$ and $\gamma > 0$ to simplify the calculations. Furthermore, we measure all momenta and energies with respect to k_0 and $\epsilon(k_0)$. The dispersion relation used in the remainder of this paper is thus given by

$$\epsilon(k) = vk + \gamma k^2. \tag{4.7}$$

It is clear that such an expansion is only valid for a certain range of momenta, i.e. as long as the dispersion relation can be considered as quasi-linear. This can be quantified by looking at the normalized derivative of the dispersion relation,

$$\frac{\epsilon'(k)}{\epsilon'(0)} = 1 + \frac{2\gamma k}{v}. \tag{4.8}$$

The correction should be small, which leads to

$$\left|\frac{2\gamma k}{v}\right| \ll 1 \qquad \Rightarrow \qquad |k| \ll \left|\frac{v}{2\gamma}\right|. \tag{4.9}$$

Inserting these momenta into the dispersion relation yields the energies which lie in the quasi-linear regime of the dispersion relation,

$$-\frac{v^2}{4\gamma} = \epsilon\left(-\frac{v}{2\gamma}\right) \ll E \ll \epsilon\left(\frac{v}{2\gamma}\right) = \frac{3v^2}{4\gamma}. \tag{4.10}$$

The equations above define the limits in which Eq. (4.7) is a good approximation of the underlying real dispersion relation. We note that Eq. (4.7) exhibits a band edge at $k = -v/2\gamma$ and a second quasi-linear regime at $k \sim -v\gamma$. These properties lie outside of the region defined by Eq. (4.9) and are in general not contained in the underlying real dispersion relation. Consequently, these features should be neglected when performing a calculation. This can be done by choosing all energies and momenta such that Eq. (4.9) and (4.10) are fulfilled.

So far, the dispersion relation describes only right moving photons ($v > 0$). In order to complete the discussion of the band structure we have to include left-moving photons, which generalizes the dispersion relation

$$\epsilon_\mu(k) = \mu v k + \gamma k^2. \tag{4.11}$$

Here, $\mu = R/L = +/-$ is again the quantum number chirality, in analogy to the purely linear case evaluated in Sec. 2.3.2. Note that this discussion is included for the sake of completeness; the calculation in the next section is carried out for right-moving photons since chirality plays an insignificant role[2].

4.3.2 Scattering matrix

We have calculated $I_{\mathrm{T}}(k_i, k_f; \omega)$ in Appendix C for the dispersion relation given by Eq. (4.7). In the case $\gamma/v \ll 1$ and assuming that all energies appearing in the integrand lie in the quasi-linear regime given by Eq. (4.10) we find that

$$I_{\mathrm{T}}(k_i, k_f; \omega) = 0 + \mathcal{O}\left(\frac{\gamma}{v}\right)^2, \tag{4.12}$$

whereas ${}_2G_{\mathrm{e}}^{\mathrm{lin}}(k_i, k_f; \omega)$ gives corrections to first order in γ/v. Thus, the Green's function is given in leading order by

$${}_2G_{\mathrm{e}}(k_i, k_f; \omega) = {}_2G_{\mathrm{e}}^{\mathrm{lin}}(k_i, k_f; \omega), \tag{4.13}$$

the differences to the purely linear case are only the nonlinear dispersion relation entering the basic Green's functions and the renormalized self-energy of the TLS-Green's function.

[2] The chirality plays only an insignificant role in the evaluation of $I_{\mathrm{T}}(k_i, k_f; \omega)$, but is important in the derivation of the quasi-linear regime. The quasi-linear regime is only well-defined if the right- and leftmoving particles can be separated, otherwise one would necessarily need a band edge.

The knowledge of the Green's function enables us to calculate the two-photon S-Matrix with the help of the LSZ reduction formula. Since the structure of the Green's function is very similar to the one with a purely linear dispersion relation, we follow closely the calculation in Appendix B and find for the case of two transmitted photons

$$S_{k_i p_i, k_f p_f} = t_{k_i} t_{p_i} \left(\delta_{k_i,k_f} \delta_{p_i,p_f} + \delta_{k_i,p_f} \delta_{p_i,k_f} \right) + S^{PV}_{k_i p_i, k_f p_f}. \tag{4.14}$$

Here,

$$t_k = 1 + r_k = 1 + \frac{-iU^2/(v + 2\gamma k)}{\epsilon(k) - \Omega + iU^2/(v + 2\gamma k)} \tag{4.15}$$

is the transmission amplitude, r_k the reflection amplitude and

$$S^{PV}_{k_i p_i, k_f p_f} = \frac{iU^4}{\pi} \delta(E) \tilde{r}_{ki} \tilde{r}_{pi} \tilde{r}_{kf} \tilde{r}_{pf} \left(c_4 \left(\epsilon(k_i) + \epsilon(p_i) \right) - 2c_2 \Omega + i2c_2 \frac{U^2}{v} \right), \tag{4.16}$$

where $\delta(E)$ is an energy-conserving δ-function,

$$\tilde{r}_k = \frac{1}{\epsilon(k) - \Omega + iU^2/(v + 2\gamma k)} \tag{4.17}$$

and

$$c_n = 1 - in \frac{\gamma}{v} \frac{U^2}{v^2}. \tag{4.18}$$

The structure of the scattering matrix is the same as in the purely linear case (cf. Sec. 3.4). The first term containing the transmission amplitudes describes the scattering on the single photon level whereas the second term stems from the nonlinear behavior of the TLS in the presence of two or more photons and induces photon bunching [51, 79, 84]. The nonlinear dispersion relation leads to renormalization effects, which are discussed in the next section.

4.3.3 Discussion

We now turn to the discussion of the results obtained above. Due to the suppression of additional physical processes and ${}_2G_\mathrm{e}(k_i, k_f; \omega) = {}_2G^\mathrm{lin}_\mathrm{e}(k_i, k_f; \omega)$, the dominant effect of the nonlinearity in the S-matrix are renormalizations. This can be quantified by an analysis of the poles, which represent the resonances [91]. The reflection amplitude r_k exhibits several poles, but only one lies in the quasi-linear regime, at

$$k_0 = \frac{\Omega}{v} \left(1 - \frac{\gamma}{v} \frac{\Omega}{v} \right) + \frac{\gamma}{v} \frac{3U^4}{v^4} - i \frac{U^2}{v^2} \left(1 - \frac{\gamma}{v} \frac{4\Omega}{v} \right) \tag{4.19}$$

to first order in γ/v. The real part of the pole represents the resonance momentum and consists of two terms: The first term $\frac{\Omega}{v} \left(1 - \frac{\gamma}{v} \frac{\Omega}{v} \right)$ is the solution of the resonance condition $\epsilon(k) = \Omega$ in first order γ/v; the second term stems from the real part of the self-energy and shifts the resonance away from the band edge. The imaginary part of the pole describes the width of the resonance. Here, the renormalization of the width U^2/v^2 in the case of a linear

dispersion relation is connected with the TLS resonance energy Ω and is sensitive to its sign. This connection can be explained by the value of Ω and the according group velocity of the waveguide at this energy. Rewriting the width as $U^2/\tilde{v}^2$, with the group velocity

$$\tilde{v} = \left.\frac{\partial\epsilon(k)}{\partial k}\right|_{k=\epsilon^{-1}(\Omega)} \tag{4.20}$$

taken at Ω gives the same result as in the S-matrix pole. Note that the structure of the renormalization suggests that the width could become zero or negative. This is an artifact from the expansion in γ/v and cannot be achieved as long as Ω fulfills Eq. (4.10).

Since the single-particle reflection amplitude r_k exhibits only one pole in the quasi-linear regime, the decay of the TLS is still purely exponential, as in the case of a linear dispersion relation. This means that the calculation carried out above can be considered as a Markovian approximation. Non-Markovian effects are expected to appear when the energies are closer to the band edge. As a last remark on the S-matrix we note that the poles of $S^{PV}_{k_i p_i, k_f p_f}$ are renormalized in the same way as the ones in r_k, which means that the photon bunching effect [51, 52, 79] is renormalized accordingly.

Finally, we can compare these results with the numerical calculation of the cosine dispersion relation (cf. Fig. 4.1). The calculations here have focused on the regime where all energies are far away from band edges and the band curvature is small. This can be quantified for the cosine band by the equation $|\epsilon''_{\cos}(k)/\epsilon'_{\cos}(k)| \ll 1$, and an equation similar to Eq. (4.10) for the energies. These equations give $\frac{\pi}{4} \ll k \ll \frac{3\pi}{4}$ and $-\sqrt{2} \ll \omega \ll \sqrt{2}$, which is plotted in Fig. 4.1 as the green box with black borders, which also indicates the quasi-linear regime (we have neglected the second solution with $k \to -k$ for clarity). As predicted in our calculation, $I_{\mathrm{T}}(k_i, k_f; \omega)$ is strongly suppressed in this region, apart from the thin line at $\omega \simeq 0$. However, the line is an artifact of the atom- photon bound state and thus not covered in our calculation.

4.4 Band-edge effects

After having finished the discussion of the quasi-linear regime, we now focus on the band edge. As discussed in Sec. 4.2.2, here we assume a dispersion relation of the form $\epsilon(k) = tk^2$ $(t > 0)$. This dispersion relation induces branch-cuts into the analytic structure of ${}_2G_{\mathrm{e,r}}(k;\omega)$, thus making it impossible for us to compute ${}_2G^{(i)}_{\mathrm{e}}(k_f, k_i; \omega)$ analytically. From a more physical point of view, however, we expect that the higher-order processes encapsulate the effect of interaction-induced radiation trapping (IIRT) [76, 77]. This phenomenon describes the excitation of the atom-photon bound state by a two-photon pulse as the result of a nonlinear process. This expectation can be motivated by the diagrammatic form of ${}_2G^{(3)}_{\mathrm{e}}(k_f, k_i; \omega)$,

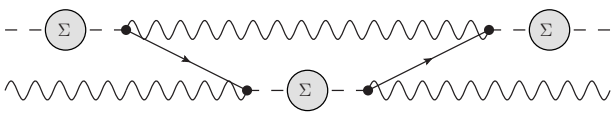

In the top line the TLS emits a photon, which is reabsorbed at a later time. This is exactly the behavior one would expect from the atom-photon bound state, since the radiation cannot leave the TLS.

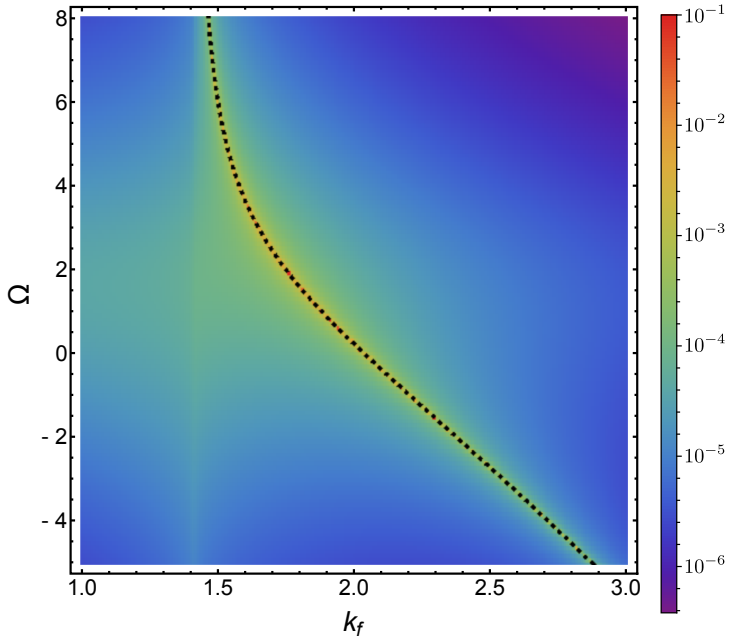

Figure 4.3: *Logarithmic plot of* $\left|{}_2G_{\mathrm{e}}^{(3)}(k_f, k_i; \omega)\right|$ *with* $k_i = p_i = 1$, $t = 1$, $U = 1$, $\omega = \epsilon(k_1) + \epsilon(k_2)$. *We have added a small imaginary part* $\delta = 10^{-3}$ *to* ω *for an artificial broadening of the resonance. The black dotted line represents the solution of* $\omega = \omega_{\mathrm{BS}} + \epsilon(k_f)$. *The resonance approaches* $k_f \to \sqrt{2}$ *for large values of* Ω, *since the bound state energy* $\omega_{BS} \to 0$ *in this case.*

The prototypical process of IIRT includes two initial photons, which are transformed into an atom-photon bound state and a photon with a different momentum. Energetically, this process is described by

$$\omega = \epsilon(k_i) + \epsilon(p_i) = \omega_{\mathrm{BS}} + \epsilon(k_f), \tag{4.21}$$

where k_i and p_i are the momenta of the initial photons, k_f is the momentum of the final photon, ω is the total energy and ω_{BS} is the energy of the atom-photon bound state. This energy can be determined from the poles of ${}_1G_{\mathrm{e,r}}(\omega)$, or equivalently

$$\left[{}_1G_{\mathrm{e,r}}(\omega)\right]^{-1} = \omega_{\mathrm{BS}} - \Omega + i\frac{U^2\pi}{\sqrt{t\omega_{\mathrm{BS}}}} = 0. \tag{4.22}$$

In fact, setting ${}_2G_{\mathrm{e}}^{(3)}(k_f, k_i; \omega)$ on-shell (thus making it proportional to a scattering matrix element) and computing the integration over the internal momenta numerically yields a sharp peak at precisely the momenta k_f which fulfill $\omega = \omega_{\mathrm{BS}} + \epsilon(k_f)$ (cf. Fig. 4.3). This indicates that ${}_2G_{\mathrm{e}}^{(3)}(k_f, k_i; \omega)$ (together with the higher-order processes) describes indeed the physics behind the IIRT. Moreover, treating the sharp peak as a pole (which is motivated by the fact that the width of the resonance scales with the small imaginary part $i\delta$) enables us to compute

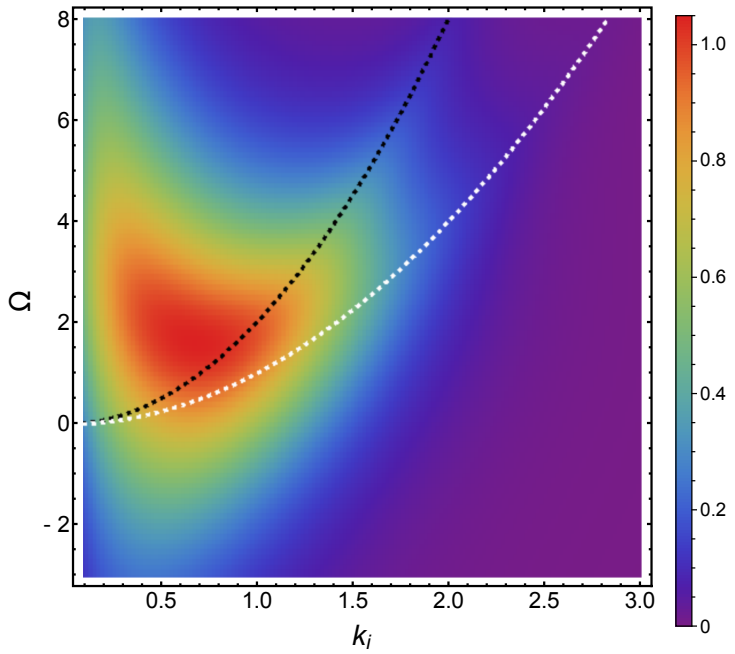

Figure 4.4: *Plot of* $\left|Res\left[{}_2G_{\mathrm{e}}^{(3)}, k_0\right]\right|$ *for two identical initial photons* $\omega = 2\epsilon(k_i)$, $U = 1$, $t = 1$, $\delta = 10^{-4}$ *and* $\eta = 10^{-6}$. *The black and white lines represent the parabolas* $\Omega = 2\epsilon(k_i)$ *and* $\Omega = \epsilon(k_i)$, *respectively.*

the residue of the resonance via

$$\mathrm{Res}\left[{}_2G_{\mathrm{e}}^{(3)}, k_0\right] = \frac{1}{2\pi i}\oint_C \mathrm{d}z\, {}_2G_{\mathrm{e}}^{(3)}(z, k_i; \omega)\Big|_{\mathrm{os}}, \tag{4.23}$$

where k_0 is the solution of Eq. (4.21), the subscript os indicates again that the expression is taken on-shell and the contour C is a circle centered at k_0 with radius η. We have plotted the residue in Fig. 4.4, together with the conditions that the two initial photons are on resonance with the TLS individually ($\Omega = \epsilon(k_i)$) and collectively ($\Omega = \omega = 2\epsilon(k_i)$). We can see here that the strength of the pole is sensitive to the TLS being on resonance with the collective photonic excitation, rather than with the individual ones. This is another indicator that IIRT emerges as the result of the nonlinear behavior of the TLS in the presence of two or more photons. Furthermore, this result shows that an analytic solution for ${}_2G_{\mathrm{e}}^{(3)}(k_f, k_i; \omega)$ is still highly desirable since it would gain further insight to the physics of IIRT.

Finally, we would like to conclude by recalling the physical interpretation of each term in the perturbation series of ${}_2G_{\mathrm{e}}(k_f, k_i; \omega)$: The first term describes the single-photon scattering and does not induce correlations between the two photons. The second term gives rise to photon bunching and is always finite, independent of the dispersion relation. The third term and all higher order terms are nontrivial, since they include integrations over internal momenta. In the case of a linear dispersion relation they give no contribution, but in the presence of a band

edge these terms are responsible for the effect of IIRT. To make the connection to the Feynman diagrams clear, we show again the perturbation series of ${}_2G_{\mathrm{e}}(k_f, k_i; \omega)$,

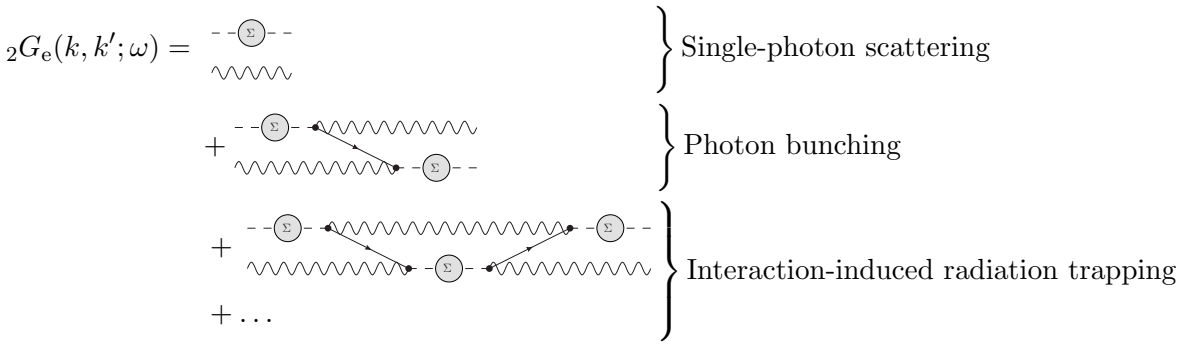

4.5 Conclusion

In this chapter we have discussed the implications of a nonlinear dispersion relation on the two-excitation TLS-Green's function. For a linear dispersion relation the perturbation series of the Green's function breaks down. Hence we focused on the nonvanishing terms for dispersion relations beyond linear. For energies far away from band edges and only a small band curvature γ we were able to find an analytical perturbative expansion of the Green's function in the small parameter γ/v. These calculations show that higher order terms are strongly suppressed and the dominant contributions stem from renormalizations of the lower order terms, which translate to renormalized poles in the scattering matrix. In the other limit of energies close to the band edge, we have performed a phenomenological calculation which focused on new physical effects. Indeed, we have found that the higher order terms contribute IIRT, an effect that has not been included in the lower order diagrams. Furthermore, our analysis shows that the two incoming photons should be tuned collectively on resonance with the TLS rather than individually to enhance the IIRT.

5 WAVEGUIDE QED IN TIME-DOMAIN: THE ROLE OF THE PHOTONIC PULSE WIDTH

After having established the Green's functions for waveguide QED in frequency-domain in the last chapters, we consider here the Green's functions in time-domain. These Green's functions are used to calculate the time-evolution of one- and two-photon pulses, where we provide in both cases analytical formulas for the wavefunctions at all times. We find that the determining factor of the scattering behavior and the atomic excitation is the ratio between the photonic pulse width in real space σ and the TLS decay time τ. Numeric calculations on a tight-binding chain support our results and give limits regarding band curvature.

5.1 Introduction

In the last two chapters we have presented a theoretical formalism to describe the scattering behavior of few-photon states on quantum emitters coupled to a one-dimensional waveguide. These calculations where carried out in the frequency-momentum domain and assumed δ-like excitations to compute the scattering matrix. On the other hand, experiments focusing on the generation of single- and few-photon sources [36, 92–95] have reported a specific temporal profile of the photonic pulse, depending on the generation procedure [96]. Recently, techniques have been developed which are able to transform the temporal profile into a more or less arbitrary shape [97–100]. Thus, it is interesting how the temporal profile of the photon alters the results obtained by δ-like excitations.

From a theoretical point of view, most of the publications have focused on the stationary regime [50, 51, 55, 56, 74]. However, calculations in the time-domain are also desirable, since they take the temporal profile of the photon into account and could furthermore provide access to correlation functions [101]. Up to now, calculations in time-domain are either carried out numerically by propagating a wavefunction on a tight-binding chain [75, 76, 78, 79, 81] or

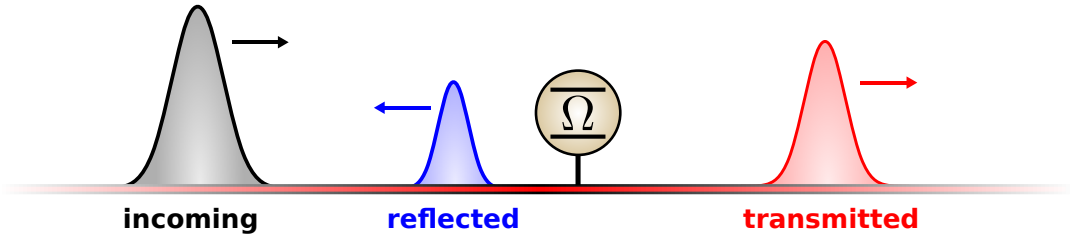

Figure 5.1: *Sketch of the model together with a prototypical scattering process of an incoming photonic wavepacket, which is transformed into a reflected and a transmitted part.*

by solving the equations of motion, which leads to analytical results in the single-excitation sector [69] but requires numerical support in the two-excitation sector [70, 71].

We analyze in this chapter the effect of the temporal shape of the photon on the scattering behavior and the maximal TLS excitation. Fig. 5.1 shows a prototypical scattering process: We initialize a photonic wavepacket, which scatters on the TLS and is divided in a transmitted and a reflected part. The calculations are carried out by propagating wavefunctions in time by means of Green's functions in space-time domain, where we find analytical expressions for the propagated wavefunctions in the single- and two-excitation sector for a linear dispersion relation. The analysis shows that depending on the ratio between the photonic pulse width σ and the TLS decay time τ the system can be classified into three regimes. Finally, we investigate the implications of band curvature on our results with the help of numerical calculations on a tight-binding chain.

5.2 Fundamentals

We are interested in this chapter in the propagation of wavefunctions $|\Psi(x,t_0)\rangle$ from an initial time t_0 to a later time t by means of Green's functions. This is obtained by employing the main formula of this chapter [91],

$$|\Psi(x',t)\rangle = \int \mathrm{d}x\, \hat{G}(x',t;x,t_0)|\Psi(x,t_0)\rangle, \tag{5.1}$$

which is given here in terms of a generic Green's function $\hat{G}(x',t;x,t_0)$ in space-time domain. This equation can be understood by recalling that the Green's function propagates particles, or alternatively δ-like excitations, from one space-time-point to another. The above equation is thus a generalization of this concept to spatially extended excitations.

For our purpose we use the Green's functions defined in Chapter 3 and Fourier transform them to space-time domain (the actual form of the wavefunction $|\Psi(x,t_0)\rangle$ and the Green's function $\hat{G}(x',t;x,t_0)$ is given in the corresponding section). We restrict ourselves to the case of a linear dispersion relation here since we have in this case exact analytical expressions in the single- and two-excitation sector.

5.2.1 Single-excitation sector

We start with the single-excitation sector, i.e. we employ the Green's functions derived in Sec. 3.2.1. According to Eq. (3.5), the Green's function already carries a matrix structure. However, the matrix structure takes only the state of the TLS into account. Therefore, we generalize the matrix structure as

$$ {}_1\hat{G} = \begin{pmatrix} {}_1\hat{G}_{\mathrm{e}} & {}_1\hat{G}_{\mathrm{ab}} \\ {}_1\hat{G}_{\mathrm{em}} & {}_1\hat{G}_{\mathrm{w}} \end{pmatrix} = \left(\begin{array}{c|cc} {}_1G_{\mathrm{ee}} & {}_1G_{\mathrm{Re}} & {}_1G_{\mathrm{Le}} \\ \hline {}_1G_{\mathrm{eR}} & {}_1G_{\mathrm{RR}} & {}_1G_{\mathrm{LR}} \\ {}_1G_{\mathrm{eL}} & {}_1G_{\mathrm{RL}} & {}_1G_{\mathrm{LL}} \end{array}\right), \tag{5.2} $$

to take the different chirality configurations of the photon into account. We suppressed here the space-time coordinates for a shorter notation. Furthermore, we have chosen a slightly different notation than in the previous chapters: ${}_1G_{\mathrm{ee}}$ is the TLS-Green's function, ${}_1G_{\mu_i\mu_f}$ is the waveguide Green's function with the respective initial and final chiralities μ_i and μ_f and ${}_1G_{\mu_i\mathrm{e}}$ and ${}_1G_{\mathrm{e}\mu_f}$ are the absorption and emission Green's functions, respectively. The idea behind this nomenclature is to indicate the initial and final state of the system by the two subscripts.

Within this matrix structure, the wavefunction assumes the form

$$ |{}_1\Psi(x,t)\rangle = \begin{pmatrix} {}_1\Psi_{\mathrm{e}}(t) \\ {}_1\Psi_{\mathrm{R}}(x,t) \\ {}_1\Psi_{\mathrm{L}}(x,t) \end{pmatrix}, \tag{5.3} $$

where the components represent

- a TLS in the excited state and no photon in the waveguide,
- a TLS in the ground state and a right-moving photon in the waveguide
- a TLS in the ground state and a left-moving photon in the waveguide

respectively.

The calculation of the propagated wavefunction has been relegated to Appendix D since the resulting formulas are quite bulky. With the propagated wavefunctions we can define the waveguide occupation as

$$ {}_1P_{\mathrm{ph}}(x,t) = |{}_1\Psi_{\mathrm{R}}(x,t)|^2 + |{}_1\Psi_{\mathrm{L}}(x,t)|^2 \tag{5.4} $$

and the TLS excitation as

$$ {}_1P_{\mathrm{e}}(t) = |{}_1\Psi_{\mathrm{e}}(t)|^2. \tag{5.5} $$

We will use these formulas in Sec. 5.3 to analyze the photonic scattering behavior and the maximal TLS excitation.

5.2.2 Two-excitation sector

The matrix structure of the Green's function has to be extended once more in the two-excitation sector due to the appearance of an additional photon,

$$ {}_2\hat{G} = \begin{pmatrix} {}_2\hat{G}_{\mathrm{e}} & {}_2\hat{G}_{\mathrm{ab}} \\ {}_2\hat{G}_{\mathrm{em}} & {}_2\hat{G}_{\mathrm{w}} \end{pmatrix} = \left(\begin{array}{cc|ccc} {}_2G_{\mathrm{Re,Re}} & {}_2G_{\mathrm{Le,Re}} & {}_2G_{\mathrm{RR,Re}} & {}_2G_{\mathrm{RL,Re}} & {}_2G_{\mathrm{LL,Re}} \\ {}_2G_{\mathrm{Re,Le}} & {}_2G_{\mathrm{Le,Le}} & {}_2G_{\mathrm{RR,Le}} & {}_2G_{\mathrm{RL,Le}} & {}_2G_{\mathrm{LL,Le}} \\ \hline {}_2G_{\mathrm{Re,RR}} & {}_2G_{\mathrm{Le,RR}} & {}_2G_{\mathrm{RR,RR}} & {}_2G_{\mathrm{RL,RR}} & {}_2G_{\mathrm{LL,RR}} \\ {}_2G_{\mathrm{Re,RL}} & {}_2G_{\mathrm{Le,RL}} & {}_2G_{\mathrm{RR,RL}} & {}_2G_{\mathrm{RL,RL}} & {}_2G_{\mathrm{LL,RL}} \\ {}_2G_{\mathrm{Re,LL}} & {}_2G_{\mathrm{Le,LL}} & {}_2G_{\mathrm{RR,LL}} & {}_2G_{\mathrm{RL,LL}} & {}_2G_{\mathrm{LL,LL}} \end{array}\right). \tag{5.6} $$

Again, we have modified the notation slightly to incorporate the individual chiralities of the photons: ${}_2G_{\mu_i\mathrm{e},\mu_f\mathrm{e}}$ is the TLS-Green's function, ${}_2G_{\mu_i\nu_i,\mu_f\nu_f}$ the waveguide Green's function, ${}_2G_{\mu_i\nu_i,\mu_f\mathrm{e}}$ the absorption and ${}_2G_{\mu_i\mathrm{e},\mu_f\nu_f}$ the emission Green's function with initial chiralities μ_i and ν_i and final chiralities μ_f and ν_f.

The wavefunction is then given by

$$ |{}_2\Psi(x,y;t)\rangle = \begin{pmatrix} {}_2\Psi_{\mathrm{Re}}(x,t) \\ {}_2\Psi_{\mathrm{Le}}(x,t) \\ {}_2\Psi_{\mathrm{RR}}(x,y,t) \\ {}_2\Psi_{\mathrm{RL}}(x,y,t) \\ {}_2\Psi_{\mathrm{LL}}(x,y,t) \end{pmatrix}, \tag{5.7} $$

where the components represent

- a TLS in the excited state and one right-moving photon in the waveguide
- a TLS in the excited state and one left-moving photon in the waveguide
- a TLS in the ground state and two right-moving photons in the waveguide
- a TLS in the ground state and one right-moving and one left-moving photons in the waveguide
- a TLS in the ground state and two left-moving photons in the waveguide

respectively.

The propagated wavefunctions together with their derivation can be found in Appendix E. Furthermore, the (combined) probability to find a photon at position x and the other one at position y is given by

$$ {}_2P_{\mathrm{ph}}(x,y,t) = \sum_{\mu\nu} |{}_2\Psi_{\mu\nu}(x,y,t)|^2 \tag{5.8} $$

and the probability to find an excited TLS is defined as

$$ {}_2P_{\mathrm{e}}(t) = \sum_{\mu} \int \mathrm{d}x |{}_2\Psi_{\mu\mathrm{e}}(x,t)|^2. \tag{5.9} $$

The analysis of the photonic scattering behavior and the maximal TLS excitation in the two-excitation sector can be found in Sec. 5.4.

5.2.3 Further considerations

For our analysis we initialize the photons in the form of a Gaussian wavepacket,

$$g_{\mathbf{p}}(x) = \pi^{-1/4}\sigma^{-1/2}e^{-\frac{(x-x_0)^2}{2\sigma^2}+ik_0x}, \tag{5.10}$$

where $g_{\mathbf{p}}(x)$ has been normalized to $\int \mathrm{d}x|g_{\mathbf{p}}(x)|^2 = 1$ and the subscript is meant as a superparameter including the center of the Gaussian x_0, the width σ and the momentum k_0.

Moreover, we have a closer look at the different scales involved here: Since the considerations in this chapter are performed in the field limit we have neglected the effects of system-inherent scales like lattice spacing. Nevertheless, there exists a scale which is induced by the TLS-waveguide coupling: The spontaneous emission time of the TLS $\tau = v/U^2$ (cf. Eq. (3.41) and Eq. (3.53)) which can also be transformed into a length scale via $l = v\tau$. Moreover, another length scale is introduced when the system is subjected to a photonic pulse with a finite width σ. Furthermore limiting the parameter space by setting the photons on resonance with the TLS, $\epsilon(k_0) = \Omega$, leaves only the two scales σ and $l = v\tau$ as tuning parameters. We will thus analyze the scattering behavior and the maximal TLS excitation with respect to these two parameters.

5.3 Single-excitation sector

We start with the single-excitation sector and initialize a right-moving photon in the waveguide,

$$_1\Psi_{\mathrm{R}}(x,0) = g_{\mathbf{p}}(x), \qquad _1\Psi_{\mathrm{L}}(x,0) = {}_1\Psi_{\mathrm{e}}(0) = 0. \tag{5.11}$$

As already noted, the propagated wavefunction together with the according Green's functions are given in Appendix D.

In Fig. 5.2(a), we have plotted the maximal excitation of the TLS over σ and τ (the other parameters are given in the caption). The maximal excitation of the TLS is $\max[{}_1P_{\mathrm{e}}(t)] \approx 0.4$, which is in agreement with previous results [69]. Higher excitations can be achieved when the photon is subjected to a beam splitter and inserted to the waveguide from both sides with 50% probability [68], by optimizing the pulseshape [68] or by setting the TLS at an optimized distance to the end of a waveguide [69]. From the cone-like structure of Fig. 5.2(a), we can infer that the maximal TLS excitation depends only on one dimensionless parameter $\sigma/v\tau$, where $\sigma/v\tau \approx 0.47$ gives the highest excitation.

The parameter $\sigma/v\tau$ is the ratio of the two scales left to the system and is the only relevant parameter to describe its properties, at least for a given time scale. The time scale can be either defined by τ or σ/v and can be used to maximize the duration of the TLS excitation, for example. The value of $\sigma/v\tau$ has also effects on the wavefunction of the scattered photons. In Fig. 5.3, we show ${}_1P_{\mathrm{ph}}(x,t)$ long after the interaction with the TLS for different values of $\sigma/v\tau$. We find that the properties of the scattered wavefunction depend strongly on the value of $\sigma/v\tau$: for $\sigma/v\tau \gg 1$, the incoming wavepacket is almost perfectly reflected, as predicted by stationary calculations [49, 50, 74, 75], whereas there seems to be no effect on the wavepacket for $\sigma/v\tau \ll 1$. In the case of $\sigma/v\tau = 0.47$, the wavepacket is split up into a right- and leftmoving part and is also deformed.

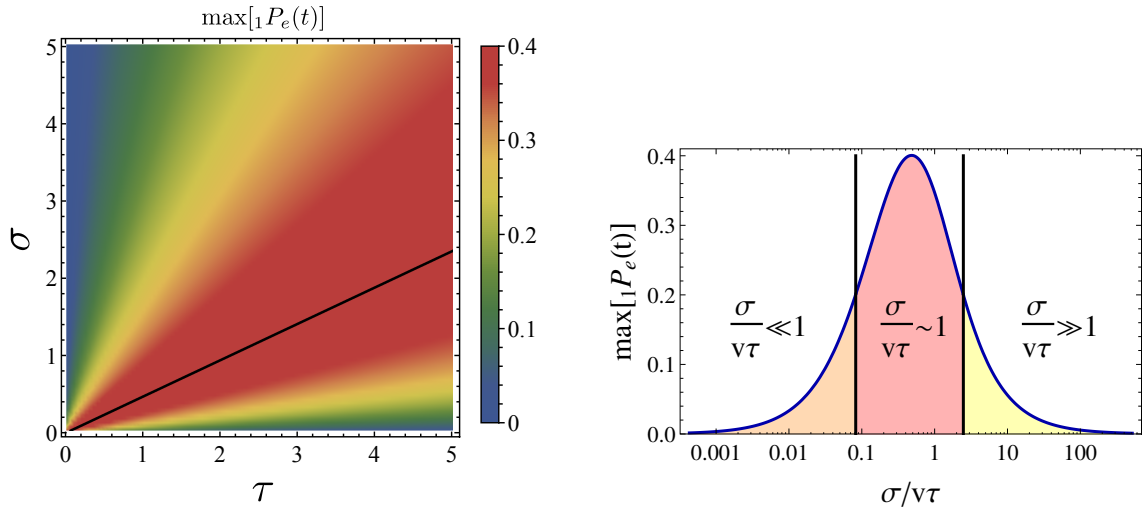

(a) (b)

Figure 5.2: *(a)Maximal TLS excitation over σ and τ, with $\Omega = vk_0 = 2$, $x_0 = -20$ and $v = 1$. The black line is runs through the points with the highest excitation and is given by $\sigma \simeq 0.47v\tau$.*
(b) Plot of the maximal TLS excitation over the dimensionless parameter $\sigma/v\tau$, together with the different regimes (see text for details). The borders of the regimes have been chosen such that $\max[{}_1P_e(t)]$ is half the value of the absolute maximal TLS excitation.

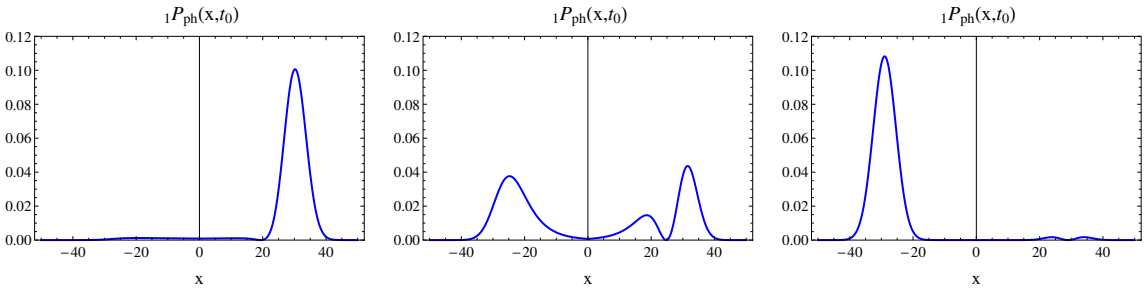

(a) (b) (c)

Figure 5.3: *Photonic distribution ${}_1P_{\mathrm{ph}}(x, t_0)$ for the parameters $v = 1$, $\Omega = vk_0 = 2$ and $x_0 = -20$. The time $t_0 = 50$ is chosen in such a way that the peak of the initial photon has moved far away from the TLS. Moreover, U has been tuned such that $\sigma/v\tau = 0.47\alpha$, where $\alpha = 0.1, 1, 10$ in (a), (b) and (c) respectively.*

Combining the results for the maximal TLS excitation and the scattered photon leads to three regimes, as shown in Fig. 5.2(b):

- $\sigma/v\tau \ll 1$: The maximal TLS excitation is very low and the photon passes the TLS merely undisturbed, indicating low interaction between the TLS and the photon.
- $\sigma/v\tau \sim 1$: The TLS excitation is maximized and the TLS strongly modifies the shape of the photonic wavefunction.
- $\sigma/v\tau \gg 1$: The maximal TLS excitation is very low and the TLS acts as a mirror, as predicted by stationary calculations.

This strong correlation between the distribution of the scattered photonic wavefunction and the maximal TLS excitation helps tuning the system into the desired regime or can be used for indirect measurements, for example. Note that the transition between the regimes is smooth, which means that a reasonably high TLS excitation together with a TLS acting as a mirror can be realized by carefully tuning the system. Furthermore, we would like to point out that these regimes exist for even for arbitrary small, yet non-zero U and can be accessed by sufficiently large pulse widths.

5.4 Two-excitation sector

In the two-excitation sector we initialize two right-moving, bosonically symmetrized photons, i.e.

$$ {}_2\Psi_{\mathrm{RR}}(x,y;0) = \mathcal{N}\Big\{ g_{\mathbf{p}}(x)g_{\mathbf{q}}(y) + g_{\mathbf{p}}(y)g_{\mathbf{q}}(x) \Big\}, \tag{5.12}$$

and all other components being zero, where the normalization constant is given by[1]

$$ \mathcal{N} = \frac{1}{\sqrt{2 + 2|\int \mathrm{d}x g_{\mathbf{p}}(x) g^*_{\mathbf{q}}(x)|^2}}. \tag{5.13}$$

We have propagated these wavefunctions by employing Eq. (5.1), where the actual calculation as well as the results are shown in Appendix E.

We choose the parameters of the two photons such that they are identical and individually on resonance with the TLS, i.e.

$$ x_0 = y_0, \qquad vk_x = vk_y = \Omega, \qquad \sigma_x = \sigma_y, \tag{5.14}$$

where all parameters with an x belong to the superparameter $\mathbf{p}$, and the ones with y to $\mathbf{q}$. Performing the same analysis for the maximal TLS excitation as in Sec. 5.3, we find that it depends again on the dimensionless parameter $\sigma/v\tau$. As shown in Fig. 5.4, the TLS excitation maximizes at $\sigma/v\tau \approx 0.33$, where the TLS reaches a value of ${}_2P_{\mathrm{e}}(t) \approx 0.59$, which is roughly 150% of the result for a single photon.

[1] The normalization constant stems from the condition $\int \mathrm{d}x\mathrm{d}y\, |{}_2\Psi_{\mathrm{RR}}(x,y;0)|^2 = 1$ and the overlap integral is rooted in the bosonic symmetrization of the wavefunction.

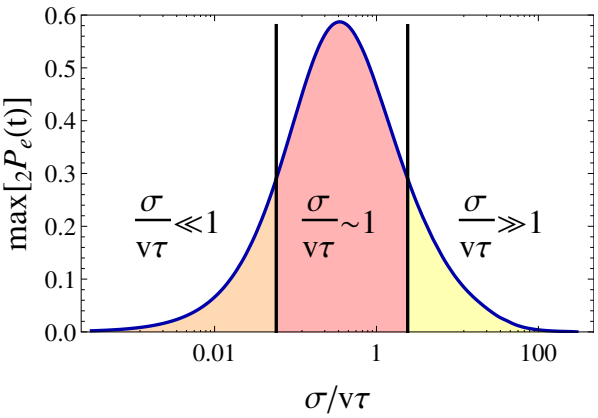

Figure 5.4: *Plot of the maximal TLS excitation over the dimensionless parameter $\sigma/v\tau$ for an initial wavefunction containing two photons. In analogy to Fig. 5.2(b), we have again included the different regimes.*

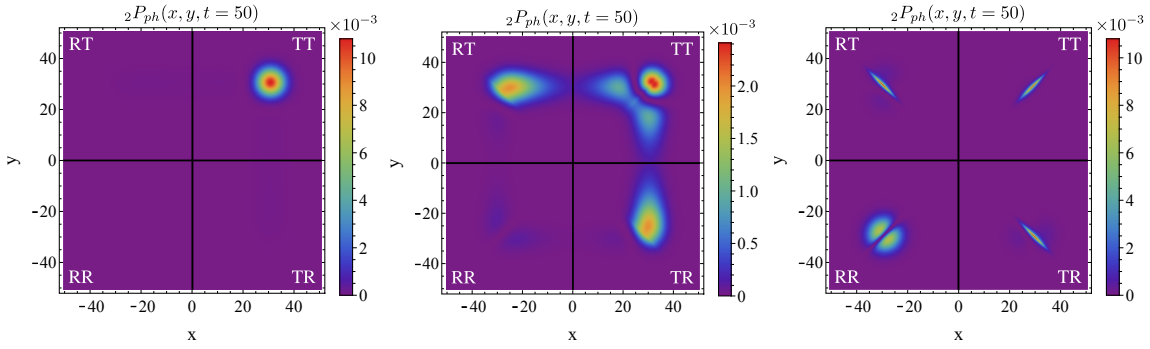

Figure 5.5: *Photonic distribution $_2P_{\mathrm{ph}}(x, y, t_0)$ for the parameters $v = 1$, $\Omega = vk_x = vk_y = 2$, $x_0 = y_0 = -20$ and $t_0 = 50$ is long after the peak of the photon hits the TLS. U has been tuned such that $\sigma/v\tau = 0.33\alpha$, where $\alpha = 0.1, 1, 10$ in (a), (b) and (c) respectively.*

We have also plotted the photonic distribution ${}_2P_{\mathrm{ph}}(x, y, t)$ after scattering off the TLS in Fig. 5.5, which can be interpreted as the probability to find a photon at x and another one at y. The black cross at $x = 0$ and $y = 0$ indicates the position of the TLS[2]. We have initialized a rightmoving two-photon wavepacket at $x_0 = y_0 = -50$ (the other parameters are given in the caption), which means that after the scattering, photons in the bottom left quadrant are both reflected, the ones in the top right quadrant are both transmitted and in the other two quadrants one photon is transmitted and one is reflected. Note that the distribution is symmetric with respect to the diagonal $x = y$ due to the bosonic symmetry of the photonic wavepacket.

In contrast to the case of a single photon, the TLS acts as a nonlinearity in the presence of two and more photons [77]. This can be seen in Fig. 5.5(c), where the scattered photons are strongly correlated [51, 52]: The part of the wavepacket where both photons are transmitted is strongly localized around the diagonal $x = y$, which can be interpreted as photon bunching [79, 89], whereas the photons which are both reflected show antibunching behavior. The photons in the remaining quadrants are strongly localized around the diagonal $x = -y$, which indicates entanglement between two photons moving in different directions. In Fig. 5.5(b), the system is tuned to the maximal TLS excitation, which leads to a delocalized photon distribution. The long tail pointing to the TLS can be explained by the high excitation, which takes a long time to decay. Note that in this case there occurs almost no double reflection of photons. For the parameters chosen in Fig. 5.5(a) the photonic wavepacket passes the TLS merely undisturbed, similar to the case of a single photon.

In analogy to Sec. 5.3, we are able to identify three different regimes by combining Fig. 5.4 and 5.5:

- $\sigma/v\tau \ll 1$: The maximal TLS excitation is very low and the photon passes the TLS merely undisturbed, leading to no additional correlation.
- $\sigma/v\tau \sim 1$: The TLS excitation is maximized, which leads to a highly delocalized photon distribution where double reflection is almost absent.
- $\sigma/v\tau \gg 1$: The maximal TLS excitation is very low and the TLS induces a strong correlation between the photons.

In addition to the effects in the single-excitation sector, the TLS induces here correlations between the two photons. The strength and properties of these correlations depends on the regime and can be tuned by external parameters.

5.5 The role of band curvature

So far we have focused on the case of a linear dispersion relation, where we were able to obtain analytical formulas for the propagated wavefunctions. The framework presented here is in general also capable to propagate wavefunctions in a waveguide with a nonlinear dispersion relation. However, Fourier transforming the Green's function from Chapter 3 for a nonlinear

[2]Note that the whole black cross indicates the TLS position since at least one photon is at the TLS.

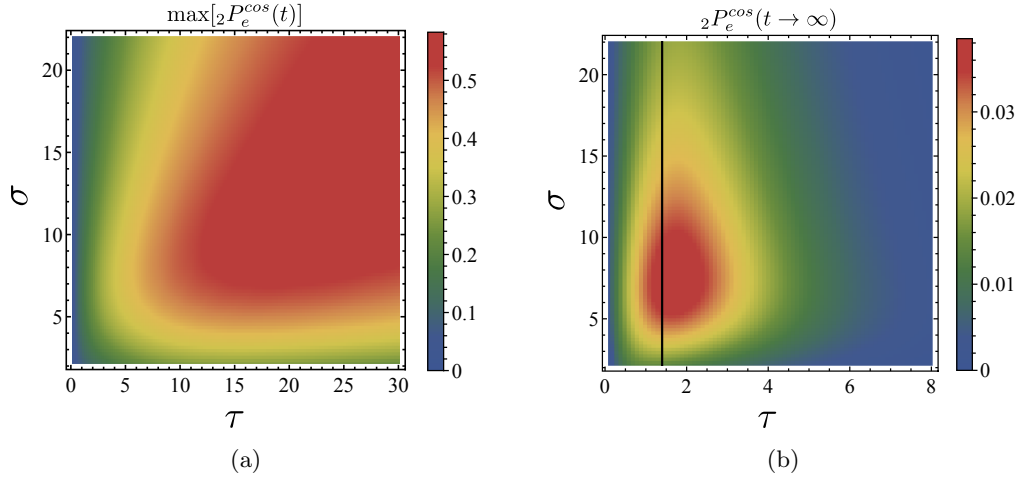

Figure 5.6: *(a)Maximal TLS excitation over σ and τ for a tight-binding waveguide with a cosine-dispersion relation subjected to two identical photons with $x_0 = y_0 = 50$, $\sigma_x = \sigma_y = \sigma$, $k_x = k_y = 3\pi/4a$. The parameters of the Hamiltonian are set to $J = 1$, $\Omega = \sqrt{2}$ and $L = 199$ sites.*
(b) TLS excitation long time after the two-photon wavepacket has hit the TLS. The parameters are the same as in (a), but with $L = 499$ sites. The black line indicates $J = U = 1$.

dispersion relation to space-time domain is a tedious task, since the analytic structure of the Green's functions becomes more complicated (cf. Chapter 4). Instead, we analyze the effects of band curvature and finite lattice spacing by employing the tight-binding Hamiltonian defined in Eq. (2.67). The propagation of the wavefunction is performed by means of the formula

$$|\Psi(t)\rangle = e^{-iH_{tb}(t-t_0)}|\Psi(t_0)\rangle, \tag{5.15}$$

where we utilize a Krylov-subspace based operator-exponential technique [75, 77, 81]. Specifically, we employ the *PPS Photon Simulator*, which was developed in this group by Christoph Martens during his PhD [102]. Nevertheless, we use the Green's function approach to calculate the spontaneous decay time of the TLS, which is defined as

$$\tau(k) = -\mathrm{Im}[{}_1\Sigma(\epsilon(k))]^{-1}. \tag{5.16}$$

Since the tight-binding chain features a cosine-shaped dispersion relation we insert Eq. (3.40) as the self-energy, which is evaluated at $\omega = \epsilon(k)$.

We have plotted the maximal TLS excitation for two photons with momentum $k_x = k_y = 3\pi/4a$ (with lattice spacing a) in Fig. 5.6(a). The plot shows the same cone-like behavior for large enough σ, but for small pulse widths the TLS excitation is significantly lower. This is caused by the nonlinear dispersion relation: Smaller pulse widths in real space lead to larger pulse widths in momentum space, which leads to dispersion and a broadening of the wavepacket.

Hence, the description in terms of the dimensionless parameter $\sigma/v\tau$ is applicable as long as the band curvature is negligible.

Another effect which arises in this system is the IIRT [76, 77], i.e. the efficient excitation of the atom-photon bound state by a two-photon pulse. We have plotted the excitation of the TLS a long time after the interaction with a two-photon wavepacket[3] in Fig. 5.6(b), where we see that the excitation of the atom-photon bound state does not follow the regimes discussed so far in this paper. Instead, the bound state is efficiently excited in a narrow region around $J = U$ (indicated by a black line in Fig. 5.6(b)) and for values of σ around the order of ten. This means that the bound state can only be excited for a system in the strong-coupling regime together with a carefully tuned two-photon pulse. However, we also observe that the excitation becomes smaller for larger pulse widths. This indicates that the cone induced by the ratio $\sigma/v\tau$ (see Fig. 5.6(a)) is still present here but superimposed by the strong-coupling regime.

5.6 Conclusion

We have derived in this chapter the propagated wavefunctions in space-time domain in the single- and two-excitation sector with the help of the Green's functions defined in Chapter 3. We have focused on the propagation of Gaussian wavepackets in a waveguide with a linear dispersion relation, where we obtained analytical results for the propagated wavepackets. Since the calculation has been carried out in the field limit, there are two length scales left to determine the system: The pulsewidth of the photonic wavepacket σ and the spontaneous emission time of the TLS τ, which can be combined to a dimensionless factor $\sigma/v\tau$. Depending on the value of this dimensionless factor, the wavepacket is either almost not interacting with the TLS, exciting the TLS maximally or after the scattering (a)fully reflected in the one-excitation sector and (b)strongly correlated in the two-excitation sector. We have backed up our results with numeric calculations on a tight-binding chain, where we found that the nonlinear dispersion relation plays a significant role for sufficiently narrow pulsewidths. On top of that, we have also found that the pulsewidth plays an important role in the effect of IIRT.

[3] We have terminated the simulation when the wavepacket has hit the boundary of the waveguide.

6 DECAY PROPERTIES OF AN ATOM COUPLED TO A DISORDERED WAVEGUIDE

In this chapter, we analyze the decay properties of a TLS into a disordered waveguide. Adapting techniques from disordered electronic systems we focus on the calculation of the disorder-averaged TLS-Green's function. We find that disorder induces a smearing in the density of states in the vicinity of the band edge, which renders the atom-photon bound states unstable for sufficiently strong disorder. On top of this we find that the disorder can act as a memory kernel, which leads to non-Markovian behavior even for a linear dispersion relation.

6.1 Introduction

As discussed in Sec. 2.3.1 there exists today a great variety of experimental realizations of waveguide QED, ranging from examples in the superconducting regime [28–30] over cold atoms trapped next to a nanofiber [27] to quantum dots coupled to photonic crystal waveguides [33–35]. However, these realizations are not perfect since they are all subjected to fabricational imperfections (called disorder henceforth). Although it usually induces undesired effects, sufficiently strong disorder can be used to trap light by means of Anderson localization [103, 104]. Recently, this effect has been measured in deliberately disordered photonic crystal waveguides [105] and has been exploited to obtain strong coupling between a quantum dot and an Anderson-localized mode [106, 107].

Most of the theoretical efforts have focused on analyzing the effects induced by disorder in photonic crystal waveguides. Starting with the examination of one-dimensional waveguides [108, 109] (i.e. stacked layers of alternating refractive index) there exist frameworks today which are able to calculate the effects of disorder on a line-defect waveguide in a (disordered) two-dimensional photonic crystal [110–113]. These calculations are very close to the abovementioned experimental realizations, where disorder is deliberately introduced by randomly varying the lattice constant in the photonic crystal, as shown in Fig. 6.1.

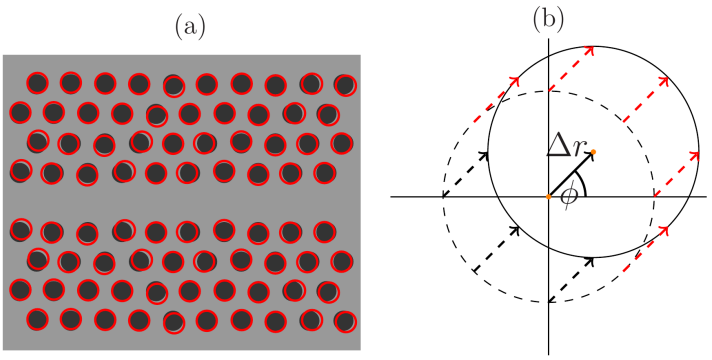

Figure 6.1: *(a)Schematic of a line defect waveguide in a photonic crystal, where the underlying lattice structure (black dots) is disturbed by positional disorder (red circles). (b) Schematic of the positional disorder with magnitude Δr and direction ϕ (adapted from Ref. [111]).*

We analyze here the effects of a disordered waveguide on the coupled TLS-waveguide system, where we focus on the decay properties of the TLS. Adapting techniques from condensed matter theory we include disorder to the Green's functions diagrammatically, where we use two different approximation schemes: First results are obtained by coupling the TLS to an already disorder-averaged waveguide. This has no effect on the TLS-Green's function for a linear dispersion relation. For a cosine dispersion, however, we find that disorder induces a smearing in the density of states at the band edges, which leads to the breakdown of the atom-photon bound state for sufficiently strong disorder. On top of that, we identify a special class of diagrams unique to the setup of waveguide QED. In contrast to the previous approximation these diagrams contribute also when the energy is far away from the band edge, where they induce non-Markovian behavior.

6.2 Fundamentals

In this section we present the fundamental theory of the disordered waveguide. We start by presenting techniques from condensed matter theory which we employ to calculate the Green's function diagrammatically in the presence of disorder. Afterwards we discuss how these techniques can be adopted for the present case of a disordered waveguide.

6.2.1 Disorder in electronics

Disorder plays an important role in condensed matter physics, where it gives rise to effects like Anderson localization [103], weak localization [114] or universal conductance fluctuations [115, 116], but also enters fundamental properties like the conductivity [17]. Due to the importance in the field there exists a variety of excellent textbooks covering the topic of disordered systems [16, 17, 117, 118]. We will follow these textbooks here to give a short introduction to the diagrammatic theory of disordered systems.

Model

A microscopic model for disorder is e.g. given by randomly positioned impurities, which give rise to a randomly fluctuating disorder potential $V(x)$. Electrons in a disordered solid feel this fluctuating potential via their density, hence we can write down the total Hamiltonian as

$$H = H^{\text{clean}} + H^{\text{dis}}, \qquad H^{\text{dis}} = \int \mathrm{d}x V(x) a_x^\dagger a_x. \tag{6.1}$$

Here, H^{clean} is the Hamiltonian of the clean system, H^{dis} describes the random fluctuations on top of the clean system and $a_x^\dagger$ is an electronic creation operator. Since the exact position of the impurities is often unknown in experiments so is the actual form of $V(x)$, which makes it basically impossible to calculate quantities for a given experimental disorder realization. This problem can be overcome by the concept of *ensemble-averaging*, where one averages over many disorder realizations[1]. In this way only statistical properties of $V(x)$ like mean value and autocorrelation functions are relevant, i.e. expressions like

$$\langle V(x)\rangle, \qquad \langle V(x)V(x')\rangle, \qquad \langle V(x)V(x')V(x'')\rangle \quad \text{etc.}, \tag{6.2}$$

where the brackets denote the ensemble-averaging. A common choice for the disorder potential in electronic systems is Gaussian white noise, which is defined by the correlation functions

$$\langle V(x)\rangle = 0, \qquad \langle V(x)V(x')\rangle = U_{\text{dis}}^2 \delta(x - x') \tag{6.3}$$

and is equivalent to the limit of dense point scatterers. Here, U_{dis} describes the strength of the fluctuations. Note that all higher correlation functions with an odd number of disorder potentials $V(x)$ evaluate to zero, whereas the correlation functions with an even number factorize into the two-point correlation function shown above. In momentum space the correlator is given by

$$\langle V(q)V(q')\rangle = U_{\text{dis}}^2 2\pi\delta(q + q'), \tag{6.4}$$

i.e. every disorder potential $V(q)$ which changes the momentum by q is accompanied by another potential $V(-q)$ that restores the original momentum. This is a nontrivial statement: A random potential breaks translation symmetry and thus momentum is not conserved. However, upon ensemble averaging the symmetry is restored and momentum conserved.

Diagrammatics

Diagrammatically, the disorder correlator can be written as

$\langle V(x)V(x')\rangle =$ 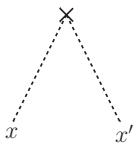

, (6.5)

[1] This is actually automatically realized in nature for large enough systems at sufficiently high temperatures. In this regime the coherence time of the electron is much smaller than the system size and the system becomes *self-averaging*.

where the cross indicates the impurity on which the electron scattered[2]. We can now write down a perturbation series for the electron Green's function in the disorder strength (we depict the electron here as a wavy line to make the connection to the photons in the next section visible),

$G(k) =$ 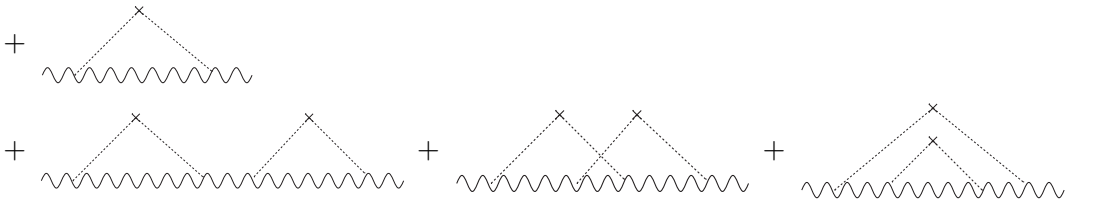

(6.6)

Here, each line corresponds to one order in the perturbation series and the internal Green's functions come with an integration over the corresponding momenta. In second order perturbation theory we find 3 classes of diagrams, where the last two diagrams (with the crossed and nested impurity lines) cannot be constructed from the first order diagram. Higher order terms exhibit an even more complicated structure, including multiple crossing impurity lines combined with nesting, which makes the full summation of the perturbation series a difficult task.

One way to obtain a disorder-induced self-energy is to sum the perturbation series only partially. A convenient choice would be to sum the diagrams which can be constructed with the help the first order diagram. This method is called *first Born approximation* (1BA) and the self-energy is given by

$$\Gamma_{\mathrm{1BA}}(\omega) = \quad = U_{\mathrm{dis}}^2 \int \frac{\mathrm{d}k}{2\pi} G(\omega, k), \tag{6.7}$$

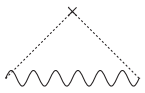

where $G(\omega.k)$ is the electronic Green's functions. In order to take more diagrams into account, we examine the remaining two diagrams from second order perturbation theory in detail. Upon inspecting the diagram with the crossed impurity lines one finds that the available phase space for the internal momentum integration is strongly reduced and the diagram is much smaller than the first-order diagram [118]. Hence, this diagram can be neglected. The diagram with the nested impurity lines, however, is not affected by this phase-space argument and is of comparable size as the first-order diagram. The nested diagrams can be included in the *self-consistent Born approximation* (SCBA), where the self-energy is given by

$$\begin{aligned} \Gamma_{\mathrm{SCBA}}(\omega) = \quad &= U_{\mathrm{dis}}^2 \int \frac{\mathrm{d}k}{2\pi} \langle G(\omega, k) \rangle \\ &= U_{\mathrm{dis}}^2 \int \frac{\mathrm{d}k}{2\pi} \frac{1}{\omega - \epsilon(k) - \Gamma_{\mathrm{SCBA}}(\omega)}. \end{aligned} \tag{6.8}$$

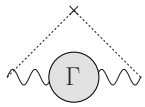

[2]The isolated impurity is not visible in the way the disorder potential is presented here. However, in another, equivalent presentation involving the microscopic impurities one can see that this correlator corresponds to the scattering on a single impurity.

Physics

On a more physical level disorder introduces a new length scale to the system, the so-called *mean-free path*

$$l = v\tau = -v\mathrm{Im}\left[\Gamma(\omega)\right]^{-1}, \tag{6.9}$$

which defines the scale on which an electron can travel unperturbed by disorder. Additionally, the mean-free path defines the limit of weak disorder by means of the formula $k_0 l \gg 1$, where k_0 is some system-specific momentum (in electronic systems it is the Fermi momentum k_f). The perturbative expansion of the Green's function above with the partial summation of diagrams is only valid in the limit of weak disorder. When $k_0 l \sim 1$, all diagrams contribute equally and induce a phase transition to the Anderson-localized regime[3]. In the Anderson-localized regime, all wavefunctions decay exponentially on the length scale of the localization length ξ, which leads to zero transmission, for example. In 1D, an arbitrary small amount of disorder is sufficient to drive the system to the Anderson-localized regime [120]. However, we assume here that the localization length is the largest scale in the system and we can thus treat disorder perturbatively.

The disorder-induced self-energy for waveguide QED in the 1BA can be computed immediately, since the definition is formally identical to Eq. (3.17). With the help of Eq. (3.38), we find for the self-energy

$$\Gamma_{\mathrm{1BA}}(\omega) = -i\pi U_{\mathrm{dis}}^2 \nu(\omega). \tag{6.10}$$

For a linear dispersion relation this expression is a constant and always finite, thus the limit of weak disorder is always fulfilled for a small enough disorder strength. However, for a cosine dispersion relation the DOS diverges at the band edge and leads to a vanishing mean-free path. This behavior is unphysical and is rooted in the crude approximation scheme applied in the 1BA. A more physical result can be achieved within the SCBA, where the additional diagrams renormalize the divergence at the band edge. This leads to a smeared-out DOS at the band edge[4] and to a finite mean-free path. Nevertheless, Anderson localization is more probable at the band edge [104, 122, 123] and although the SCBA gives qualitatively good results it is not entirely clear if it is sufficient to describe the physics also in a quantitatively correct way.

6.2.2 Disorder in photonics

Disorder enters in photonic systems in a different way than in electronic systems. In electronic systems disorder is generated on a microscopic level by impurities, for example, which are differently charged than the atomic background and thus enter as a potential term in the Hamiltonian. Photons, however, do not scatter on differently charged impurities but rather, e.g., on perturbations in the lattice of a photonic crystal like in Fig. 6.1 or due to surface roughness in the waveguide. Disorder enters thus through random fluctuations in the dielectric function $\epsilon(r)$ in the macroscopic Maxwell's equation. Moreover, electrons are scalar particles whereas photons have a vectorial nature with a given polarization, which is an important point

[3] The formula $k_0 l \sim 1$ is also called the *Ioffe-Regel criterion* [119].

[4] Disorder breaks the symmetry of the underlying lattice and introduces states in the formerly forbidden region, the band gap. This leads to the appearance of Lifshitz tails [121] in the DOS.

in the theoretical treatment of disordered photonic crystals [108–113]. Nevertheless, these calculations yield qualitatively similar results as in electronic systems, like the smearing of the DOS at the band edge, for example.

Since the theoretical model laid down in Sec. 2.3.2 has strong similarities to electronic systems and the qualitative effects in photonics are comparable we adopt the electronic disorder scheme and define the Hamiltonian of waveguide QED with disorder as

$$H = H^{\text{clean}} + H^{\text{dis}}, \tag{6.11}$$

where H^{clean} is given by Eq. (2.60) and

$$H^{\text{dis}} = \int \mathrm{d}x V(x) a_x^\dagger a_x, \tag{6.12}$$

in analogy to the electronic case. In addition, we also define a Hamiltonian with a disordered tight-binding chain,

$$H_{\text{tb}} = H_{\text{tb}}^{\text{clean}} + H_{\text{tb}}^{\text{dis}}, \tag{6.13}$$

where $H_{\text{tb}}^{\text{clean}}$ is given by Eq. (2.67) and the disorder enters via the on-site energies[5]

$$H_{\text{tb}}^{\text{dis}} = \sum_i V_{0,i} a_i^\dagger a_i, \tag{6.14}$$

where the $V_{0,i}$ are random numbers following a given distribution. This Hamiltonian is again employed in numerical calculations, which is used to back up the analytical results. Furthermore, we relabel the TLS-waveguide coupling constant $U \to U_{\text{at}}$ to clarify the distinction from the disorder strength U_{dis}.

The drawback here is that we have no indication about the statistical properties of the disorder potential since the Hamiltonian above is not derived from first principles but constructed by heuristic arguments. Hence, we refer again to electronic systems and adopt the Gaussian white noise disorder potential as introduced in Eq. (6.3). In the case of a disordered tight-binding waveguide we choose then the numbers $V_{0,i}$ from a Gaussian distribution with width U_{dis}. Naturally, it would be highly desirable to know the statistical properties of the actual disorder potential. One way would be to expand the Maxwell's equation in a photonic crystal in a Wannier basis, which can be used to extract the dispersion relation of a line-defect waveguide [44, 124]. This technique has also been adapted in disordered photonic crystals [112, 113] to calculate e.g. the DOS of a line-defect waveguide and is in general also capable to calculate the corresponding disorder statistics.

6.3 Density of states effects

6.3.1 The disorder-averaged Green's function

The quantity we are interested in is the disorder-averaged TLS-Green's function $\langle {}_1G_{\text{e}}(\omega)\rangle$, which is presented in the clean case in Sec. 3.2.1. To include the effects of disorder, we follow

[5] This is also called diagonal disorder. Disorder entering the hopping terms is called off-diagonal disorder.

a simple two-step approximation procedure in this section: First, we calculate the disorder-averaged waveguide Green's function $\langle {}_1G^0_{\mathrm{w}}(k;\omega)\rangle$ in the absence of the TLS. Afterwards, we calculate $\langle {}_1G_{\mathrm{e}}(\omega)\rangle$ by coupling the TLS to the already disorder-averaged waveguide. Note that we have again shifted $\omega \to \omega - \Omega/2$.

We include the effects of disorder in the waveguide on the level of the SCBA, i.e. we have to solve the integral

$$\Gamma_{\mathrm{SCBA}}(\omega) = U^2_{\mathrm{dis}} \int \frac{\mathrm{d}k}{2\pi} \frac{1}{\omega - \epsilon(k) - \Gamma_{\mathrm{SCBA}}(\omega)}. \tag{6.15}$$

Since we are working with retarded Green's functions in this thesis, we can assume that $\mathrm{Im}[\Gamma_{\mathrm{SCBA}}(\omega)] < 0$. Furthermore, since $\Gamma_{\mathrm{SCBA}}(\omega)$ does not depend on the momentum k, we can evaluate it following Eqs. (3.17) and (3.38) as

$$\Gamma_{\mathrm{SCBA}}(\omega) = -i\pi U^2_{\mathrm{dis}} \nu(\omega - \Gamma_{\mathrm{SCBA}}(\omega)). \tag{6.16}$$

For a linear dispersion relation the DOS $\nu = (\pi v)^{-1}$ is independent of the energy, therefore

$$\Gamma^{\mathrm{lin}}_{\mathrm{SCBA}} = -i\frac{U^2_{\mathrm{dis}}}{v}. \tag{6.17}$$

However, for a cosine dispersion relation we find with the help of Eqs. (3.17) and (3.40)

$$\Gamma^{\mathrm{cos}}_{\mathrm{SCBA}} = \frac{U^2}{\omega - \Gamma^{\mathrm{cos}}_{\mathrm{SCBA}}(\omega) - 2J} \sqrt{\frac{\omega - \Gamma^{\mathrm{cos}}_{\mathrm{SCBA}}(\omega) - 2J}{\omega - \Gamma^{\mathrm{cos}}_{\mathrm{SCBA}}(\omega) + 2J}} \tag{6.18}$$

This equation can be solved analytically for $\Gamma^{\mathrm{cos}}_{\mathrm{SCBA}}$, giving four solutions. The solutions are not presented here since the expressions are quite large and we do not intend to interpret them. Analyzing these solutions shows that for all values of ω and J only one solution has[6] $\mathrm{Im}[\Gamma_{\mathrm{SCBA}}(\omega)] < 0$. This is the only physically relevant solution, since it agrees with the assumption above. Therefore, we find for the disorder-averaged waveguide Green's function

$$\langle {}_1G^0_{\mathrm{w}}(k;\omega)\rangle = \frac{1}{\omega - \epsilon(k) - \Gamma_{\mathrm{SCBA}}(\omega)}. \tag{6.19}$$

We have plotted the DOS of the disorder-averaged waveguide with a cosine dispersion relation in Fig. 6.2 for various disorder strengths[7]. We can see the van-Hove singularities emerging at the band-edges in the clean case. These singularities become renormalized by disorder, which furthermore leads to a smearing of the DOS.

[6] Note that it is not one solution which gives $\mathrm{Im}[\Gamma_{\mathrm{SCBA}}(\omega)] < 0$ in the whole parameter space. We rather have to check all solutions for a given ω and J and can then identify the correct solution.

[7] The DOS can be obtained via [17]

$$\nu(\omega) = -\frac{\mathrm{Im}\left[{}_1G^0_{\mathrm{w}}(x=0;\omega)\right]}{\pi} = -\frac{\mathrm{Im}\left[\int \frac{\mathrm{d}k}{2\pi} {}_1G^0_{\mathrm{w}}(k;\omega)\right]}{\pi}$$

and has been generalized here to the disorder-averaged Green's function.

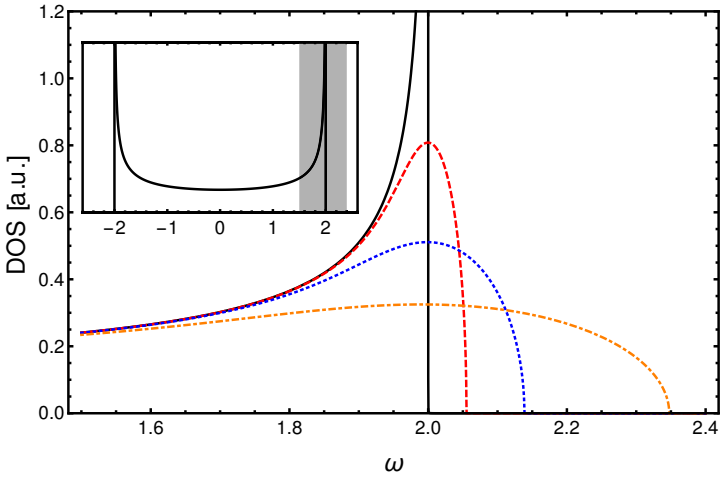

Figure 6.2: *Plot of the smeared-out DOS of the disorder-averaged waveguide with a cosine dispersion relation ($J = 1$) for disorder strengths $U_{\mathrm{dis}} = 0$ (black solid line), $U_{\mathrm{dis}} = 0.1$ (red dashed line), $U_{\mathrm{dis}} = 0.2$ (blue dotted line), $U_{\mathrm{dis}} = 0.4$ (orange dash-dotted line). The inset shows the DOS in the clean case over the full bandwidth.*

We turn now to the calculation of the disorder-averaged TLS-Green's function. In the clean case, it is given by

$$ {}_1G_{\mathrm{e}}(\omega) = \frac{1}{\omega - \Omega - {}_1\Sigma(\omega)}, \qquad \text{with} \qquad {}_1\Sigma(\omega) = U_{\mathrm{at}}^2 \int \frac{\mathrm{d}k}{2\pi} {}_1G_{\mathrm{w}}(\omega, k). \tag{6.20} $$

We perform here a simple approximation and assume that

$$ \langle {}_1G_{\mathrm{e}}(\omega) \rangle = \left\langle \frac{1}{\omega - \Omega - {}_1\Sigma(\omega)} \right\rangle = \frac{1}{\omega - \Omega - \langle {}_1\Sigma(\omega) \rangle} \tag{6.21} $$

holds. Furthermore, combining

$$ \langle {}_1\Sigma(\omega) \rangle = U_{\mathrm{at}}^2 \int \frac{\mathrm{d}k}{2\pi} \langle {}_1G_{\mathrm{w}}(\omega, k) \rangle, \tag{6.22} $$

and Eq. (6.19), we find for the disorder-averaged TLS-Green's function

$$ \langle {}_1G_{\mathrm{e}}(\omega) \rangle = \frac{1}{\omega - \Omega - {}_1\Sigma\left(\omega - \Gamma_{\mathrm{SCBA}}(\omega)\right)}. \tag{6.23} $$

6.3.2 Discussion

Since the dominant effect of disorder in the waveguide is a smearing of the DOS and we have coupled the TLS to an already disorder-averaged waveguide, it is natural to investigate the disorder-induced effects in the TLS with respect to the DOS.

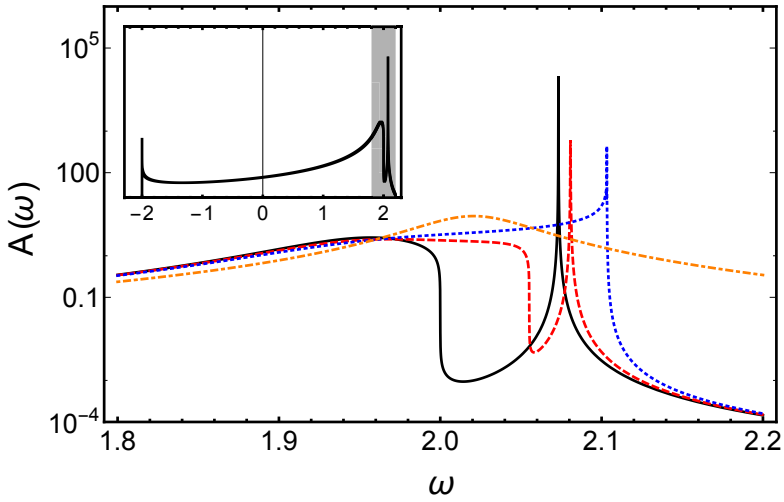

Figure 6.3: *Plot of the spectral density* $\langle {}_1A(\omega)\rangle$ *for* $\Omega = 2$, $U_{\mathrm{at}} = 0.2$ *and* $U_{\mathrm{dis}} = 0$ *(black),* $U_{\mathrm{dis}} = 0.1$ *(red dashed),* $U_{\mathrm{dis}} = 0.16$ *(blue dotted),* $U_{\mathrm{dis}} = 0.5$ *(orange dash-dotted). The inset shows the spectral density for a wider frequency range, where the grey area indicates the frequency range of the large plot. In this plot we have substituted* $\omega \to \omega + i\delta$ *with* $\delta = 10^{-5}$ *for artificial broadening of the resonance*

For a linear dispersion relation the self-energy ${}_1\Sigma$ is independent of ω (cf. Eq. (3.41)). Hence, the disorder self-energy Γ_{SCBA} does not enter the disorder-averaged TLS-Green's function and we find

$$\langle {}_1G_{\mathrm{e}}(\omega)\rangle = {}_1G_{\mathrm{e}}(\omega). \tag{6.24}$$

This behavior is rooted in the fact that $\nu(\omega) = \text{const}$ for a linear dispersion relation, therefore it cannot be smeared out by disorder.

For a cosine dispersion relation this is not the case. We have plotted the spectral density

$$\langle {}_1A(\omega)\rangle = -\frac{\mathrm{Im}[\langle {}_1G_{\mathrm{e}}(\omega)\rangle]}{\pi} \tag{6.25}$$

of the disorder-averaged TLS-Green's function in the vicinity of the band edge for various disorder strengths in Fig. 6.3. In the clean case, the band edge at $\omega = 2$ and the atom-photon bound state to the right are clearly visible and well-separated. We observe that a small disorder strength leads to the expected smearing of the waveguides DOS, accompanied by a small shift of the bound state energy (red dashed curve). With increasing disorder strength, the edge of the DOS moves closer to the bound state resonance and eventually they overlap at a critical disorder strength $U_{\mathrm{dis}}^{\mathrm{crit}}$ (blue dotted curve). For much higher disorder strengths the averaged DOS is very broad and the bound state is no longer supported by the system. In this case the DOS is basically uniform and the resonance transforms to a Lorentzian around the TLS resonance energy Ω.

This transformation can be quantified by expanding the TLS Green's function around the bound state energy ω_{bs}

$$\langle {}_1G_\mathrm{e}(\omega)\rangle \simeq \frac{Z}{(\omega-\omega_{bs})+i\gamma}, \tag{6.26}$$

where the resonance weight Z and width γ are defined as

$$Z = \left(1 - \mathrm{Re}\left[\partial_\omega \langle {}_1\Sigma(\omega)\rangle\Big|_{\omega=\omega_{bs}}\right]\right)^{-1}, \qquad \gamma = -Z\mathrm{Im}[\langle {}_1\Sigma(\omega_{bs})\rangle]. \tag{6.27}$$

We have plotted Z and γ over the disorder strength in Fig. 6.4(a). Here we observe that the bound state weight decreases with increasing disorder strength and the width grows, but very slowly. At $U_\mathrm{dis}^\mathrm{crit}$ the bound state weight reaches its minimal value, whereas the width grows by several orders of magnitude (red line). This indicates that the bound state breaks down for $U_\mathrm{dis} > U_\mathrm{dis}^\mathrm{crit}$ (red shaded region). Note that Eq. (6.26) is not valid anymore in this region, since the isolated resonance disappeared. Physically, this behavior can be understood by the appearance of scattering states in the vicinity of the bound state, which can act as decay channels for the excited TLS.

The calculation above has been carried out in the SCBA, where only a subset of disorder diagrams has been taken into account. In order to check the validity of the above results, we perform additional numerical calculations with the Hamiltonian given by Eq. (6.13). The goal is to construct a quantity which describes similar properties as the spectral density above.

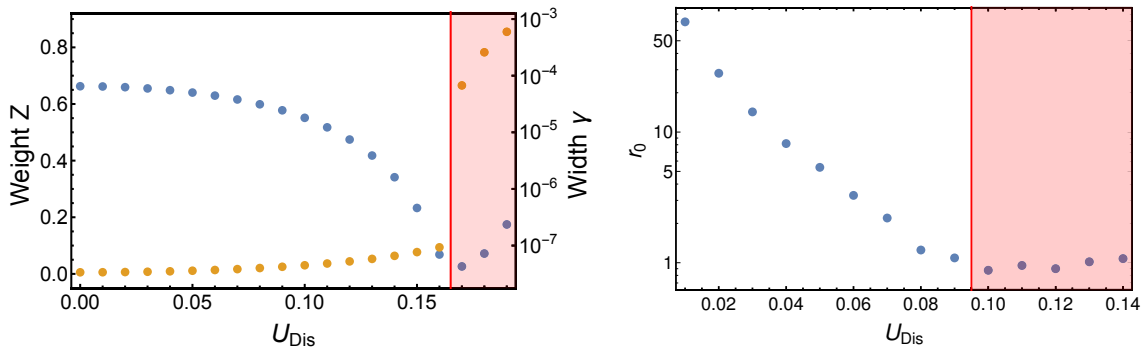

(a) (b)

Figure 6.4: *(a)Plot of the bound state weight Z and width γ for $\Omega = 2$, $U_\mathrm{at} = 0.2$. We have performed the substitution $\omega \to \omega + i\delta$ with $\delta = 10^{-7}$ to broaden the bound state resonance artificially. The width grows by several orders of magnitude in the red shaded region, which indicates the breakdown of the bound state.*
(b)Plot of $\langle r_0\rangle$ over U_dis for $J = 1$, $\Omega = 2$, $U_\mathrm{at} = 0.2$, $L = 2999$ and we have averaged over 500 disorder realizations. Not plotted is the case $U_\mathrm{dis} = 0$, where $r_0 \sim 10^{10}$. In the red shaded region $r_0 \approx 1$, which indicates the breakdown of the bound state.

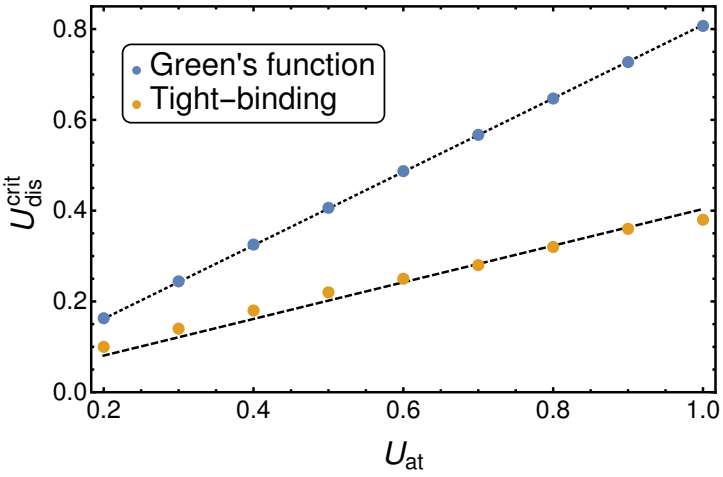

Figure 6.5: *Comparison of $U_{\mathrm{dis}}^{\mathrm{crit}}$ calculated in both ways presented in the text. We have used $\Omega = 2$ and a waveguide with $L = 2999$ sites in the discrete model, where we averaged over 500 realizations. The straight lines show fits of the form $U_{\mathrm{dis}}^{\mathrm{crit}} = mU_{\mathrm{at}}$, which yielded $m \approx 0.4$ and $m \approx 0.81$ for the numeric and analytic solution, respectively.*

Therefore, we investigate the Eigenvalues E_i of the system with size L. The Eigenstates are sorted according to their energy, i.e. in the clean case E_0 and E_L correspond to the atom-photon bound states and the other Eigenvalues to scattering states. The breakdown of the atom-photon bound state can then be seen by the relative neighboring Eigenvalue distance,

$$r_i = \left| \frac{E_i - E_{i+1}}{E_{i+1} - E_{i+2}} \right|. \tag{6.28}$$

When all Eigenvalues belong to scattering states, we can estimate $E_i - E_{i+1} \sim \Lambda/L$ (with the bandwidth Λ and number of waveguide sites L), which leads to $r_i \approx 1$. In the clean system the extremal Eigenvalue E_0 has a finite distance to the band $E_0 - E_1 = \alpha$. Hence we can estimate $r_0 \sim \alpha L/\Lambda \gg 1$ for sufficiently large L. Following the line of reasoning above, r_0 decreases with increasing disorder strength because of the increasing bandwidth and eventually becomes of order one when the bound state breaks down. We have plotted r_0 in Fig. 6.4(b) and find indeed this behavior.

It is already apparent from Fig. 6.4(a) and (b) that both approaches show the breakdown of the bound-state, but nevertheless differ in the value of $U_{\mathrm{dis}}^{\mathrm{crit}}$. In order to compare the two models, we have calculated $U_{\mathrm{dis}}^{\mathrm{crit}}$ for various values of U_{at} in both approaches and plotted it in Fig. 6.5. $U_{\mathrm{dis}}^{\mathrm{crit}}$ was determined in the Green's function approach by minimizing the bound state weight Z and by introducing the condition $r_0 < r_{\mathrm{thresh}}$ in the discrete model, where we set the threshold to $r_{\mathrm{thresh}} = 10^{0.1}$. Both models show that a larger TLS coupling U_{at} leads to a higher stability of the bound state towards disorder. This is due to the fact that the bound state moves further away from the band edge with growing U_{at}. However, we still observe a difference

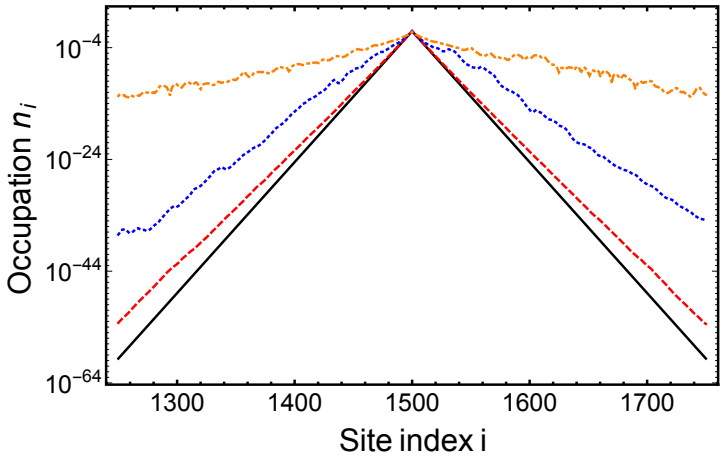

Figure 6.6: *Average waveguide occupation of the state with maximal p_i. The system parameters are $\Omega = 2$, $U_{\mathrm{at}} = 0.2$, $L = 2999$ sites and $U_{\mathrm{dis}} = 0$ (black), $U_{\mathrm{dis}} = 0.05$ (red dashed), $U_{\mathrm{dis}} = 0.1$ (blue dotted) and $U_{\mathrm{dis}} = 0.2$ (orange dash-dotted).*

between both approaches. Since the behavior is to a good approximation linear, we perform fits of the form $U_{\mathrm{dis}}^{\mathrm{crit}} = mU_{\mathrm{at}}$, which yields $m \approx 0.4$ for the disordered tight-binding chain and $m \approx 0.81$ for the Green's function approach[8]. As already noted, we address this discrepancy to the partial summation of diagrams in the SCBA. The SCBA is a good approximation for small disorder, where a partial summation of the perturbation series is sufficient. In the vicinity of the band edge localization effects are more pronounced [104, 123]. This means that all terms in the perturbation series have to be included, and the SCBA is not sufficient anymore. Hence, the result of the tight-binding chain should be more accurate.

Another method to quantify the breakdown of the bound state is via the projection of the Eigenvector with Eigenvalue E_i on the excited TLS $p_i = |\langle E_i|e\rangle|$. For $U_{\mathrm{dis}} < U_{\mathrm{dis}}^{\mathrm{crit}}$, the maximal projection is always given by the bound state, i.e. $\max_i p_i = p_0$, whereas for $U_{\mathrm{dis}} > U_{\mathrm{dis}}^{\mathrm{crit}}$ we find $\max_i p_i = p_j$ with $j \neq 0$. Additionally, we can analyze the waveguide occupation $n_i = \langle a_i^\dagger a_i \rangle$: The atom-photon bound state is characterized by an exponentially decaying envelope centered around the TLS. We have plotted the waveguide occupation of the Eigenvectors which maximize p_i in Fig. 6.6, where we have averaged over 1000 disorder realizations. For sufficiently small disorder we can see that the exponential envelope is still present, but for larger disorder strengths it breaks down and the states become extended over the waveguide, which indicates again the breakdown of the bound state. Note that the states are not extended over the whole space like in the clean case, but are localized around the TLS on the scale of the localization length.

[8] Although both fits differ by a factor of two with a surprisingly high accuracy (0.2%), we believe that this is just a coincidence and not a systematic feature.

6.4 Non-Markovian effects

Up to now, we have included the disorder in the Green's functions in the SCBA, which is an approximation scheme independent of the TLS. We show now that the presence of the TLS produces new terms in the perturbation series which are not covered by the SCBA and lead to new effects.

We start by recalling the perturbation series of the TLS-Green's function coupled to a clean waveguide,

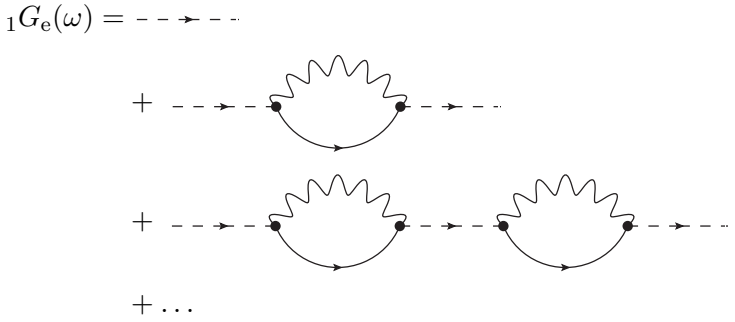

(6.29)

In the approximation scheme applied in the previous section we have substituted the free waveguide Green's function ${}_1G^0_\mathrm{w}(k;\omega)$ with its disorder-averaged counterpart. This means that the disorder correlation function

$\langle V(x)V(x')\rangle =$ 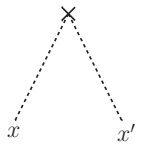 , (6.30)

enters $\langle {}_1G_\mathrm{e}(\omega)\rangle$ only via the waveguide Green's functions which are sandwiched between two TLS-Green's functions (for example the intermediate photon in the second term in Eq. (6.29)). However, the disorder correlator could also lead to diagrams of the form

$\Delta_1 G_\mathrm{e}(\omega) =$ 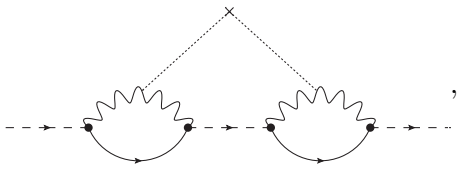 , (6.31)

where we assume that the waveguide Green's functions are already disorder-averaged. This diagram is unique to this setup in the sense that it needs the coupling to the TLS. Furthermore, it is the first nontrivial diagram exhibiting dressing of the TLS. From left to right, the diagram can be read as follows: The excited TLS emits a photon, which scatters off an impurity and is then again absorbed by the TLS. This process is repeated, such that the acquired momentum of the impurity is zero (this follows from the disorder average). Higher order terms would correspond to placing more disorder hats over the one shown above. Physically, the first

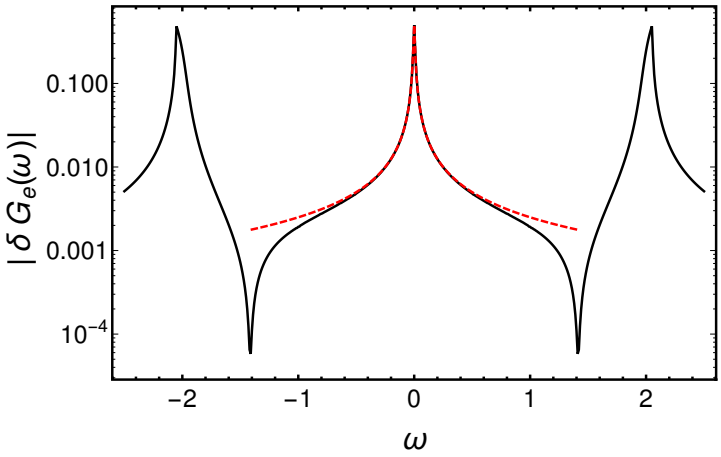

Figure 6.7: *Plot of* $|\delta_1 G_\mathrm{e}(\omega)|$ *for a cosine dispersion relation* $\epsilon(k) = -2\cos(k)$ *and* $U_\mathrm{dis} = 0.1$ *on a log scale (black). The peak at* $\omega = 0$ *is also visible for a linear dispersion relation (red dashed) (cf. Eq.* (6.32)*), but the peaks at* $\omega \sim \pm 2$ *stem from the enhanced localization probability at the band edge.*

photon would then perform a loop along the impurities which starts and ends at the TLS, and the second photon would travel along this path in time-reversed order[9].

In contrast to the DOS renormalization effects, which are presented in the previous section and are most prominent at the band edges, the disorder diagram above gives also corrections when the energy is far away from the band edge. For a linear dispersion relation this diagram evaluates to

$$\begin{aligned}\Delta_1 G_\mathrm{e}^\mathrm{lin}(\omega) &= [{}_1G_\mathrm{e}(\omega)]^3 U_\mathrm{at}^4 U_\mathrm{dis}^2 \sum_{\mu_1\ldots\mu_4} \int \frac{\mathrm{d}k}{2\pi}\frac{\mathrm{d}p}{2\pi}\frac{\mathrm{d}q}{2\pi} G_\mathrm{w}^{\mu_1}(k) G_\mathrm{w}^{\mu_2}(k-q) G_\mathrm{w}^{\mu_3}(p-q) G_\mathrm{w}^{\mu_4}(p) \\ &= i[{}_1G_\mathrm{e}(\omega)]^3 \frac{U_\mathrm{at}^4}{v^2} \frac{1/\left(2\tau_\mathrm{dis}\right)}{\omega + i/\tau_\mathrm{dis}}, \end{aligned} \tag{6.32}$$

where $\tau_\mathrm{dis} = v/U_\mathrm{dis}^2$ is the mean disorder scattering time and ${}_1G_\mathrm{w}^\mu(k) = \left(\omega - \mu v k + i/\tau_\mathrm{dis}\right)^{-1}$ is the disorder-renormalized photon Green's function (the brackets denoting the disorder average have been omitted for a shorter notation).

We can see that Eq. (6.32) exhibits two poles: One stems from the TLS-Green's functions ${}_1G_\mathrm{e}(\omega)$ and describes the spontaneous decay (with the associated timescale τ_sd), the other one stems from the disorder-induced momentum integration. In the clean case there is only one pole, which renders the decay purely exponential and thus Markovian. However, Fourier transforming the above equation gives a result of the form $\Delta_1 G_\mathrm{e}^\mathrm{lin} \sim e^{-t/\tau_\mathrm{sd}} + \eta e^{-t/\tau_\mathrm{dis}}$, where η is some prefactor. This result shows clearly that disorder breaks Markovianity: The exponential decay of the clean system is superimposed by another timescale, induced by disorder. From a

[9] The mechanism may be similar to that of weak localization, but in the present case there is no interference between the two paths, which would be crucial for the effect of weak localization [118].

physical point of view, the non-Markovian effect of disorder becomes clear by looking again at Eq. (6.31). A photon with momentum k scatters on an impurity, which stores the momentum $2k$. At a later time, another photon scatters on the impurity and collects the momentum. In this way, the impurity acts as a memory kernel and provides the second photon with additional information about the past. This is also valid for higher-order terms, where the photon scatters on multiple impurities and visits them again later in time-reversed order.

In the case of a nonlinear band structure we expect that the qualitative behavior stays the same, because the photon is still able to perform loops along the impurities. We have numerically evaluated Eq. (6.32) for a cosine dispersion relation and plotted

$$\delta_1 G_\mathrm{e}(\omega) = \Delta_1 G_\mathrm{e}(\omega)/\Delta_1 G_\mathrm{e}(\omega)|_\mathrm{nh}, \tag{6.33}$$

in Fig. 6.7. Here, $\Delta_1 G_\mathrm{e}(\omega)|_\mathrm{nh}$ corresponds to the diagram in Eq. (6.31) without the disorder hat. The peak at $\omega = 0$ corresponds to

$$\delta_1 G_\mathrm{e}^\mathrm{lin}(\omega) = \frac{1/\left(2\tau_\mathrm{dis}\right)}{\omega + i/\tau_\mathrm{dis}}, \tag{6.34}$$

which is derived with the help of Eq. (6.32) for the linear dispersion relation. Additionally, we observe two peaks at the band edges. These peaks stem from the enhanced localization probability at the band edge, which leads to strong contributions from all disorder diagrams. Hence, the dressing diagrams also contribute to the discrepancy between the Green's function approach and the diagonalized discrete waveguide in Fig. 6.5.

6.5 Conclusion

We have calculated here the influence of disorder in the waveguide on the decay properties of the TLS. As a first approximation we coupled the TLS to an already disorder-averaged waveguide, where the dominant contribution stems from the disorder-induced smearing of the DOS. For a linear dispersion relation this has no effect, since the DOS is already flat, but for a cosine dispersion relation this leads to a breakdown of the atom-photon bound state for sufficiently strong disorder. This result is supported by numerical calculations on a disordered tight-binding chain. Moreover, we found that the numeric and analytic calculations give quantitatively different results, which we address to the partial summation of disorder diagrams in the Green's function. On top of that, we have identified a class of Feynman diagrams in the perturbation series which are unique to this system and give rise to effects beyond the coupling to a waveguide with a smeared out DOS. In these diagrams, the photon performs a loop along impurities in the vicinity of the TLS, which is performed a second time by another photon. These loops act as memory kernel and lead to non-Markovian behavior.

7 SUMMARY, CONCLUSION & OUTLOOK

In this chapter we summarize of the results presented in this thesis. Furthermore, we give a conclusion and discuss possible future applications.

7.1 Summary

The goal of this thesis was to present and analyze a new theoretical framework for waveguide QED based on quantum-field theoretical Green's functions and to study its applications in disordered systems.

To this end, we introduced the fundamental concepts of quantum field theory in Chapter 1. We focused on the derivation of Green's functions in the presence of interaction. Supported by Feynman diagrams, we eventually obtained a self-consistent Dyson equation for the full Green's function and introduced the concept of the self-energy.

Chapter 2 was devoted to the derivation of the physical model used throughout this thesis. Starting from Maxwell's equations, we quantized the electromagnetic field and discussed its interaction with a single atom. With the help of these results we were able to construct the waveguide QED Hamiltonian Eq. (2.60), which was used in this thesis. Furthermore, we discussed several experimental realizations, ranging from the microwave regime to optical wavelengths.

In Chapter 3 we introduced our framework for waveguide QED. We derived the full Green's functions in the single- and two-excitation sectors for an arbitrary dispersion relation, together with their Feynman diagram representation. In the single-excitation sector we found analytical expressions for the Green's function and extracted the spectral density as well as the scattering matrix. The Green's function in the two-excitation sector was defined in terms of a self-consistent T-Matrix equation. Due to its complexity we evaluated the T-matrix numerically for a cosine dispersion relation and identified a Fano resonance in the spectral density between the excited, renormalized TLS and the additional photon in the waveguide. Furthermore, we found an exact solution for the Green's function for a linear dispersion relation, where the perturbation series breaks down after the second order. We were thus able to derive the spectral density and the scattering matrix analytically and compared these results with previous works.

In Chapter 4 we investigated the effects of a nonlinear dispersion relation on the Green's function in the two-excitation sector. We focused on two regimes. In the first regime we assumed that the energy is far away from band edges and slow-light regimes, but the dispersion relation has a small but non-zero curvature γ as compared to the group velocity v. A perturbative calculation in the small parameter γ/v yielded that additional terms in the perturbation series of the Green's function are still strongly suppressed and that the dominant effects are renormalizations in the result for a linear dispersion relation due to the band curvature. In the second regime we focused on energies in the vicinity of the band edge. We analyzed the additional terms in the perturbation series on a phenomenological level and identified that these terms include the effect of interaction-induced radiation trapping (IIRT). Hence, we were able to assign each term in the perturbation series of the Green's function a physical effect.

Chapter 5 was devoted to the dynamics of the system when subjected to one- and two-photon Gaussian wavepackets. With the help of the Green's functions in space-time domain we calculated analytic expressions for the propagated wavefunction in both sectors. We found that the scattering behavior can be described by the ratio of the pulsewidth σ and the spontaneous emission time τ. Depending on this ratio, the photons are either very weakly interacting with the TLS, maximally exciting it or strongly reflected in the single-photon case and strongly correlated for more than one photon. These results are supported by numerical calculations on a tight-binding chain, where we also observe a dependence of IIRT on this ratio.

Finally, we examined the influence of disorder in the waveguide on the decay properties of the TLS in Chapter 6. We started with a simple approximation and coupled the TLS to an already disorder-averaged waveguide. Here, the dominant effect is a disorder-induced smearing of the DOS. This has no effect on the disorder-averaged TLS-Green's function for a linear dispersion relation, but leads to the breakdown of the atom-photon bound state at a critical disorder strength. Again, we supported our results with numeric calculations on a tight-binding chain. These calculations confirmed the breakdown of the atom-photon bound state, but yielded a different critical disorder strength. This discrepancy was attributed to the approximations made in the derivation of the disorder-averaged TLS-Green's function. Furthermore, we identified a special class of diagrams unique to the setup of waveguide QED. In these diagrams the photons perform loops along single impurities, giving rise to memory effects. Thus, these diagrams induce non-Markovian behavior, generating finite contributions even for a linear dispersion relation.

7.2 Conclusion & Outlook

To conclude, we presented in this thesis a powerful and versatile theoretical framework for waveguide QED, which provides Green's function in the single- and two-excitation sector for an arbitrary dispersion relation. In addition, the Feynman diagram representation enabled us to identify the underlying physical processes. The Green's functions can either be presented in frequency-momentum or space-time domain and thus offer themselves for a number of possible extensions.

A straightforward extension of this framework would e.g. include more difficult quantum emitters, like three- or four-level systems, or higher excitation numbers. One could also imagine

to include quantum emitters which couple to right- and leftmoving photons differently. Such a setup is realized for example in cold atoms systems coupled to a tapered fiber, where directed emission is observed [125]. Alternatively, multiple TLS coupled to the waveguide promise fascinating physics. The case of two TLS is currently investigated by T. Sproll by means of the framework presented in this thesis. The setup shows fascinating features like, e.g., near-field, Förster-like excitation transfer and bound states in the continuum [90, 126].

We already presented an extension of the framework in this thesis, i.e. the inclusion of disorder. This part can be further developed, e.g., by going to the two-excitation sector or by combining the abovementioned straightforward extensions with a disordered waveguide. Other approaches to make the model more realistic could include dissipation by coupling the TLS to an external bath, or to go beyond the RWA.

These are just some of the possible extensions of the framework. Green's functions have been used a long time in the theory of condensed matter systems, where they found numerous applications. We are confident that the work presented in this thesis can also have a great value for the community, bringing waveguide QED a step closer to applications in quantum technologies.

A APPEARANCE OF EQUAL-TIME GREEN'S FUNCTIONS

Our discussion will focus on an example diagram of the perturbation series, which is given by

$$g(t_f - t_i) = \quad , \tag{A.1}$$

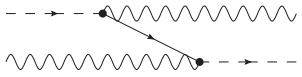

with the goal to derive the equal-time Greens's functions from a more "standard" diagrammatic approach [16]. Note that this appendix is not rigorous but intends to give the reader insight about the emergence of the equal-time Green's functions.

From a direct diagrammatic derivation, the diagram is given in time domain by

$$g(k,k';t_f - t_i) = iU^2 \int \mathrm{d}t\mathrm{d}t' g_{\mathrm{e}}(t - t_i) g_{\mathrm{ph}}(k, t' - t_i) g_{\mathrm{g}}(t' - t) g_{\mathrm{ph}}(k', t_f - t) g_{\mathrm{e}}(t_f - t'), \tag{A.2}$$

where the free Green's functions are

$$g_{\mathrm{e}}(t) = e^{-i\Omega t/2}, \quad g_{\mathrm{g}}(t) = e^{i\Omega t/2}, \quad g_{\mathrm{ph}}(k,t) = e^{-i\epsilon(k)t}, \tag{A.3}$$

the corresponding Feynman diagrams are given in Tab. 3.1 and the time integrations stem from the interaction vertices. The crucial point about these Green's functions is that they can be rewritten in the form

$$\begin{aligned} g_{\mathrm{ph}}(k, t_f - t_i) &= e^{-i\epsilon(k)(t_f - t_i)} \\ &= e^{-i\epsilon(k)(t_f - t)} e^{-i\epsilon(k)(t - t_i)} \\ &= g_{\mathrm{ph}}(k, t_f - t) g_{\mathrm{ph}}(k, t - t_i). \end{aligned} \tag{A.4}$$

In this way Eq. (A.2) can be rewritten as

$$\begin{aligned} g(k,k';t_f - t_i) = iU^2 \int \mathrm{d}t\mathrm{d}t' & \Big[g_{\mathrm{e}}(t - t_i) g_{\mathrm{ph}}(k, t - t_i) \Big] \\ & \times \Big[g_{\mathrm{g}}(t' - t) g_{\mathrm{ph}}(k, t' - t) g_{\mathrm{ph}}(k', t' - t) \Big] \\ & \times \Big[g_{\mathrm{e}}(t_f - t') g_{\mathrm{ph}}(k', t_f - t') \Big], \end{aligned} \tag{A.5}$$

where each bracket contains an equal-time Green's function. Fourier transforming this expression to frequency domain yields

$$g(k,k';\omega) = U^2 \frac{1}{\omega - \Omega/2 - \epsilon(k) + i0} \frac{1}{\omega + \Omega/2 - \epsilon(k) - \epsilon(k') + i0} \frac{1}{\omega - \Omega/2 - \epsilon(k') + i0}$$

$$= \quad , \tag{A.6}$$

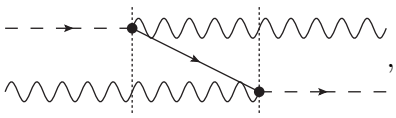

which is exactly the second term in Eq. (3.22) without bubble-like self-energy corrections.

B CALCULATION OF THE TWO-EXCITATION S-MATRIX

In this Appendix, we provide the details of the calculation of the two-excitation scattering matrix for the case of a linear dispersion relation. The two-excitation S-Matrix is given by Eqs. (3.58) and (3.60). With the help of Eqs. (3.29) and (3.56), we can write this S-Matrix as

$$S_{k_i p_i, k_f p_f} = S^0_{k_i p_i, k_f p_f} + S^1_{k_i p_i, k_f p_f} + S^2_{k_i p_i, k_f p_f}, \tag{B.1}$$

$$S^0_{k_i p_i, k_f p_f} = \delta_{k_i, k_f}\delta_{p_i, p_f} + \delta_{p_i, k_f}\delta_{k_i, p_f}, \tag{B.2}$$

$$S^1_{k_i p_i, k_f p_f} = -i\delta(E)U^2\Big({}_2G_{\mathrm{e,r}}(k_i;\omega)\delta_{k_i,k_f} + \{\mathrm{perm}\}\Big)\Big|_{os}, \tag{B.3}$$

$$S^2_{k_i p_i, k_f p_f} = -i\delta(E)\frac{U^4}{2\pi}\Big({}_2G_{\mathrm{e,r}}(k_i)\,{}_2G_{\mathrm{w},0}(k_i,k_f)\,{}_2G_{\mathrm{e,r}}(k_f) + \{\mathrm{perm}\}\Big)\Big|_{os}, \tag{B.4}$$

where {perm} represents terms where the momenta have been permuted according to Eq. (3.29) and

$$\delta(E) = \delta(\epsilon(k_i) + \epsilon(p_i) - \epsilon(k_f) - \epsilon(p_f)). \tag{B.5}$$

Furthermore, we suppress the chirality indices, thus (initially) treating all (incoming and outgoing) photons as right-movers. The case of different chiralities will be discussed at the end of this appendix.

In order to calculate $S^1_{k_i p_i, k_f p_f}$, we rewrite the δ-function according to

$$\delta(\epsilon(k_i) + \epsilon(p_i) - \epsilon(k_f) - \epsilon(p_f)) = \frac{\delta_{k_i+p_i, k_f+p_f}}{v}. \tag{B.6}$$

Bearing in mind that we have shifted $\omega \to \omega - \Omega/2$, using Eq. (3.24), and setting $\omega = vk_i + vp_i$, we find after cumbersome but straightforward calculation

$$\begin{aligned} S^1_{k_i p_i, k_f p_f} &= \delta_{p_i, p_f}\delta_{k_i, k_f}\frac{-iU^2/v}{vp_i - \Omega + iU^2/v} + \{\mathrm{perm}\} \\ &= r_{k_i}\left(\delta_{p_i,p_f}\delta_{k_i,k_f} + \delta_{p_i,k_f}\delta_{k_i,p_f}\right) + r_{p_i}\left(\delta_{p_i,p_f}\delta_{k_i,k_f} + \delta_{p_i,k_f}\delta_{k_i,p_f}\right). \end{aligned} \tag{B.7}$$

Here, r_k is the single-excitation reflection amplitude as specified in Eq. (3.50).

In very much the same manner, we find

$$S^2_{k_i p_i, k_f p_f} = \delta_{k_i+p_i, k_f+p_f} \frac{-iU^4}{2\pi v} \frac{1}{vk_i - \Omega + iU^2/v} \frac{1}{vk_f - vp_i + i0} \frac{1}{vp_f - \Omega + iU^2/v} + \{\text{perm}\}. \tag{B.8}$$

Upon replacing the inner free Green's function by an application of the Dirac identity

$$\frac{1}{x + i0} = \mathcal{P}\left(\frac{1}{x}\right) - i\pi\delta(x), \tag{B.9}$$

the scattering matrix decomposes into two terms

$$S^2_{k_i p_i, k_f p_f} = S^{2,\text{P.V.}}_{k_i p_i, k_f p_f} + S^{2,\delta}_{k_i p_i, k_f p_f}, \tag{B.10}$$

where the term that results from the δ-function in the Dirac identity, $S^{2,\delta}_{k_i p_i, k_f p_f}$, reduces to

$$\begin{aligned} S^{2,\delta}_{k_i p_i, k_f p_f} =& \frac{1}{2}\delta_{p_i,p_f}\delta_{k_i,k_f} \frac{-iU^2/v}{vk_i - \Omega + iU^2/v} \frac{-iU^2/v}{vp_f - \Omega + iU^2/v} + \{\text{perm}\} \\ =& r_{k_1} r_{p_1} \left(\delta_{p_1,p_2}\delta_{k_1,k_2} + \delta_{k_1,p_2}\delta_{p_1,k_2}\right). \end{aligned} \tag{B.11}$$

The term of the scattering matrix that originates from the principal value in the Dirac identity is given by

$$\begin{aligned} S^{2,\text{P.V.}}_{k_i p_i, k_f p_f} =& \frac{i}{2\pi}\delta_{k_i+p_i, k_f+p_f} r_{k_i} r_{p_f} \mathcal{P}\frac{1}{k_i - k_f} + \{\text{perm}\} \\ =& \frac{i}{2\pi}\delta_{k_i+p_i, k_f+p_f} \left[\mathcal{P}\frac{1}{k_i - k_f}\left(r_{k_i} r_{p_f} - r_{p_i} r_{k_f}\right) + \mathcal{P}\frac{1}{k_i - p_f}\left(r_{k_i} r_{k_f} - r_{p_i} r_{p_f}\right)\right]. \end{aligned} \tag{B.12}$$

Here, we have used energy conservation to make certain simplifications. Using energy conservation once again, we find

$$\begin{aligned} r_{k_i} r_{p_f} - r_{p_i} r_{k_f} =& \frac{U^4}{v} \frac{(k_i - k_f)\left(E - 2\Omega + iU^2/v\right)}{(vp_i - \Omega + iU^2/v)(vk_i - \Omega + iU^2/v)} \\ & \times \frac{1}{(vp_f - \Omega + iU^2/v)(vk_f - \Omega + iU^2/v)} \end{aligned} \tag{B.13}$$

and the same expression with interchanged momenta, $k_f \leftrightarrow p_f$, for $r_{k_i} r_{k_f} - r_{p_i} r_{p_f}$. Exploiting the fact that

$$\left(k_i - k_f\right)\mathcal{P}\frac{1}{k_i - k_f} = 1 \tag{B.14}$$

(which is, strictly speaking, only valid when $k_i \neq k_f$) and combining the above expressions, we find

$$\begin{aligned} S^{2,\text{P.V.}}_{k_i p_i, k_f p_f} = \frac{iU^4}{\pi v}\delta_{k_i+p_i, k_f+p_f} & \frac{\left(k_i + p_i - 2\Omega + iU^2/v\right)}{(vp_i - \Omega + iU^2/v)(vk_i - \Omega + iU^2/v)} \\ & \times \frac{1}{(vp_f - \Omega + iU^2/v)(vk_f - \Omega + iU^2/v)}. \end{aligned} \tag{B.15}$$

Upon inserting Eq. (B.2), (B.7), and (B.11) in (B.1), we finally find

$$S^{RR,RR}_{k_i p_i, k_f p_f} = t_{k_i} t_{p_i} \left(\delta_{k_i,k_f} \delta_{p_i,p_f} + \delta_{k_i,p_f} \delta_{p_i,k_f} \right) + S^{2,\text{P.V.}}_{k_i p_i, k_f p_f}, \tag{B.16}$$

where $t_k = 1 + r_k$. As a matter of fact, the above expression is exactly the scattering matrix given in Ref. [52].

We now turn to the effects of chirality. Firstly, the momenta are renormalized $k \to \mu k$, which controls the sign of the momenta. Secondly, chirality is conserved upon free propagation, which adds two chirality-conserving δ-functions to $S^0_{k_i p_i, k_f p_f}$ and one to $S^1_{k_i p_i, k_f p_f}$. Combining all the relevant expressions, the S-matrix in the other chirality sectors yields

- $k_i^R p_i^R \to k_f^R p_f^L$

$$S^{RR,RL}_{k_i p_i, k_f p_f} = t_{k_i} r_{p_i} \delta_{k_i,k_f} \delta_{p_i,-p_f} + r_{k_i} t_{p_i} \delta_{k_i,-p_f} \delta_{p_i,k_f} + S^{2,\text{P.V.}}_{k_i p_i, k_f p_f}, \tag{B.17}$$

- $k_i^R p_i^R \to k_f^L p_f^L$

$$S^{RR,LL}_{k_i p_i, k_f p_f} = r_{k_i} r_{p_i} \left(\delta_{k_i,-k_f} \delta_{p_i,-p_f} + \delta_{k_i,-p_f} \delta_{p_i,-k_f} \right) + S^{2,\text{P.V.}}_{k_i p_i, k_f p_f}, \tag{B.18}$$

where the superscripts of k_j^μ indicate the values of chirality.

C CALCULATION OF $I_{\mathrm{T}}(k_i, k_f; \omega)$ IN THE QUASI-LINEAR REGIME

In this appendix we present the detailed calculation of $I_{\mathrm{T}}(k_i, k_f; \omega)$ in the quasi-linear regime. Iterating Eq. (3.27) and inserting it into Eq. (4.3) restores the perturbation series

$$I_{\mathrm{T}}(k_i, k_f; \omega) = \sum_i I_{\mathrm{T}}^{(i)}(k_i, k_f; \omega). \tag{C.1}$$

We focus mainly on the calculation of

$$\begin{aligned} I_{\mathrm{T}}^{(1)}(k_i, k_f; \omega) &= \int \frac{\mathrm{d}k}{2\pi} {}_2G_w^0(k_i, k; \omega) {}_2G_{\mathrm{e,r}}(k; \omega) {}_2G_w^0(k, k_f; \omega) \\ &= \int \frac{\mathrm{d}k}{2\pi} \mathcal{I}_{\mathrm{T}}^{(1)}(k_i, k_f, k; \omega). \end{aligned} \tag{C.2}$$

and turn to the higher order processes at the end of this section. The definitions of ${}_2G_w^0(k_f, k_i; \omega)$ and ${}_2G_{\mathrm{e,r}}(k; \omega)$ are given in Eq. (3.23) and (3.24), respectively, where the self-energy in ${}_2G_{\mathrm{e,r}}(k; \omega)$ is

$${}_2\Sigma(k) = -i\frac{U^2}{v} \frac{1}{\sqrt{1 + 4\frac{\gamma}{v}\frac{\omega - \epsilon(k)}{v}}}. \tag{C.3}$$

As discussed in Chapter 4, we assume that all energies which appear in Eq. (C.2), that is $\epsilon(k_i)$, $\epsilon(k_f)$, Ω and ω, lie within the quasi-linear energy range defined by Eq. (4.10). We furthermore assume that sums of these energies still fulfill Eq. (4.10).

We start by analyzing the analytic structure of the integrand of Eq. (C.2). The two free waveguide Green's functions exhibit two poles each, located at

$$k_\pm = \frac{-1 \pm \sqrt{1 + 4\frac{\gamma}{v}\frac{\tilde{\omega}}{v}}}{2\gamma/v}, \tag{C.4}$$

where $\tilde{\omega} = \omega - \epsilon(k_{i/f}) + i0$. Since sums of these energies fulfill Eq. (4.10), the two poles are always well-separated ($4\frac{\gamma\tilde{\omega}}{v^2} \gg -1$). In the limit $\gamma \to 0$, $k_+ = \tilde{\omega}/v$ is the physical pole, whereas $k_- \to -\infty$ is unphysical.

The analytic structure of the TLS-Green's function is more complicated: The self-energy shifts the poles in a nontrivial way and induces additional branch cuts when

$$\omega - \epsilon(k) < -\frac{1}{4}\frac{v}{\gamma}v. \tag{C.5}$$

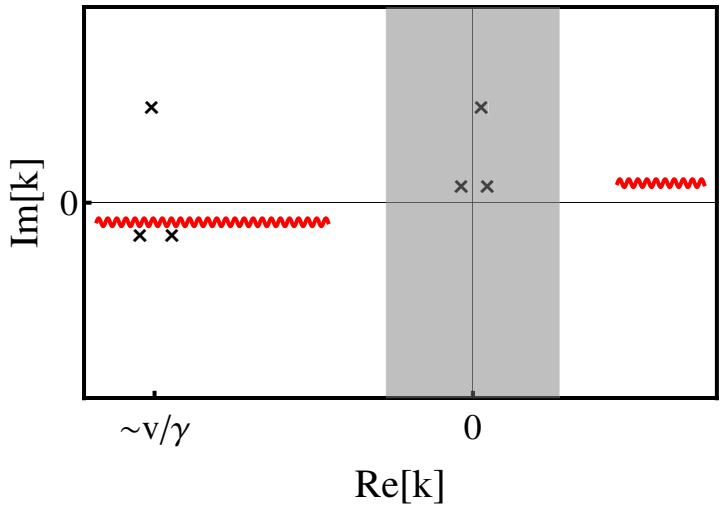

Figure C.1: *Analytic structure of the integrand of Eq.* (C.2)*, where the crosses denote poles and the red lines indicate branch cuts. The poles near the real axis stem from the free waveguide Green's functions, the ones shifted to the upper complex plane from the renormalized TLS-Green's function. The only phyisically relevant poles are the ones near* $Re[k] = 0$*. The ones near* $Re[k] = -v/\gamma$ *and the branch cuts are artifacts stemming from the nonlinearity of the dispersion relation.*

This relation is valid when k is of order v/γ, which is far away from the quasi-linear regime. With the help of Eq. (4.10), we find that in the quasi-linear regime

$$\left| 4\frac{\gamma}{v}\frac{\omega - \epsilon(k)}{v} \right| \ll 4\frac{\gamma}{v}\frac{v}{4\gamma} = 1, \tag{C.6}$$

which means that the self-energy can be approximated as

$$\Sigma(k) \simeq -i\frac{U^2}{v}\left(1 - 2\frac{\gamma}{v}\frac{\omega - \epsilon(k)}{v}\right). \tag{C.7}$$

Using this self-energy we are able to calculate the poles of the TLS-Green's function, which are given by

$$k_{\pm}^{\mathrm{TLS}} = i\frac{U^2}{v^2} - \frac{v}{2\gamma}\left(1 \mp \sqrt{1 + \frac{4\gamma}{v}\frac{\omega - \Omega}{v} - 4\frac{\gamma^2}{v^2}\left(\frac{U^4}{v^4} + \frac{2iU^2\omega}{v^3}\right)}\right). \tag{C.8}$$

Here, k_{+}^{TLS} is the physical pole, going to $k_{+}^{\mathrm{TLS}} \to iU^2/v^2 + (\omega - \Omega)/v$ in the limit of $\gamma/v \to 0$, whereas k_{-}^{TLS} goes with $-v/\gamma \to -\infty$.

The analytic structure of the integrand is summarized in Fig. C.1, where the poles near $\mathrm{Re}[k] = 0$ are the phyisical poles and the ones near $\mathrm{Re}[k] = -v/\gamma$ are the unphysical ones. The

poles of the free waveguide Green's functions are located near $\mathrm{Im}[k] = 0$, whereas the poles of the TLS-Green's function are shifted to the complex plane - notably both to the upper half plane. The branch cuts are indicated by the red wiggly lines and the grey area denotes the quasi-linear region of the dispersion relation.

The actual integration is performed as follows: Since the dispersion relation only makes sense in the quasi-linear regime given by Eq. (4.9), the integration in Eq. (C.2) should only be performed in this region (i.e. the grey shaded region in Fig. C.1). At the borders of the quasi-linear regime, the integrand is suppressed with $\left(\gamma/v\right)^3$, which allows us to expand the integration borders to infinity again, neglecting the effects of the additional (unphysical) poles and branch cuts. The integral can then be computed by closing the contour in the upper half plane and collecting only the physical poles,

$$I_{\mathrm{T}}^{(1)}(k_i, k_f; \omega) = i \sum_n \mathrm{Res}[\mathcal{I}_{\mathrm{T}}^{(1)}(k_i, k_f, k; \omega), k_n], \tag{C.9}$$

where $\mathrm{Res}[\mathcal{I}_{\mathrm{T}}^{(1)}(k_i, k_f, k; \omega), k_n]$ is the residue of the integrand $\mathcal{I}_{\mathrm{T}}^{(1)}(k_i, k_f, k; \omega)$ at $k = k_n$ and k_n are the physical poles. Expanding the integral up to first order in γ/v yields

$$I_{\mathrm{T}}^{(1)}(k_i, k_f; \omega) = 0 + \mathcal{O}\left(\frac{\gamma}{v}\right)^2, \tag{C.10}$$

which means that the influence of a small band curvature can be neglected in first order.

The calculation up to now only considered $I_{\mathrm{T}}^{(1)}(k_i, k_f; \omega)$, which was the first term when inserting Eq. (3.27) into $I_{\mathrm{T}}(k_i, k_f; \omega)$. The second term has the form

$$I_{\mathrm{T}}^{(2)}(k_i, k_f; \omega) = \int \frac{\mathrm{d}k}{2\pi} \frac{\mathrm{d}p}{2\pi} \mathcal{I}_{\mathrm{T}}^{(1)}(k_i, p, k; \omega) {}_2G_{\mathrm{e,r}}(p; \omega) {}_2G_{\mathrm{w}}^0(p, k_f; \omega), \tag{C.11}$$

where, in analogy to the previous calculation, the momenta are restricted to the quasi-linear regime. This means that the k-integration can be performed in the way depicted above, which means that without performing the p-integration, $I_{\mathrm{T}}^{(2)}(k_i, k_f; \omega)$ is of order $\mathcal{O}\left(\gamma/v\right)^2$. The same argument holds for all higher order integrals, which means that

$$I_{\mathrm{T}}(k_i, k_f; \omega) = 0 + \mathcal{O}\left(\frac{\gamma}{v}\right)^2. \tag{C.12}$$

D PROPAGATED WAVEFUNCTION IN THE SINGLE-EXCITATION SECTOR

In this appendix we present the propagated wavefunctions together with the corresponding Green's functions in the single-excitation sector, where the initial wavefunction is given by Eq. (5.11). For this initial wavefunction, the propagated one is given by

$$|{}_1\Psi(x',t)\rangle = \begin{pmatrix} {}_1\Psi_{\mathrm{e}}(t) \\ {}_1\Psi_{\mathrm{R}}(x',t) \\ {}_1\Psi_{\mathrm{L}}(x',t) \end{pmatrix} = \int \mathrm{d}x \begin{pmatrix} {}_1G_{\mathrm{Re}}(x;t)g_{\mathbf{p}}(x) \\ {}_1G_{\mathrm{RR}}(x',x;t)g_{\mathbf{p}}(x) \\ {}_1G_{\mathrm{RL}}(x',x;t)g_{\mathbf{p}}(x) \end{pmatrix}. \tag{D.1}$$

The waveguide Green's function with the initial and final chiralities μ_i and μ_f is given by (cf. Sec. 3.2.1)

$${}_1G_{\mu_i\mu_f}(x_f,x_i;t) = {}_1G^{(1)}_{\mu_i\mu_f}(x_f,x_i;t) + {}_1G^{(2)}_{\mu_i\mu_f}(x_f,x_i;t), \tag{D.2}$$

where

$${}_1G^{(1)}_{\mu_i\mu_f}(x_f,x_i;t) = -i\Theta(x_f-x_i)\delta_{\mu_i,\mu_f}\delta\left(x_f-x_i-vt\right), \tag{D.3}$$

$${}_1G^{(2)}_{\mu_i\mu_f}(x_f,x_i;t) = (-i)^3\left(\frac{U}{v}\right)^2\Theta(-x_i)\Theta(x_f)\Theta(vt-(x_f-x_i))e^{-\left(i\frac{\Omega}{v}+\frac{U^2}{v^2}\right)\left(vt-(x_f-x_i)\right)}. \tag{D.4}$$

Here, we have absorbed the chirality into the according coordinates $\mu_i x_i \to x_i$ for brevity. The remaining Green's function, which describes the absorption of a photon, is given by

$${}_1G_{\mu_i\mathrm{e}}(x_i;t) = -\frac{U}{v}\Theta(-x_i)\Theta(x_i+vt)e^{-\left(i\frac{\Omega}{v}+\frac{U^2}{v^2}\right)(x_i+vt)}. \tag{D.5}$$

Inserting these Green's functions into Eq. (D.1) and performing the integrations yields

$${}_1\Psi_{\mu}(x,t) = {}_1\Psi^{(1)}_{\mu}(x,t) + {}_1\Psi^{(2)}_{\mu}(x,t) \tag{D.6}$$

with

$${}_1\Psi^{(1)}_{\mu}(x,t) = -i\Theta(vt)g_{\mathbf{p}}(x-vt)\delta_{R,\mu}, \tag{D.7}$$

$$\begin{aligned} {}_1\Psi^{(2)}_{\mu}(x,t) =& \frac{(-i)^3\pi^{\frac{1}{4}}\sqrt{2\sigma}}{2}\left(\frac{U}{v}\right)^2\Theta(x)\Theta(vt-x) \\ &\times e^{-\left(i\frac{\Omega}{v}+\frac{U^2}{v^2}\right)(vt-x)}e^{\bar{x}^2-\frac{x_0^2}{2\sigma^2}}\mathrm{Erf}\left[\frac{x-vt}{\sqrt{2}\sigma}-\bar{x},-\bar{x}\right], \end{aligned} \tag{D.8}$$

and

$$ {}_1\Psi_{\mathrm{e}}(t) = -\pi^{\frac{1}{4}}\sqrt{2\sigma}\frac{U}{2v}e^{-\left(i\Omega+\frac{U^2}{v}\right)t}e^{\bar{x}^2-\frac{x_0^2}{2\sigma^2}}\,\mathrm{Erf}\left[\frac{-vt}{\sqrt{2}\sigma}-\bar{x},-\bar{x}\right]. \tag{D.9} $$

The parameter $\bar{x}$ is defined as

$$ \bar{x} = \frac{1}{\sqrt{2}}\left(\frac{\mu_i x_0}{\sigma}-\sigma\left(\frac{U}{v}\right)^2+i\sigma\left(\mu_i k_0-\frac{\Omega}{v}\right)\right) \tag{D.10} $$

and $\mathrm{Erf}(x,y)$ is defined as

$$ \mathrm{Erf}(x,y) = \mathrm{Erf}(y)-\mathrm{Erf}(x), \tag{D.11} $$

where $\mathrm{Erf}(x)$ is the Error function,

$$ \mathrm{Erf}(x) = \frac{2}{\sqrt{\pi}}\int_0^x \mathrm{d}t e^{-t^2}. \tag{D.12} $$

E PROPAGATED WAVEFUNCTION IN THE TWO-EXCITATION SECTOR

In this appendix we present the propagated wavefunctions together with the corresponding Green's functions in the two-excitation sector, where the initial wavefunction is given by Eq. (5.12). For this initial wavefunction, the propagated one is given by

$$|{}_2\Psi(x',y';t)\rangle = \int \mathrm{d}x\mathrm{d}y \begin{pmatrix} \frac{1}{2}{}_2G_{\mathrm{RR,Re}}(x,y,x';t){}_2\Psi_{\mathrm{RR}}(x,y,0) \\ \frac{1}{\sqrt{2}}{}_2G_{\mathrm{RR,Le}}(x,y,x';t){}_2\Psi_{\mathrm{RR}}(x,y,0) \\ \frac{1}{2}{}_2G_{\mathrm{RR,RR}}(x,y,x',y';t){}_2\Psi_{\mathrm{RR}}(x,y,0) \\ \frac{1}{\sqrt{2}}{}_2G_{\mathrm{RR,RL}}(x,y,x',y';t){}_2\Psi_{\mathrm{RR}}(x,y,0) \\ \frac{1}{\sqrt{2}}{}_2G_{\mathrm{RR,LL}}(x,y,x',y';t){}_2\Psi_{\mathrm{RR}}(x,y,0) \end{pmatrix}, \tag{E.1}$$

where the prefactors stem from the normalization condition for the Green's function

$$\int \mathrm{d}x'\mathrm{d}y'{}_2\hat{G}(x,y,x',y';t){}_2\hat{G}^{\dagger}(\bar{x},\bar{y},x',y';t) = \frac{1}{2}\left(\delta(x-\bar{x})\delta(y-\bar{y}) + \delta(x-\bar{y})\delta(y-\bar{x})\right)\mathbb{1}. \tag{E.2}$$

The waveguide Green's function is given by

$$\begin{aligned} {}_2G_{\mu_i\nu_i,\mu_f\nu_f}(x_i,y_i,x_f,y_f;t) =& {}_2G^{(0)}_{\mu_i\nu_i,\mu_f\nu_f}(x_f-x_i,y_f-y_i;t) \\ &+ {}_2G^{(0)}_{\mu_i\nu_i,\nu_f\mu_f}(y_f-x_i,x_f-y_i;t) \\ &+ \left({}_2G^{(1)}_{\mu_i\nu_i,\mu_f\nu_f}(x_i,y_i,x_f,y_f;t) + \{\mathrm{sym}\}\right) \\ &+ \left({}_2G^{(2)}_{\mu_i\nu_i,\mu_f\nu_f}(x_i,y_i,x_f,y_f;t) + \{\mathrm{sym}\}\right), \end{aligned} \tag{E.3}$$

where x_i and y_i (x_f and y_f) are the initial (final) coordinates of the photons with the according chiralities μ_i and ν_i (μ_f and ν_f), $\{\mathrm{sym}\}$ represents a symmetrization of the coordinates (and the according chiralities) of the form

$$\{\mathrm{sym}\} = \{x_i \leftrightarrow y_i\} + \{x_f \leftrightarrow y_f\} + \{x_i \leftrightarrow y_i\}\{x_f \leftrightarrow y_f\}. \tag{E.4}$$

Just like in the single-excitation sector we absorb the chiralities into the corresponding coordinates $\mu_i x_i \to x_i$. The individual Green's functions are then given by

$${}_2G^{(0)}_{\mu_i\nu_i,\mu_f\nu_f}(x,y;t) = -i\Theta(x)\delta(x-vt)\delta(x-y)\delta_{\mu_i\mu_f}\delta_{\nu_i\nu_f}, \tag{E.5}$$

$$
\begin{aligned}
{}_2G^{(1)}_{\mu_i\nu_i,\mu_f\nu_f}(x_i,y_i,x_f,y_f;t) =& (-i)^3\left(\frac{U}{v}\right)^2\delta_{\nu_i\nu_f}\delta(y_f-y_i-vt)\Theta(x_f)\Theta(-x_i)\\
&\times\Theta\Big((y_f-y_i)-(x_f-x_i)\Big)\,e^{-\left(i\frac{\Omega}{v}+\frac{U^2}{v^2}\right)((y_f-y_i)-(x_f-x_i))},
\end{aligned}
\tag{E.6}
$$

$$
\begin{aligned}
{}_2G^{(2)}_{\mu_i\nu_i,\mu_f\nu_f}(x_i,y_i,x_f,y_f;t) =& (-i)^5\left(\frac{U}{v}\right)^4\Theta(y_f)\Theta(-x_i)\Theta(x_i-y_i)\Theta(x_f-y_f)\\
&\times e^{-\left(i\frac{\Omega}{v}+\frac{U^2}{v^2}\right)((x_i-y_i)+(x_f-y_f))}e^{-\left(2\frac{\Omega}{v}+\frac{U^2}{v^2}\right)(vt-(x_f-y_i))}\\
&\times\Big\{\Theta(vt-(x_f-y_i-\min(x_i-y_i,x_f-y_f)))\\
&\quad-\Theta(vt-(x_f-y_i))\Big\}.
\end{aligned}
\tag{E.7}
$$

The absorption Green's function is given by

$$
\begin{aligned}
{}_2G_{\mu_i\nu_i,\mu_f\mathrm{e}}(x_i,y_i,x_f;t) =& {}_2G^{(1)}_{\mu_i\nu_i,\mu_f\mathrm{e}}(x_i,y_i,x_f;t)+{}_2G^{(1)}_{\nu_i\mu_i,\mu_f\mathrm{e}}(y_i,x_i,x_f;t)\\
&+{}_2G^{(2)}_{\mu_i\nu_i,\mu_f\mathrm{e}}(x_i,y_i,x_f;t)+{}_2G^{(2)}_{\nu_i\mu_i,\mu_f\mathrm{e}}(y_i,x_i,x_f;t),
\end{aligned}
\tag{E.8}
$$

with

$$
\begin{aligned}
{}_2G^{(1)}_{\mu_i\nu_i,\mu_f\mathrm{e}}(x_i,y_i,x_f;t) =& (-i)^2\frac{U}{v}\delta_{\nu_i\mu_f}\delta(x_f-y_i-vt)\Theta(-x_i)\Theta\Big(x_f-(y_i-x_i)\Big)\\
&\times e^{-\left(i\frac{\Omega}{v}+\frac{U^2}{v^2}\right)(x_f-(y_i-x_i))},
\end{aligned}
\tag{E.9}
$$

$$
\begin{aligned}
{}_2G^{(2)}_{\mu_i\nu_i,\mu_f\mathrm{e}}(x_i,y_i,x_f;t) =& (-i)^4\left(\frac{U}{v}\right)^3\Theta(-x_i)\Theta(x_i-y_i)\Theta(x_f)\\
&\times e^{-\left(i\frac{\Omega}{v}+\frac{U^2}{v^2}\right)(x_i-y_i+x_f)}e^{-\left(2\frac{\Omega}{v}+\frac{U^2}{v^2}\right)(vt-(x_f-y_i))}\\
&\times\Big\{\Theta(vt-(x_f-y_i-\min(x_i-y_i,x_f)))\\
&\quad-\Theta(vt-(x_f-y_i))\Big\}.
\end{aligned}
\tag{E.10}
$$

Using Eq. (E.1) we are able to compute $|{}_2\Psi(x,y,t)\rangle$. However, the integrals containing Eqs. (E.7) and (E.10) are very difficult, since the Θ-functions couple the integration variables in a nontrivial way. This problem will be addressed in Sec. E.1 and it turns out that the two integrations decouple. Hence, the propagated wave function for two photons in the waveguide reads

$$
{}_2\Psi_{\mu\nu}(x,y,t)=\mathcal{N}\Big\{{}_2\Psi^{(0)}_{\mu\nu}(x,y,t)+{}_2\Psi^{(1)}_{\mu\nu}(x,y,t)+{}_2\Psi^{(2)}_{\mu\nu}(x,y,t)\Big\},
\tag{E.11}
$$

where the normalization constant is given by Eq. (5.13) and

$$ {}_2\Psi^{(0)}_{\mu\nu}(x,y,t) = -i\Theta(vt) g_{\mathbf{p}}(x-vt) g_{\mathbf{q}}(y-vt)\delta_{R\mu}\delta_{R\nu} + \{\mathbf{p}\leftrightarrow\mathbf{q}\}, \tag{E.12} $$

$$ \begin{aligned} {}_2\Psi^{(1)}_{\mu\nu}(x,y,t) =& \frac{(-i)^3\pi^{\frac{1}{4}}\sqrt{2\sigma_x}}{2}\left(\frac{U}{v}\right)^2 \delta_{R\nu}\Theta(x)\Theta(vt-x) g_{\mathbf{q}}(y,-vt) e^{-\left(i\frac{\Omega}{v}+\frac{U^2}{v^2}\right)(vt-x)} \\ & \times e^{\bar{x}^2-\frac{x_0^2}{2\sigma_x^2}} \mathrm{Erf}\left[\frac{x-vt}{\sqrt{2}\sigma_x} - \bar{x}, -\bar{x}\right] + \{\mathbf{p}\leftrightarrow\mathbf{q}\} + \{x\leftrightarrow y\} + \{\mathbf{p}\leftrightarrow\mathbf{q}\}\{x\leftrightarrow y\}, \end{aligned} \tag{E.13} $$

$$ \begin{aligned} {}_2\Psi^{(2)}_{\mu\nu}(x,y,t) =& \frac{(-i)^5\pi^{\frac{1}{2}}\sqrt{2\sigma_x}\sqrt{2\sigma_y}}{4}\left(\frac{U}{v}\right)^4 \Theta(y)\Theta(x-y)\Theta(vt-x) \\ & \times e^{-\left(i\frac{\Omega}{v}+\frac{U^2}{v^2}\right)(x-y)} e^{-\left(i2\frac{\Omega}{v}+2\frac{U^2}{v^2}\right)(vt-x)} \\ & \times e^{\bar{x}^2-\frac{x_0^2}{2\sigma_x^2}} \mathrm{Erf}\left[\frac{x-vt}{\sqrt{2}\sigma_x} - \bar{x}, -\bar{x}\right] e^{\bar{y}^2-\frac{y_0^2}{2\sigma_y^2}} \mathrm{Erf}\left[\frac{y-vt}{\sqrt{2}\sigma_y} - \bar{y}, \frac{x-vt}{\sqrt{2}\sigma_y} - \bar{y}\right] \\ & + \{\mathbf{p}\leftrightarrow\mathbf{q}\} + \{x\leftrightarrow y\} + \{\mathbf{p}\leftrightarrow\mathbf{q}\}\{x\leftrightarrow y\}. \end{aligned} \tag{E.14} $$

Here, $\mathbf{p}$ and $\mathbf{q}$ are again understood as superparameters, carrying all the information about the initial pulses. The propagated wavefunction where the TLS is in the excited state is given by

$$ {}_2\Psi_{\mu\mathrm{e}}(x,t) = \mathcal{N}\left\{ {}_2\Psi^{(1)}_{\mu\mathrm{e}}(x;t) + {}_2\Psi^{(2)}_{\mu\mathrm{e}}(x;t)\right\}, \tag{E.15} $$

where

$$ \begin{aligned} {}_2\Psi^{(1)}_{\mu\mathrm{e}}(x,t) =& \frac{(-i)^2\pi^{\frac{1}{4}}\sqrt{2\sigma_x}}{2}\frac{U}{v}\delta_{R\mu}\Theta(vt) g_{\mathbf{q}}(x-vt) e^{-\left(i\frac{\Omega}{v}+\frac{U^2}{v^2}\right)vt} \\ & \times e^{\bar{x}^2-\frac{x_0^2}{2\sigma_x^2}} \mathrm{Erf}\left[\frac{-vt}{\sqrt{2}\sigma_x} - \bar{x}, -\bar{x}\right] + \{\mathbf{p}\leftrightarrow\mathbf{q}\}, \end{aligned} \tag{E.16} $$

$$ \begin{aligned} {}_2\Psi^{(2)}_{\mu\mathrm{e}}(x,t) =& \frac{(-i)^4\pi^{\frac{1}{2}}\sqrt{2\sigma_x}\sqrt{2\sigma_y}}{4}\left(\frac{U}{v}\right)^3 \Theta(x)\Theta(vt-x) e^{-\left(i\frac{\Omega}{v}+\frac{U^2}{v^2}\right)x} e^{-\left(i2\frac{\Omega}{v}+2\frac{U^2}{v^2}\right)(vt-x)} \\ & \times e^{\bar{x}^2-\frac{x_0^2}{2\sigma_x^2}} \mathrm{Erf}\left[\frac{x-vt}{\sqrt{2}\sigma_x} - \bar{x}, -\bar{x}\right] e^{\bar{y}^2-\frac{y_0^2}{2\sigma_y^2}} \mathrm{Erf}\left[\frac{-vt}{\sqrt{2}\sigma_y} - \bar{y}, \frac{x-vt}{\sqrt{2}\sigma_y} - \bar{y}\right] \\ & + \{\mathbf{p}\leftrightarrow\mathbf{q}\}. \end{aligned} \tag{E.17} $$

E.1 Decoupling of the Θ-functions

In this section we consider the Θ-functions in Eq. (E.7). Similar ones are given in Eq. (E.10). The procedure shown in this appendix applies to these as well.

The Θ-functions considered here define the integral limits in Eq. (E.1). However, the Θ-functions in Eq. (E.7) contain the integral variables x_i and y_i in a nontrivial form, hence the integral limits are not clear. The Θ-functions appearing in Eq. (E.7) are

$$\begin{aligned}
&\Theta(-x_i)\Theta(x_i-y_i)\Theta(x_f)\Theta(x_f-y_f)\\
&\times\Big\{\Theta(vt-(x_f-y_i-\min(x_i-y_i,x_f-y_f)))-\Theta(vt-(x_f-y_i))\Big\}\\
=&\Theta(-x_i)\Theta(x_i-y_i)\Theta(x_f)\Theta(x_f-y_f)\\
&\times\Big\{\Theta((x_i-y_i)-(x_f-y_f))\Big[\Theta(vt-(y_f-y_i))-\Theta(vt-(x_f-y_i))\Big] \quad ①\\
&\quad+\Theta((x_f-y_f)-(x_i-y_i))\Big[\Theta(vt-(x_f-x_i))-\Theta(vt-(x_f-y_i))\Big]\Big\}. \quad ②
\end{aligned} \tag{E.18}$$

We now have a closer look at part ①,

$$\Theta(vt-(y_f-y_i))-\Theta(vt-(x_f-y_i))=\begin{cases}1, & x_f-vt>y_i>y_f-vt\\ -1, & y_f-vt>y_i>x_f-vt\\ 0, & \text{otherwise.}\end{cases} \tag{E.19}$$

Eq. (E.18) gives another constraint, $x_f > y_f$. This constraint is compatible with the first case

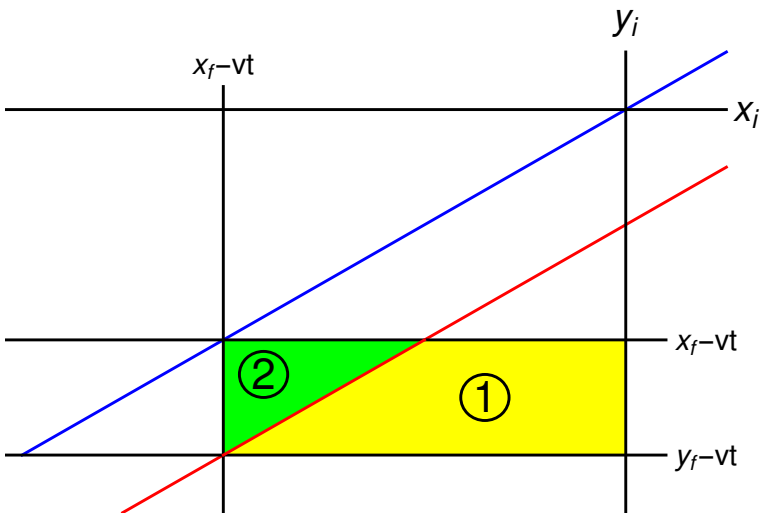

Figure E.1: *Visualization of the inequalities given by Eq.* (E.23) *in the x_i-y_i-plane. The blue line is at $y_i = x_i$ and the red one at $y_i = x_i-(x_f-y_f)$. The regions where all inequalities of (1) and (2) are fulfilled are yellow and green, respectively.*

of Eq. (E.19), but not with the second case. Hence, Eq. (E.19) reduces to the simple constraint

$$x_f - vt > y_i > y_f - vt. \tag{E.20}$$

A similar relation can be found for part ②,

$$\Theta(x_i - (x_f - vt)) - \Theta(y_i - (x_f - vt)) = \begin{cases} 1, & x_i > x_f - vt > y_i \\ -1, & y_i > x_f - vt > x_i \\ 0, & \text{otherwise.} \end{cases} \tag{E.21}$$

Again, we find another constraint in Eq. (E.18), $x_i > y_i$, which is compatible with the first case but incompatible with the second one. Thus, Eq. (E.21) reduces to

$$x_i > x_f - vt > y_i. \tag{E.22}$$

Combining Eq. (E.18), (E.19) and (E.21), we find the following constraints on the incoming space coordinates:

①	②
$x_i < 0$	$x_i < 0$
$x_i > y_i$	$x_i > y_i$
$y_i > y_f - vt$	$x_i > x_f - vt$
$x_f - vt > y_i$	$x_f - vt > y_i$
$x_i - (x_f - y_f) > y_i$	$y_i > x_i - (x_f - y_f)$

(E.23)

The areas which are spanned by the inequalities above are shown in Fig. E.1. One can see that the two areas together form a rectangle in the x_i-y_i-plane, which means that the Θ-functions decouple completely. Thus, we can write

$$\begin{aligned} \text{(E.18)} =& \Theta(x_f)\Theta(x_f - y_f)\Theta(vt - x_f) \\ & \times \Theta(-x_i)\Theta(xi - (x_f - vt)) \\ & \times \Theta(y_i - (y_f - vt))\Theta((x_f - vt) - y_i), \end{aligned} \tag{E.24}$$

which enables us to compute the propagation of the initial wavefunction.

PUBLICATIONS

1. M. P. Schneider, S. Carr, I. V. Gornyi and A. D. Mirlin, "Weak localization and magnetoresistance in a two-leg ladder model", Phys. Rev. B, **86,** 155141

2. M. P. Schneider, T. Sproll, C. Stawiarski, P. Schmitteckert and K. Busch, "Green's Function Formalism for Waveguide QED Applications", arXiv:1509.08633 and submitted to Phys. Rev. A

3. M. P. Schneider, T. Sproll, C. Martens and K. Busch, "Tunability of a one-dimensional waveguide with an embedded two-level system subjected to few photon wavepackets", in preparation

4. M. P. Schneider and K. Busch, "Waveguide QED with a nonlinear dispersion relation", in preparation

5. M. P. Schneider, C. Martens, T. Sproll and K. Busch, "Decay properties of an atom coupled to a disordered waveguide", in preparation

6. T. Sproll, C. Martens, M. P. Schneider, F. Intravaia and K. Busch, "Atomic population transfer in integrated 1-D photonic structues", in preparation

BIBLIOGRAPHY

1. J. Mehra and H. Rechenberg, *The Historical Development of Quantum Theory* (Springer New York, 2000).
2. A. Einstein, B. Podolsky and N. Rosen, "Can Quantum-Mechanical Description of Physical Reality Be Considered Complete?", Phys. Rev. **47,** 777 (1935).
3. A. Einstein, M. Born and H. Born, *The Born-Einstein letters: correspondence between Albert Einstein and Max and Hedwig Born from 1916-1955, with commentaries by Max Born* (Macmillan, 1971).
4. J. S. Bell, "On the einstein-podolsky-rosen paradox", Physics **1,** 195 (1964).
5. A. Aspect, P. Grangier and G. Roger, "Experimental Realization of Einstein-Podolsky-Rosen-Bohm *Gedankenexperiment* : A New Violation of Bell's Inequalities", Phys. Rev. Lett. **49,** 91 (1982).
6. M. Nielsen and I. Chuang, *Quantum Computation and Quantum Information* (Cambridge University Press, 2000).
7. N. Gisin and R. Thew, "Quantum communication", Nat Photon **1,** 165 (2007).
8. C. H. Bennett *et al.,* "Teleporting an unknown quantum state via dual classical and Einstein-Podolsky-Rosen channels", Phys. Rev. Lett. **70,** 1895 (1993).
9. J. L. O'Brien, A. Furusawa and J. Vuckovic, "Photonic quantum technologies", Nat Photon **3,** 687 (2009).
10. V. Giovannetti, S. Lloyd and L. Maccone, "Quantum-Enhanced Measurements: Beating the Standard Quantum Limit", Science **306,** 1330 (2004).
11. H. J. Kimble, "The quantum internet", Nature **453,** 1023 (2008).
12. J. Preskill, "Plug-in quantum software", Nature **402,** 357 (1999).
13. A. Ekert and R. Jozsa, "Quantum computation and Shor's factoring algorithm", Rev. Mod. Phys. **68,** 733 (1996).
14. A. Abrikosov, L. Gor'kov and I. Dzyaloshinski, *Methods of Quantum Field Theory in Statistical Physics* (Dover Publications, 1975).
15. M. E. Peskin and D. V. Schroeder, *An Introduction to Quantum Field Theory* (Perseus Books, Cambridge, Massachusetts, 1995).
16. G. Mahan, *Many-Particle Physics* (Springer, 2000).
17. H. Bruus and K. Flensberg, *Many-Body Quantum Theory in Condensed Matter Physics: An Introduction* (OUP Oxford, 2004).

18. M. Gell-Mann and F. Low, "Bound States in Quantum Field Theory", Phys. Rev. **84,** 350 (1951).

19. G. C. Wick, "The Evaluation of the Collision Matrix", Phys. Rev. **80,** 268 (1950).

20. R. P. Feynman, "Space-Time Approach to Quantum Electrodynamics", Phys. Rev. **76,** 769 (1949).

21. W. P. Schleich, *Quantum Optics in Phase Space* (Wiley-VCH, Berlin, 2001).

22. R. J. Glauber and M. Lewenstein, "Quantum optics of dielectric media", Phys. Rev. A **43,** 467 (1991).

23. W. Greiner and J. Reinhardt, *Field Quantization* (Springer, 1996).

24. M. Bordag, G. Klimchitskaya, U. Mohideen and V. Mostepanenko, *Advances in the Casimir Effect* (OUP Oxford, 2009).

25. E. Jaynes and F. W. Cummings, "Comparison of quantum and semiclassical radiation theories with application to the beam maser", Proceedings of the IEEE **51,** 89 (1963).

26. L. Liebermeister *et al.,* "Tapered fiber coupling of single photons emitted by a deterministically positioned single nitrogen vacancy center", Applied Physics Letters **104,** – (2014).

27. E. Vetsch *et al.,* "Optical Interface Created by Laser-Cooled Atoms Trapped in the Evanescent Field Surrounding an Optical Nanofiber", Phys. Rev. Lett. **104,** 203603 (2010).

28. O. Astafiev *et al.,* "Resonance Fluorescence of a Single Artificial Atom", Science **327,** 840 (2010).

29. J. Q. You and F. Nori, "Atomic physics and quantum optics using superconducting circuits", Nature **474,** 589 (2011).

30. A. A. Houck, H. E. Türeci and J. Koch, "On-chip quantum simulation with superconducting circuits", Nat Phys **8,** 292 (2012).

31. G. de Lange *et al.,* "Realization of Microwave Quantum Circuits Using Hybrid Superconducting-Semiconducting Nanowire Josephson Elements", Phys. Rev. Lett. **115,** 127002 (2015).

32. T. W. Larsen *et al.,* "Semiconductor-Nanowire-Based Superconducting Qubit", Phys. Rev. Lett. **115,** 127001 (2015).

33. C. Santori, D. Fattal and Y. Yamamoto, *Single-photon Devices and Applications* (Wiley-VCH, 2010).

34. P. Lodahl, S. Mahmoodian and S. Stobbe, "Interfacing single photons and single quantum dots with photonic nanostructures", Rev. Mod. Phys. **87,** 347 (2015).

35. C. Santori, D. Fattal, J. Vuckovic, G. S. Solomon and Y. Yamamoto, "Indistinguishable photons from a single-photon device", Nature **419,** 594 (2002).

36. J. Claudon *et al.,* "A highly efficient single-photon source based on a quantum dot in a photonic nanowire", Nat Photon **4,** 174 (2010).

37. M. Arcari *et al.,* "Near-Unity Coupling Efficiency of a Quantum Emitter to a Photonic Crystal Waveguide", Phys. Rev. Lett. **113,** 093603 (2014).

38. A. V. Akimov *et al.,* "Generation of single optical plasmons in metallic nanowires coupled to quantum dots", Nature **450,** 402 (2007).

39. O. Benson, "Assembly of hybrid photonic architectures from nanophotonic constituents", Nature **480,** 193 (2011).

40. A. W. Schell *et al.,* "Three-dimensional quantum photonic elements based on single nitrogen vacancy-centres in laser-written microstructures", Sci. Rep. **3** (2013).

41. A. Goban *et al.,* "Atom-light interactions in photonic crystals", Nat Commun **5,** – (2014).

42. S. Faez, P. Türschmann, H. R. Haakh, S. Götzinger and V. Sandoghdar, "Coherent Interaction of Light and Single Molecules in a Dielectric Nanoguide", Phys. Rev. Lett. **113,** 213601 (2014).

43. M. Notomi *et al.,* "Extremely Large Group-Velocity Dispersion of Line-Defect Waveguides in Photonic Crystal Slabs", Phys. Rev. Lett. **87,** 253902 (2001).

44. K. Busch *et al.,* "The photonic Wannier function approach to photonic crystal simulations: status and perspectives", Journal of Modern Optics **58,** 365 (2011).

45. A. Yariv, Y. Xu, R. K. Lee and A. Scherer, "Coupled-resonator optical waveguide: a proposal and analysis", Opt. Lett. **24,** 711 (1999).

46. J. E. Heebner, R. W. Boyd and Q.-H. Park, "SCISSOR solitons and other novel propagation effects in microresonator-modified waveguides", J. Opt. Soc. Am. B **19,** 722 (2002).

47. B.-S. Song, S. Noda, T. Asano and Y. Akahane, "Ultra-high-Q photonic double-heterostructure nanocavity", Nat Mater **4,** 207 (2005).

48. A. Wallraff *et al.,* "Strong coupling of a single photon to a superconducting qubit using circuit quantum electrodynamics", Nature **431,** 162 (2004).

49. J. T. Shen and S. Fan, "Coherent photon transport from spontaneous emission in one-dimensional waveguides", Opt. Lett. **30,** 2001 (2005).

50. J.-T. Shen and S. Fan, "Coherent Single Photon Transport in a One-Dimensional Waveguide Coupled with Superconducting Quantum Bits", Phys. Rev. Lett. **95,** 213001 (2005).

51. J.-T. Shen and S. Fan, "Strongly Correlated Two-Photon Transport in a One-Dimensional Waveguide Coupled to a Two-Level System", Phys. Rev. Lett. **98,** 153003 (2007).

52. J.-T. Shen and S. Fan, "Strongly correlated multiparticle transport in one dimension through a quantum impurity", Phys. Rev. A **76,** 062709 (2007).

53. S. Fan, Ş. E. Kocabaş and J.-T. Shen, "Input-output formalism for few-photon transport in one-dimensional nanophotonic waveguides coupled to a qubit", Phys. Rev. A **82,** 063821 (2010).

54. B. Q. Baragiola, R. L. Cook, A. M. Brańczyk and J. Combes, "N-photon wave packets interacting with an arbitrary quantum system", Phys. Rev. A **86,** 013811 (2012).

55. T. Shi and C. P. Sun, "Lehmann-Symanzik-Zimmermann reduction approach to multi-photon scattering in coupled-resonator arrays", Phys. Rev. B **79,** 205111 (2009).

56. M. Pletyukhov and V. Gritsev, "Scattering of massless particles in one-dimensional chiral channel", New Journal of Physics **14,** 095028 (2012).

57. M. Pletyukhov and V. Gritsev, "Quantum theory of light scattering in a one-dimensional channel: Interaction effect on photon statistics and entanglement entropy", Phys. Rev. A **91,** 063841 (2015).

58. H. Zheng, D. J. Gauthier and H. U. Baranger, "Waveguide QED: Many-body bound-state effects in coherent and Fock-state scattering from a two-level system", Phys. Rev. A **82,** 063816 (2010).

59. H. Zheng, D. J. Gauthier and H. U. Baranger, "Cavity-Free Photon Blockade Induced by Many-Body Bound States", Phys. Rev. Lett. **107,** 223601 (2011).

60. H. Zheng, D. J. Gauthier and H. U. Baranger, "Strongly correlated photons generated by coupling a three- or four-level system to a waveguide", Phys. Rev. A **85,** 043832 (2012).

61. T. Shi, S. Fan and C. P. Sun, "Two-photon transport in a waveguide coupled to a cavity in a two-level system", Phys. Rev. A **84,** 063803 (2011).

62. T. Shi and S. Fan, "Two-photon transport through a waveguide coupling to a whispering-gallery resonator containing an atom and photon-blockade effect", Phys. Rev. A **87,** 063818 (2013).

63. M. Laakso and M. Pletyukhov, "Scattering of Two Photons from Two Distant Qubits: Exact Solution", Phys. Rev. Lett. **113,** 183601 (2014).

64. E. Rephaeli and S. Fan, "Dissipation in few-photon waveguide transport", Photon. Res. **1,** 110 (2013).

65. F. Ciccarello, "Waveguide-QED-based measurement of a reservoir spectral density", Phys. Rev. A **91,** 062121 (2015).

66. S. Xu, E. Rephaeli and S. Fan, "Analytic Properties of Two-Photon Scattering Matrix in Integrated Quantum Systems Determined by the Cluster Decomposition Principle", Phys. Rev. Lett. **111,** 223602 (2013).

67. E. Rephaeli and S. Fan, "Stimulated Emission from a Single Excited Atom in a Waveguide", Phys. Rev. Lett. **108,** 143602 (2012).

68. E. Rephaeli, J.-T. Shen and S. Fan, "Full inversion of a two-level atom with a single-photon pulse in one-dimensional geometries", Phys. Rev. A **82,** 033804 (2010).

69. Y. Chen, M. Wubs, J. Mørk and A. Koenderink, "Coherent single-photon absorption by single emitters coupled to one-dimensional nanophotonic waveguides", New Journal of Physics **13,** 103010 (2011).

70. A. Nysteen, P. T. Kristensen, D. P. S. McCutcheon, P. Kaer and J. Mørk, "Scattering of two photons on a quantum emitter in a one-dimensional waveguide: exact dynamics and induced correlations", New Journal of Physics **17,** 023030 (2015).

71. A. Nysteen, D. P. S. McCutcheon and J. Mørk, "Strong nonlinearity-induced correlations for counterpropagating photons scattering on a two-level emitter", Phys. Rev. A **91,** 063823 (2015).

72. S. John and J. Wang, "Quantum electrodynamics near a photonic band gap: Photon bound states and dressed atoms", Phys. Rev. Lett. **64,** 2418 (1990).

73. S. John and T. Quang, "Spontaneous emission near the edge of a photonic band gap", Phys. Rev. A **50,** 1764 (1994).

74. L. Zhou, Z. R. Gong, Y.-x. Liu, C. P. Sun and F. Nori, "Controllable Scattering of a Single Photon inside a One-Dimensional Resonator Waveguide", Phys. Rev. Lett. **101,** 100501 (2008).

75. P. Longo, P. Schmitteckert and K. Busch, "Dynamics of photon transport through quantum impurities in dispersion-engineered one-dimensional systems", Journal of Optics A: Pure and Applied Optics **11,** 114009 (2009).

76. P. Longo, P. Schmitteckert and K. Busch, "Few-Photon Transport in Low-Dimensional Systems: Interaction-Induced Radiation Trapping", Phys. Rev. Lett. **104,** 023602 (2010).

77. P. Longo, P. Schmitteckert and K. Busch, "Few-photon transport in low-dimensional systems", Phys. Rev. A **83,** 063828 (2011).

78. P. Longo, J. H. Cole and K. Busch, "The Hong-Ou-Mandel effect in the context of few-photon scattering", Opt. Express **20,** 12326 (2012).

79. M. Moeferdt, P. Schmitteckert and K. Busch, "Correlated photons in one-dimensional waveguides", Opt. Lett. **38,** 3693 (2013).

80. J. F. M. Werra, P. Longo and K. Busch, "Spectra of coherent resonant light pulses interacting with a two-level atom in a waveguide", Phys. Rev. A **87,** 063821 (2013).

81. C. Martens, P. Longo and K. Busch, "Photon transport in one-dimensional systems coupled to three-level quantum impurities", New Journal of Physics **15,** 083019 (2013).

82. E. Sanchez-Burillo, D. Zueco, J. J. Garcia-Ripoll and L. Martin-Moreno, "Scattering in the Ultrastrong Regime: Nonlinear Optics with One Photon", Phys. Rev. Lett. **113,** 263604 (2014).

83. C. Stawiarski, Diplomarbeit (Karlsruhe Institute of Technology, 2010).

84. M. P. Schneider, T. Sproll, C. Stawiarski, P. Schmitteckert and K. Busch, "Green's Function Formalism for Waveguide QED Applications", arXiv:1509.08633 (2015).

85. H. Lehmann, K. Symanzik and W. Zimmermann, "Zur Formulierung quantisierter Feldtheorien", German. Il Nuovo Cimento **1,** 205 (1955).

86. G. Zaránd, L. Borda, J. von Delft and N. Andrei, "Theory of Inelastic Scattering from Magnetic Impurities", Phys. Rev. Lett. **93,** 107204 (2004).

87. L. Borda, L. Fritz, N. Andrei and G. Zaránd, "Theory of inelastic scattering from quantum impurities", Phys. Rev. B **75,** 235112 (2007).

88. A. Braun and P. Schmitteckert, "Numerical evaluation of Green's functions based on the Chebyshev expansion", Phys. Rev. B **90,** 165112 (2014).

89. I.-C. Hoi *et al.,* "Generation of Nonclassical Microwave States Using an Artificial Atom in 1D Open Space", Phys. Rev. Lett. **108,** 263601 (2012).

90. T. Sproll, C. Martens, M. P. Schneider, F. Intravaia and K. Busch, *Förster energy Transfer in the context of integrated 1D structures* (unpublished).

91. J. J. Sakurai, *Modern Quantum Mechanics (Revised Edition)* (Addison Wesley, 1993).

92. C. Kurtsiefer, S. Mayer, P. Zarda and H. Weinfurter, "Stable Solid-State Source of Single Photons", Phys. Rev. Lett. **85,** 290 (2000).

93. C. Santori, M. Pelton, G. Solomon, Y. Dale and Y. Yamamoto, "Triggered Single Photons from a Quantum Dot", Phys. Rev. Lett. **86,** 1502 (2001).

94. A. A. Houck *et al.,* "Generating single microwave photons in a circuit", Nature **449,** 328 (2007).

95. C. Reimer *et al.,* "Integrated frequency comb source of heralded single photons", Opt. Express **22,** 6535 (2014).

96. G. K. Gulati *et al.,* "Generation of an exponentially rising single-photon field from parametric conversion in atoms", Phys. Rev. A **90,** 033819 (2014).

97. M. T. Rakher *et al.,* "Simultaneous Wavelength Translation and Amplitude Modulation of Single Photons from a Quantum Dot", Phys. Rev. Lett. **107,** 083602 (2011).

98. P. B. R. Nisbet-Jones, J. Dilley, D. Ljunggren and A. Kuhn, "Highly efficient source for indistinguishable single photons of controlled shape", New Journal of Physics **13,** 103036 (2011).

99. P. Nisbet-Jones, PhD thesis (St. John's College, 2012).

100. B. Srivathsan, G. K. Gulati, A. Cerè, B. Chng and C. Kurtsiefer, "Reversing the Temporal Envelope of a Heralded Single Photon using a Cavity", Phys. Rev. Lett. **113,** 163601 (2014).

101. R. Glauber, *Quantum Theory of Optical Coherence: Selected Papers and Lectures* (Wiley, 2007).

102. C. Martens, PhD thesis (Humboldt Universität zu Berlin, (unpublished)).

103. P. W. Anderson, "Localized Magnetic States in Metals", Phys. Rev. **124,** 41 (1961).

104. S. John, "Localization of Light", Physics Today **44,** 32 (1991).

105. J. Topolancik, B. Ilic and F. Vollmer, "Experimental Observation of Strong Photon Localization in Disordered Photonic Crystal Waveguides", Phys. Rev. Lett. **99,** 253901 (2007).

106. L. Sapienza *et al.,* "Cavity Quantum Electrodynamics with Anderson-Localized Modes", Science **327,** 1352 (2010).

107. J. Gao *et al.,* "Strongly coupled slow-light polaritons in one-dimensional disordered localized states", Sci. Rep. **3,** 1994 (2013).

108. A. Greshnov, M. Kaliteevski, R. Abram, S. Brand and G. Zegrya, "Density of states in 1D disordered photonic crystals: Analytical solution", Solid State Communications **146,** 157 (2008).

109. S. F. Liew and H. Cao, "Optical properties of 1D photonic crystals with correlated and uncorrelated disorder", Journal of Optics **12,** 024011 (2010).

110. M. Patterson and S. Hughes, "Interplay between disorder-induced scattering and local field effects in photonic crystal waveguides", Phys. Rev. B **81,** 245321 (2010).

111. N. Mann, A. Javadi, P. D. García, P. Lodahl and S. Hughes, "Theory and experiments of disorder-induced resonance shifts and mode-edge broadening in deliberately disordered photonic crystal waveguides", Phys. Rev. A **92,** 023849 (2015).

112. M. Köhl, C. Wolff and K. Busch, "Cluster coherent potential approximation for disordered photonic crystals using photonic Wannier functions", Opt. Lett. **37,** 560 (2012).

113. M. Köhl, C. Wolff and K. Busch, "Disordered photonic crystals: a cluster coherent potential approach using photonic Wannier functions", J. Opt. Soc. Am. B **31,** 2246 (2014).

114. B. L. Altshuler, D. Khmel'nitzkii, A. I. Larkin and P. A. Lee, "Magnetoresistance and Hall effect in a disordered two-dimensional electron gas", Phys. Rev. B **22,** 5142 (1980).

115. B. L. Al'tshuler, "Fluctuations in the extrinsic conductivity of disordered conductors", JETP Letters **41,** 648 (1985).

116. P. A. Lee and A. D. Stone, "Universal Conductance Fluctuations in Metals", Phys. Rev. Lett. **55,** 1622 (1985).

117. A. Altland and B. Simons, *Condensed Matter Field Theory* (Cambridge University Press, 2010).

118. J. Rammer, *Quantum Transport Theory* (Westview Press, 2004).

119. A. F. Ioffe and A. R. Regel, "Non-crystalline, Amorphous, and Liquid Electronic Semiconductors", Prog. Semicond. **4,** 237 (1960).

120. E. Abrahams, P. W. Anderson, D. C. Licciardello and T. V. Ramakrishnan, "Scaling Theory of Localization: Absence of Quantum Diffusion in Two Dimensions", Phys. Rev. Lett. **42,** 673 (1979).

121. I. M. Lifshitz, "The Energy Spectrum of Disordered Systems", Adv. Phys. **13,** 483 (1964).

122. S. John, "Electromagnetic Absorption in a Disordered Medium near a Photon Mobility Edge", Phys. Rev. Lett. **53,** 2169 (1984).

123. S. John and R. Rangarajan, "Optimal structures for classical wave localization: an alternative to the ioffe-regel criterion", Phys. Rev. B **38,** 10101 (1988).

124. C. Wolff, P. Mack and K. Busch, "Generation of Wannier functions for photonic crystals", Phys. Rev. B **88,** 075201 (2013).

125. R. Mitsch, C. Sayrin, B. Albrecht, P. Schneeweiss and A. Rauschenbeutel, "Directional nanophotonic atom–waveguide interface based on spin–orbit interaction of light", arXiv:1406.0896 (2014).

126. T. Sproll, PhD thesis (Humboldt Universität zu Berlin, (unpublished)).